

---

# Matrix-product states for strongly correlated systems and quantum information processing

Hamed Saberi

---



München 2008



---

# **Matrix-product states for strongly correlated systems and quantum information processing**

**Hamed Saberi**

---

Dissertation  
an der Fakultät für Physik  
der Ludwig–Maximilians–Universität  
München

vorgelegt von  
Hamed Saberi  
aus Arak

München, den 12. Dezember 2008

Erstgutachter: Prof. Dr. Jan von Delft

Zweitgutachter: Prof. Dr. Matthias Christandl

Tag der mündlichen Prüfung: 23. Januar 2009

To my parents



# Contents

<b>Abstract</b>	<b>xv</b>
<b>I General Introduction and Basic Concepts</b>	<b>1</b>
<b>1 Introduction and motivation</b>	<b>3</b>
<b>2 DMRG and matrix-product states</b>	<b>7</b>
2.1 Transition from NRG to DMRG . . . . .	8
2.2 Matrix-product states in the context of strongly correlated systems . . . .	12
2.3 DMRG leads to MPS . . . . .	13
<b>3 MPS in the context of quantum information processing</b>	<b>15</b>
3.1 Definition and graphical representation of MPS . . . . .	15
3.2 Schmidt decomposition and singular value decomposition . . . . .	17
3.3 Vidal decomposition . . . . .	18
3.4 Prototypical low-dimensional MPS in quantum information theory . . . . .	21
3.5 MPS for sequential generation of entangled multiqubit states . . . . .	23
<b>II Results</b>	<b>27</b>
<b>4 MPS comparison of NRG and the variational formulation of DMRG</b>	<b>29</b>
4.1 Introduction . . . . .	29
4.2 Folded and unfolded representations of Wilson chain . . . . .	32
4.3 NRG treatment of folded Wilson chain . . . . .	34
4.3.1 NRG matrix-product state arises by iteration . . . . .	34
4.3.2 NRG truncation . . . . .	35
4.3.3 Mutual information of opposite spins on site $n$ . . . . .	36
4.4 DMRG treatment of unfolded Wilson chain . . . . .	40

4.4.1	Variational matrix-product state ansatz . . . . .	40
4.4.2	VMPS truncation . . . . .	41
4.4.3	Refolding . . . . .	43
4.5	Comparison of NRG and VMPS results . . . . .	44
4.5.1	Ground state energies and overlaps . . . . .	45
4.5.2	Comparison of eigenspectra and density of states . . . . .	46
4.5.3	Comparison of energy eigenstates . . . . .	50
4.6	Cloning and variational improvement of NRG ground state . . . . .	54
4.6.1	Mapping folded to unfolded states by cloning . . . . .	56
4.6.2	Variational energy minimization of $ G\rangle_c$ . . . . .	57
4.7	Conclusions . . . . .	59
<b>5</b>	<b>Constrained optimization of sequentially generated multiqubit states</b>	<b>63</b>
5.1	Introduction . . . . .	64
5.2	Restrictions on the number of ancilla levels . . . . .	64
5.2.1	SVD for matrix approximation . . . . .	65
5.2.2	SVD for MPS compression . . . . .	68
5.2.3	Variational optimization for ancilla dimension . . . . .	69
5.3	Restrictions on the source-qubit interactions . . . . .	70
5.4	Conclusions . . . . .	74
<b>6</b>	<b>Approximate sequential implementation of global operations</b>	<b>77</b>
6.1	Introduction . . . . .	77
6.2	Sequential decomposition of global unitaries within Frobenius metric . . . . .	78
6.2.1	Results for ancilla of dimension $D = 2$ . . . . .	80
6.2.2	Results for ancilla of dimension $D = 4$ . . . . .	81
6.3	Sequential decomposition of global isometries within Frobenius norm metric . . . . .	82
6.3.1	The map $1 \rightarrow N$ . . . . .	83
6.3.2	The map $M \rightarrow N$ when $1 < M < N$ . . . . .	84
6.4	Sequential decomposition of global unitaries within $p$ -norm metric . . . . .	84
6.5	Conclusions . . . . .	87
<b>III</b>	<b>Appendix</b>	<b>89</b>
<b>A</b>	<b>Orthonormalization of <math>B</math>-matrices of unfolded Wilson chain</b>	<b>91</b>
<b>B</b>	<b>Refolding</b>	<b>93</b>



---

C	Calculation of the effective Hamiltonian within the MPS formalism	95
D	Variational “cloning” of folded to unfolded states	103
E	Matrix norm and singular value decomposition	107
IV	Miscellaneous	109
	Bibliography	111
	Deutsche Zusammenfassung	119
	Acknowledgements	121
	Curriculum Vitae	125



# List of Figures

1.1	MPS “net” . . . . .	4
2.1	Sketch of real-space NRG for Hubbard model . . . . .	9
2.2	Sketch of the superblock method . . . . .	11
2.3	DMRG leads to MPS . . . . .	13
3.1	Graphical representation of an OBC-MPS . . . . .	16
3.2	Sketch of the relation between Vidal MPS and standard MPS . . . . .	19
3.3	Sketch of the sequential quantum factory of states . . . . .	24
4.1	Folded and unfolded representation of the Wilson chain . . . . .	34
4.2	MPS representation of folded and unfolded Wilson chain . . . . .	37
4.3	NRG result for mutual information between spin-down and -up . . . . .	39
4.4	Singular values spectrum of the unfolded Wilson chain . . . . .	42
4.5	NRG and VMPS results for the ground state energies and overlaps . . . . .	47
4.6	Graphical representation of the MPS contraction patterns . . . . .	48
4.7	NRG and VMPS flow diagrams . . . . .	49
4.8	NRG and VMPS density of states . . . . .	50
4.9	Plot of the overlap matrix between NRG and refolded VMPS . . . . .	52
4.10	Plot of the weights of NRG eigenstates within VMPS-subspace . . . . .	53
4.11	Plot of the integrated NRG weights within VMPS-subspace . . . . .	55
4.12	Results for the cloning procedure . . . . .	57
4.13	Sweeping on NRG-initialized state . . . . .	58
5.1	Matrix approximation with the aid of SVD . . . . .	68
5.2	Optimizing the ancilla dimension . . . . .	70
5.3	Graphical representation of constrained MPS optimization . . . . .	71
5.4	Generation of $W$ state with restricted interactions . . . . .	73
6.1	MPO representation of global and sequential unitaries . . . . .	79

---

6.2	Quantum logic gate representation of two paradigmatic global gates . . . .	82
6.3	Scaling of the Frobenius fidelity with number of qubits . . . . .	83
6.4	Graphical representation of a sequentially generated global isometry . . . .	84
C.1	Couplings structure of the unfolded and refolded Wilson chain . . . . .	96
C.2	Subchain Hamiltonian splitted into three parts . . . . .	97
C.3	Effective refolded Hamiltonian for the site $k = 1$ . . . . .	98
C.4	Effective refolded Hamiltonian for the site $k = 2$ . . . . .	100
C.5	General recipe for obtaining the effective refolded Hamiltonian . . . . .	101
D.1	Graphical representation of the “cloning” procedure . . . . .	104

# List of Tables

5.1	Comparing our simulation to experimental realization of $W$ state . . . . .	74
6.1	Frobenius fidelity of sequential implementation of various global gates . . .	81
6.2	$p$ -norm fidelity for sequential implementation of various global gates . . . .	85
6.3	Frobenius fidelity with the same normalization scheme as the 2-norm metric	86



# Abstract

This thesis offers new developments in matrix-product state theory for studying the strongly correlated systems and quantum information processing through three major projects:

In the first project, we perform a systematic comparison between Wilson’s numerical renormalization group (NRG) and White’s density-matrix renormalization group (DMRG). The NRG method for solving quantum impurity models yields a set of energy eigenstates that have the form of matrix-product states (MPS). White’s DMRG for treating quantum lattice problems can likewise be reformulated in terms of MPS. Thus, the latter constitute a common algebraic structure for both approaches. We exploit this fact to compare the NRG approach for the single-impurity Anderson model to a variational matrix-product state approach (VMPS), equivalent to single-site DMRG. For the latter, we use an “unfolded” Wilson chain, which brings about a significant reduction in numerical costs compared to those of NRG. We show that all NRG eigenstates (kept and discarded) can be reproduced using VMPS, and compare the difference in truncation criteria, sharp vs. smooth in energy space, of the two approaches. Finally, we demonstrate that NRG results can be improved upon systematically by performing a variational optimization in the space of variational matrix-product states, using the states produced by NRG as input.

In the second project we demonstrate how the matrix-product state formalism provides a flexible structure to solve the *constrained* optimization problem associated with the sequential generation of entangled multiqubit states under experimental restrictions. We consider a realistic scenario in which an ancillary system with a limited number of levels performs restricted sequential interactions with qubits in a row. The proposed method relies on a suitable local optimization procedure, yielding an efficient recipe for the realistic and approximate sequential generation of any entangled multiqubit state. We give paradigmatic examples that may be of interest for theoretical and experimental developments.

The third project deals with sequential generation of *operations*. It is known that engineering an arbitrary global unitary is generically hard. From this point of view, it would be desirable to devise a protocol to implement the desired global unitary operation in a sequential procedure in which an itinerant ancillary system interacts locally and only once with each qubit in a row. Here the main question will be whether it is possible to design such a sequentially generated operation which has the same effect of the desired global unitary or not? We provide optimization protocols that allow an optimal realization of a sequential version of the target global unitary with an optimal fidelity.





# Part I

## General Introduction and Basic Concepts



# Chapter 1

## Introduction and motivation

One of the most important limitations of numerical calculations on strongly correlated systems is the great amount of states that have to be considered and the exponential growth of the dimension of the Hilbert space with system size. A number of techniques have been introduced in order to reduce the size of the Hilbert space to a manageable size to be able to reach larger systems, such as quantum monte carlo [1], numerical renormalization group (NRG) [2, 3, 4] and density-matrix renormalization group (DMRG) [5, 6, 7, 8, 9, 10]. Each method entails a particular criterion of keeping the most relevant information. One of the most powerful techniques for studying strongly correlated electron systems is the density-matrix renormalization group, which was developed by Steven White in 1992 [5]. Its field of applicability has now extended beyond condensed matter physics and is successfully used in statistical mechanics, high energy physics and *ab initio* quantum chemistry [11, 12].

Moreover, models for qubits coupled to a dissipative environment are quantum impurity models [13, 14, 15], in which a local degree of freedom, the “impurity”, is coupled to a continuous bath of excitations. For many years, the only reliable numerical approach to the latter has been the numerical renormalization group (NRG). In this work, we show that such models can also be addressed using the more powerful and flexible density-matrix renormalization group [16], and compare its results to those of NRG. In particular, this opens up perspectives for studying time-dependent driven qubits in the future [17, 18, 19].

The fact that an impurity model can be treated by two related but nonequivalent methods immediately raises an interesting and fundamental methodological question: How do the two methods compare? More precisely, to what extent and under which circumstances do their results agree or disagree? How do the differences in their criteria for keeping the relevant information manifest themselves? In the first part of this thesis we address this type of questions.

A few years after the advent of DMRG, it was understood that [20, 21, 22] the approximate ground states produced by DMRG have the form of matrix-product states (MPS) which can be explored and optimized variationally with an efficient use of computational resources.

Fortunately, states arising for instance as ground states from *local* physical interactions

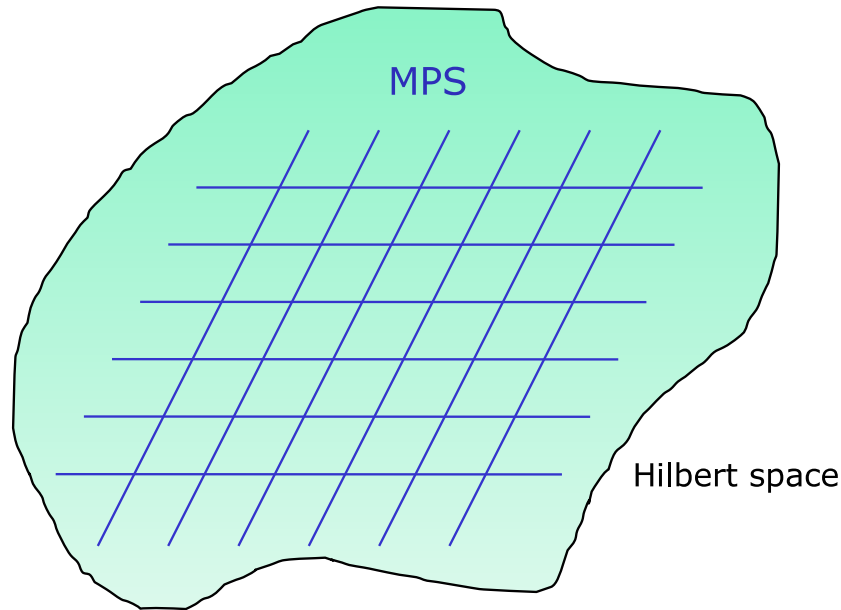


**Figure 1.1:** MPS as an effective “net” on the huge Hilbert space of many-body systems to capture the most relevant information.

are not uniformly distributed in Hilbert space. Hence, it is desirable to find a representation of quantum many-body states that efficiently describes the resulting *local* correlations. The *matrix-product-state* (MPS) representation turns out to be the one capable of realizing this idea: In fact, this representation accounts for the power of the density-matrix renormalization group method and provides a flexible common basis for a tremendous amount of recent developments in quantum information and condensed matter theory [23].

Roughly speaking, MPS can be regarded as an effective “net” on the huge Hilbert space of many-body Hamiltonian to capture the essential physics contained in the most relevant regions of the Hilbert space (see Fig. 1.1). MPS provides a flexible algebraic structure to store and manipulate the relevant information. Due to its matrix-product structure, it makes it possible to exploit the mathematical tools already developed in linear algebra, most importantly the *singular value decomposition* (SVD), recognized as a “singularly valuable decomposition!”, for obtaining an efficient full-rank representation of the underlying matrices. Moreover, it allows for defining *distance measures* in the Hilbert space through the known  $p$ -norm or Frobenius norm of the matrices expressible in terms of the singular value decomposition (see Appendix E).

In this thesis we shall exploit the common matrix-product structure for performing an exhaustive comparison between NRG and DMRG approaches when applied to a single-impurity Anderson model [24]. We show that the MPS-based variational formulation of DMRG is able to fully reproduce *all* information obtainable from NRG. We also explore the question how the two approaches compare in numerical demands for the sake of obtaining the ground state and excited state properties.

Matrix-product states play an important role also in the context of quantum information processing [25, 26, 27, 23]. Paradigmatic multiqubit states, such as Greenberger-Horne-Zeilinger (GHZ) [28],  $W$  [29] and cluster [30] states, can be described by low-dimensional MPS and are considered valuable resources for quantum information and communication tasks. The generation of multiqubit entangled states via a single *global* unitary operation acting on initially decoupled qubits is in general a difficult problem. From this point of view, several theoretical and experimental efforts have been oriented towards the *sequential* generation of paradigmatic entangled multipartite states. It turns out that the classes of all sequentially generated multiqubit states, assisted by an itinerant ancilla, are exactly given by the hierarchy of matrix-product states [26, 31, 32].

However, the sequential recipe for the generation on demand of any arbitrary multiqubit state requires a full control over the experimental resources which does not quite correspond to what is the case in practice [31], where only a restricted class of interactions are available and some atomic or qubit degrees of freedom can not be manipulated easily. In this sense, two important theoretical and experimental questions appear naturally: will the sequential generation of a desired multiqubit state still be feasible under given restricted experimental conditions? And if the answer is no, can we design an efficient protocol that tells us the best possible approximation to the sequential generation of such state? In this thesis we address satisfactorily both questions [33]. We demonstrate how linear algebraic tools accessible to MPS formalism can be exploited to study this relevant *constrained* optimization problem [34].

It is noteworthy to mention that engineering a global multiqubit operation acting simultaneously on several qubits is known to be a task of formidable difficulty. It will be then desirable to devise a recipe in which the target multiqubit operation can be implemented in a *sequence* of two-qubit operations. In this work we show how the matrix-product operator (MPO) formalism [35, 36, 37, 38] (a generalized version of MPS formalism from *states* to *operations*) offers a flexible framework to study this problem. In general, the task of sequential generation of non-trivially entangling multiqubit operation was proved in Ref. [39] to be impossible even with a full access to experimental resources. Our numerics confirm this “no-go” theorem and provides an optimal procedure with which a global unitary can be implemented in a sequential manner with the maximal fidelity.

This thesis is structured as follows: **Part I** introduces the numerical methods used throughout this thesis. A brief introduction to DMRG and the historical transition from real-space NRG to DMRG are provided in Chapter 2. Moreover, the natural connection between DMRG and MPS is elucidated here. In Chapter 3, a quantum information perspective on matrix-product states is introduced. Various paradigmatic low-dimensional MPS representation of entangled multiqubit states are presented here. The chapter ends with an overview of sequential generation of entangled multiqubit states within MPS formalism. We point out Part I introduces basic concepts in principle useful for all results of Part II, but the introductory materials of Chapter 2 (3) will be specifically needed for the results of Chapter 4 (5 and 6).

**Part II** contains our results. In Chapter 4 results of a systematic comparison between

NRG and variational formulation of DMRG are presented. An MPS reformulation of both NRG and DMRG is followed by comparison of various ground state and excited state properties of the single impurity Anderson model. In Chapter 5 we present analytical and numerical protocols for an efficient sequential generation of entangled multiqubit states under realistic experimental constraints. Motivated by a recently proved “no-go” theorem for the sequential generation of global multiqubit operations by Lamata *et al* [39], in Chapter 6 we give our numerical results for an optimal sequential generation of certain canonical multiqubit gates of quantum computation with maximal fidelity.

**Part III** collects some technical details on various manipulations involving matrix-product states.

Finally, **Part IV** contains miscellaneous items, the bibliography, the acknowledgements, the “Deutsche Zusammenfassung” and author’s curriculum vitae.

## Chapter 2

# Density-matrix renormalization group and matrix-product states

*Note that the concepts introduced in this chapter will be particularly useful for the calculations of our first project presented in Chapter 4.*

In this chapter, we provide a brief historical overview of two concepts of central importance to this thesis, namely DMRG and matrix-product states.

Shortly after Wilson's dramatic success in solving the Kondo problem [40] with a renormalization group (RG) method [2], there was considerable excitement about the possibility of applying the same type of approach to a variety of quantum lattice problems such as Hubbard and Heisenberg models, with lattice sites replacing energy levels. These real-space renormalization schemes quickly developed a bad reputation, after several applications of the method gave poor results. Actually the method had little success for anything but quantum impurity problems. In order to see what goes wrong with numerical renormalization group (NRG) when applied to real-space models, we first review in Section 2.1 the real-space NRG algorithm for a one-dimensional quantum lattice [7]. In this Section we also explain how White's DMRG eventually offered an RG scheme to overcome these problems. Section 2.2 gives a brief history of MPS and the relevance to strongly correlated systems. In Section 2.3 we explain how the renormalization procedure in a natural way leads to a state of matrix-product form.

## 2.1 Transition from NRG to DMRG

As a prototypical quantum chain model, we may mention a one-dimensional tight-binding chain [41] with hopping rates  $t_{ij}$  and on-site Coulomb interactions  $U_i$ , given by

$$\mathcal{H} = \sum_{i,j} t_{ij} a_{i\sigma}^\dagger a_{j\sigma} + \sum_i U_i n_{i\uparrow} n_{i\downarrow}, \quad (2.1)$$

where  $a_{i,\sigma}^\dagger$  ( $a_{i,\sigma}$ ) creates (annihilates) fermions of spin  $\sigma = \{\uparrow, \downarrow\}$  in an orbital centered at site  $i$ , and  $n_{i\sigma}$  denotes the occupation number operator  $n_{i\sigma} = a_{i\sigma}^\dagger a_{i\sigma}$ . In the specific case that the hopping rates and the on-site interactions are constant ( $t_{ij} = t = \text{const.}$  and  $U_i = U = \text{const.}$ ) this model reduces to the Hubbard model [42]

$$\mathcal{H} = t \sum_{i,j} a_{i\sigma}^\dagger a_{j\sigma} + U \sum_i n_{i\uparrow} n_{i\downarrow}. \quad (2.2)$$

In the standard real-space NRG, one begins by breaking the 1D chain into finite identical blocks. It is usually convenient to start at the very first iteration with blocks consisting of just one site. We will label the blocks by  $B$  and the corresponding block Hamiltonian by  $H_B$ .  $H_B$  contains all terms of the Hamiltonian  $H$  involving only sites contained in  $B$ . For example, for the Hubbard model at the first iteration, when  $B$  consists of one site,  $H_B = U n_{i\uparrow} n_{i\downarrow}$ , or for the Heisenberg model at the first iteration,  $H_B = 0$ . Rather than describing  $B$  and  $H_B$  in the usual way by listing the sites of  $B$  and using second-quantized operator expressions for  $H_B$ , we describe  $B$  by a list of the many-body states on the block, and by quantum numbers and matrix elements between these states.  $H_B$  is represented then as an  $m \times m$  matrix where  $m$  is the number of states of the block  $B$ . In order to reconstruct  $H$ , additional information about the interactions between blocks is needed besides  $H_B$ . For instance, for a Hubbard model one would have to store matrices for  $a_{i\sigma}$  in order to reconstruct the hopping term. The standard procedure, illustrated in Fig. 2.1, now goes as follows [7]:

1. At the beginning of an iteration one forms the Hamiltonian for two blocks joined together  $H_{BB}$  where  $BB$  has  $m^2$  states.
2. The lowest-lying eigenstates  $u_{i_1 i_2}^\alpha$ ,  $\alpha = 1 \dots m$  of  $H_{BB}$  are the states used to describe  $B'$  ( $BB \rightarrow B'$ ), obtaining by diagonalization of  $H_{BB}$ .
3. Then one forms matrix representations of boundary operators corresponding to the interactions between neighboring blocks for  $BB$  from the corresponding matrices for  $B$ .
4. The new block Hamiltonian matrix  $H_{B'}$  is evidently diagonal in this basis, but in the more general case where the states kept, the  $u^\alpha$ , are not eigenstates of  $H_{BB}$  we can use this transformation where the  $m \times m^2$  matrix  $O$  is made out of the basis



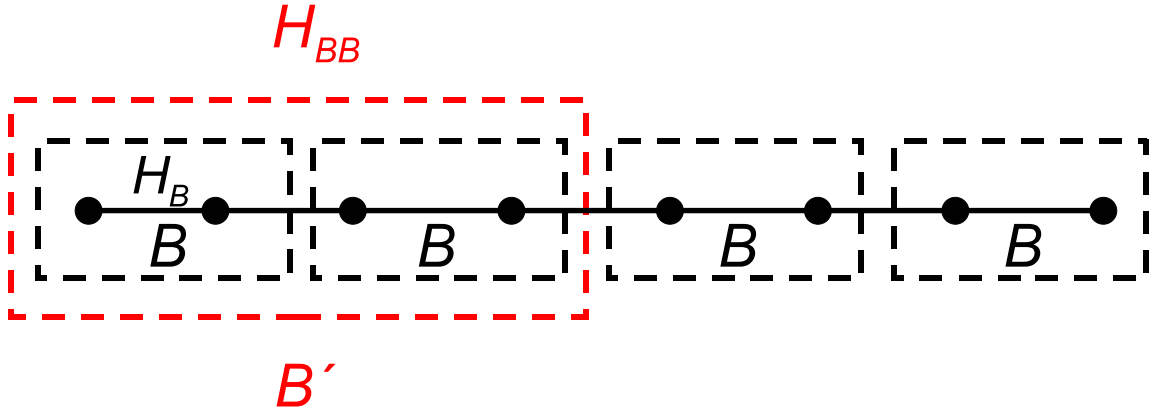


**Figure 2.1:** Sketch of real-space NRG for Hubbard model. The 1D chain is splitted into finite identical blocks labeled by  $B$  and the corresponding block Hamiltonians  $H_B$ . The RG procedure is then carried out by iterative diagonalization of the joint blocks  $H_{BB}$ .

$u^\alpha$  in such a way that the rows of  $O$  are the states kept. If  $O$  were square, this would be a unitary transformation. Since  $O$  is not square, the transformation is an *isometry* ( $O^\dagger O = \mathbb{1}$ ) that truncates away the high-energy states (see also Footnote 2 in Section 5.2 for isometries contrasted to unitaries). Moreover, in order to obtain new matrices for boundary operators at this stage, it is necessary to use the isometry  $O$  again.

5. Now we can replace  $B$  by  $B'$  and start the next iteration.

The iteration is continued until the system is large enough to represent properties of an infinite system.

Bray and Chui applied the outlined approach to the 1D Hubbard model and the results were quite discouraging [43]. The reason for this breakdown lies in the physical difference between Kondo problem and real-space quantum lattices. The most important difference between the Kondo system and a real-space 1D system is that the couplings between adjacent layers or sites decrease exponentially in the Kondo system, whereas it remains constant for a 1D quantum chain system (see for instance Eq. (2.2)). More precisely, for the Kondo model  $t_{ij} = \Lambda^{-i/2}$  in Eq. (2.1) where  $\Lambda$  is a constant discretization parameter [40, 3]. This exponential decrease is the key to the success of the method for the Kondo system and related impurity systems, but when applied to quantum lattice problems in a real-space blocking form, the approach is flawed in its treatment of the boundaries of a block. More precisely, the fundamental difficulty in the standard approach above lies in choosing the eigenstates of  $H_{BB}$  to be the states kept. Since  $H_{BB}$  contains no connections to the rest of the lattice, its eigenstates have inappropriate features at the block ends. In other words, merely considering isolated blocks imposes wrong boundary conditions on the block boundaries. The density-matrix renormalization group (DMRG) was originally developed

to overcome this sort of problems.

Xiang and Gehring applied a slight variation of the outlined real-space NRG to the 1D Heisenberg model [44]. Their method added a single site to a block at each iteration, rather than doubling the block size each time, growing the system more adiabatically, so to speak. This improvement gave somewhat more encouraging results.

White and Noack studied a toy model of the standard particle-in-a-box problem in detail suggesting two alternatives to the standard approach and they could obtain excellent results by combining Hilbert spaces from low-lying states of block  $B$  obtained by assuming various combinations of fixed and free boundary conditions [45]. In both methods the states that were kept were *not* the eigenstates of the Hamiltonian  $H_{BB}$ :

In the first method, the combination of boundary conditions (CBC approach) the lowest-lying eigenstates of several different block Hamiltonians were kept. The several-block Hamiltonian differed only in the boundary condition applied to a block, e.g. one Hamiltonian might have periodic boundary condition applied and another antiperiodic boundary condition. The rationale for this was that quantum fluctuations in the rest of system effectively apply a variety of boundary conditions to the block and states from any single boundary condition cannot respond properly to these fluctuations [7]. The CBC approach proved very successful for the simple single-particle problems. The lesson was that any approach using one set of boundary conditions on a block generates a set of states which is in some sense “incomplete”, and it is impossible to correct this incompleteness by keeping more states or by applying perturbative corrections. However, CBC approach turned out to be unsuccessful for interacting systems like a Heisenberg chain. The reason for this failure was that it is typically very difficult to obtain a set of kept states that comply with a wide range of boundary behavior associated with different particles.

The other approach proposed by White and Noack, the “superblock” method, forms the basis for DMRG. In the superblock method one diagonalizes a larger system (the superblock) composed of three or more blocks including the two blocks  $BB$  which are used to form  $B'$ . The wavefunctions for the superblock are projected onto  $BB$  and some of these projected states of  $BB$  are kept. The density matrix now tells us which states are the most important. Indeed, for a system which is strongly coupled to the outside universe, it is much more appropriate to use the eigenstates of the density matrix to describe the system rather than the eigenstates of the system’s Hamiltonian. In other words, to analyze which states to be retained, the block is embedded in some environment and the rest of the lattice can be viewed as a heat bath at an effective inverse temperature  $\beta$  to which the system is coupled.

The key idea of DMRG is that rather than keeping the lowest-lying eigenstates of the *Hamiltonian* in forming a new effective Hamiltonian of a block of sites, one should keep the most significant eigenstates of the block *density matrix*, obtained from diagonalizing the Hamiltonian of a larger section of the lattice which includes the block.

In that spirit, keeping the most probable eigenstates of the density matrix gives the most accurate representation of the state of the system as a *whole*, i.e., the block plus the rest of the lattice. This intuition can be understood by considering the expectation value

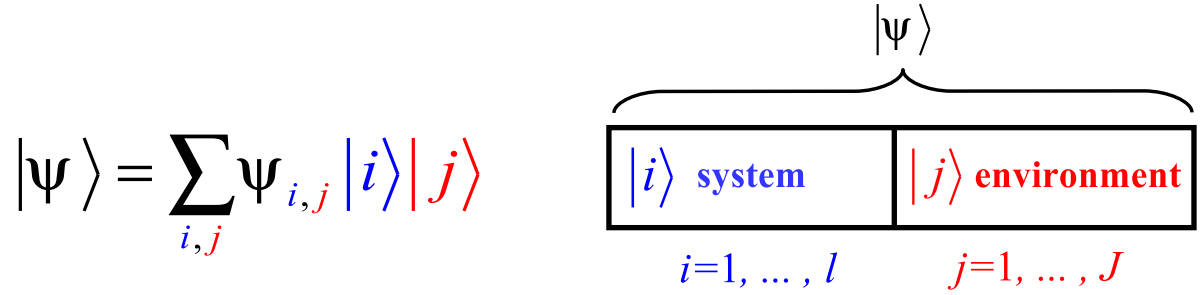


**Figure 2.2:** Sketch of the superblock method as the basis for DMRG.

of an arbitrary operator  $A$  in the basis of the eigenstates of the reduced density matrix of the block

$$\langle A \rangle = \text{Tr}(\rho A) = \sum_{\alpha} w_{\alpha} \langle \nu_{\alpha} | A | \nu_{\alpha} \rangle, \quad (2.3)$$

where  $w_{\alpha}$  are the eigenvalues of the reduced density matrix of the block and  $|\nu_{\alpha}\rangle$  the corresponding eigenvectors. This relation tells us that if for a particular  $\alpha$ ,  $w_{\alpha}$  is very small, we would make accordingly a very small error in expectation value of  $A$  if we discard the state  $|\nu_{\alpha}\rangle$ .

This conclusion that the optimal states to keep are the most probable eigenstates of the block density matrix can be justified rigorously as follows [6]:

Let us assume we have diagonalized a superblock and obtained a particular state  $|\psi\rangle$ , e.g. the ground state. Let  $|i\rangle$  be the complete set of states of the system and  $|j\rangle$  the states of the rest of the superblock, namely the environment, as illustrated in Fig. 2.2. The state of the superblock  $|\psi\rangle$  then admits an expansion of the form

$$|\psi\rangle = \sum_{i,j} \psi_{i,j} |i\rangle |j\rangle. \quad (2.4)$$

We wish to find a procedure for producing a set of states of the system say  $|u^{\alpha}\rangle = \sum_i u_i^{\alpha} |i\rangle$ , and  $\alpha = 1, \dots, m$ , which are optimal for representing  $|\psi\rangle$  in some sense. More precisely, we seek an approximate expansion (with the highest possible accuracy) for  $|\psi\rangle$  of the form

$$|\psi\rangle \approx |\tilde{\psi}\rangle = \sum_{\alpha,j} a_{\alpha,j} |u^{\alpha}\rangle |j\rangle. \quad (2.5)$$

Equivalently, we wish to minimize the error

$$S = \|\psi\rangle - |\tilde{\psi}\rangle\|^2, \quad (2.6)$$

by varying over all  $a_{\alpha,j}$  and  $u^{\alpha}$ , subject to the constraint  $\langle u^{\alpha} | u^{\alpha'} \rangle = \delta_{\alpha\alpha'}$ , since  $|u^{\alpha}\rangle$  forms a complete orthonormal basis. The minimization problem above finds a very compact solution in terms of singular value decomposition from linear algebra

$$\psi = USV^t, \quad (2.7)$$

where  $U$  and  $S$  are  $l \times l$  matrices,  $V$  is an  $J \times l$  matrix,  $U$  is orthogonal,  $V$  is column-orthogonal and the diagonal matrix  $S$  contains the singular values of  $|\psi\rangle$ . In matrix notation this implies an expansion of  $|\psi\rangle$  of the form

$$\psi_{ij} = \sum_{\alpha=1}^m a_{\alpha} u_i^{\alpha} v_j^{\alpha}. \quad (2.8)$$

Now consider what happens if some of the weight factors  $a_{\alpha}$  [ $a_{\alpha} \geq 0$ ] are zero or very small. If that is the case, then  $|\psi\rangle$  can be very well approximated by discarding them that is to say by truncating the sum to those with the largest weights. On the other hand, the density matrix can be expressed in terms of  $U$  and  $S$

$$\rho = |\psi\rangle\langle\psi| = US^2U^t, \quad (2.9)$$

which suggests  $U$  diagonalizes  $\rho$  and the eigenvalues of  $\rho$  are  $w_{\alpha} = a_{\alpha}^2$ . Recalling that  $|\psi\rangle$  could be well approximated by throwing out the smaller  $a_{\alpha}$ 's whose square are now eigenvalues of density matrix, we come up with the conclusion that the optimal states are the eigenstates of  $\rho$  with the largest eigenvalues. Moreover, the deviation of  $P_m \equiv \sum_{\alpha=1}^m w_{\alpha}$  from unity measures the accuracy of the truncation to  $m$  states. A fast decay of density matrix eigenvalues is essential for the performance of this truncation procedure. This is typically fast enough for one-dimensional gapped quantum systems, but for critical systems in one dimension and all systems in higher dimensions may be generically slow [18].

## 2.2 Matrix-product states in the context of strongly correlated systems

States that can be parameterized in terms of products of matrices, i.e. so-called matrix-product states (MPS), were first found in a percolation problem of directed lattice animals in the context of stochastic models [46, 47] and for certain quantum spin chains [48]. They have also been arisen in classical kinetic models, lattice gas and also diffusion-coagulation models [49, 50]. It has been found that the ground state of certain spin-one models and stationary state for classical particles diffusing between two reservoirs have such a form. The analogy between stochastic models and strongly correlated systems may be understood from the formal analogy between a master equation and the Schrödinger equation.

The Matrix-product method in the context of strongly correlated systems was originally devised as a variational approach appropriate to study the ground state and excitations of a variety of one-dimensional lattice systems. In that respect, MPS was used for the construction of the ground state and excitations of 1D or quasi 1D systems in a recursive way, by relating the states of the system with length  $n$  to that of length  $n - 1$ .

In the next section, we illustrate how MPS naturally arises when a renormalization procedure on a one-dimensional system is carried out.

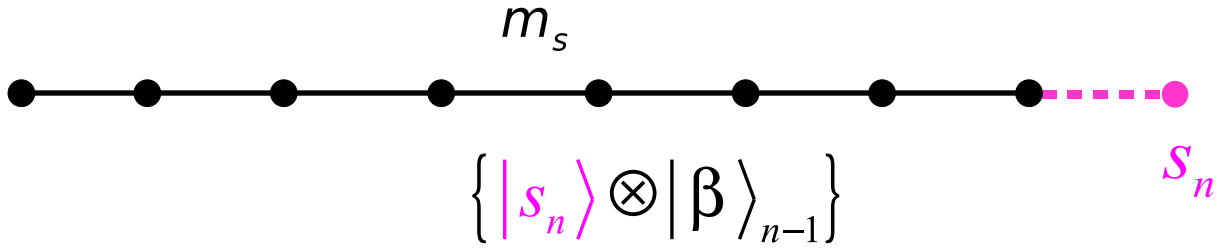


**Figure 2.3:** Renormalization procedure leads to a state of the matrix-product form.

## 2.3 DMRG leads to MPS

Assume we have a block that represents a chain with  $n - 1$  sites, as depicted in Fig. 2.3. Let  $m_s$  be the number of possible states of a single lattice site. If we were to treat this system exactly, there would be  $m_s^{n-1}$  states in the Hilbert space which implies that for large  $n$  the exact treatment of the system will be out of question. Assume, therefore, that an approximation is made and our chain is represented by a smaller set of states labeled by  $\{|\beta\rangle_{n-1}\}$ . This set of states has been chosen by the previous iterations of a renormalization procedure with the aim to describe the low-energy physics. Assume there are  $m$  states in this basis, with  $m \leq m_s^{n-1}$ . If this is the first iteration,  $\{|\beta\rangle_{n-1}\}$  can be the complete basis. We now add a single site, labeled by  $s_n$ , say the  $z$  component of spin, to our block resulting in a new block with  $n$  sites and  $m_s \times m$  states in its basis. The basis states are now generated by the product representation  $\{|s_n\rangle \otimes |\beta\rangle_{n-1}\}$ . We now use a projection operator  $A_n$  to generate a new truncated basis with typically  $m$  states that represent the most important states of the longer new block. We may now observe that the basis associated with block  $n - 1$  and  $n$  are related in a simple manner by the recursion relation of the form

$$|\alpha\rangle_n = \sum_{\beta, s_n} A_n^{\alpha, (\beta, s_n)} |s_n\rangle \otimes |\beta\rangle_{n-1}, \quad (2.10)$$

where the initial data  $|\beta\rangle_0$  should be already supplemented. The matrices  $A_n$  are the variational parameters of the matrix-product method and their determination is the central problem one has to solve. White's DMRG algorithm constitutes a particularly effective way of computing a suitable projection operator  $A_n$  by keeping the largest eigenvalues of the reduced density matrix. More precisely, in DMRG the renormalization scheme offered by singular value decomposition (see Eq. (2.8)) keeps the size of the matrices controllable.

Now if we perform a simple change in notation  $A_n^{\alpha, \beta}[s_n] \equiv A_n^{\alpha, (\beta, s_n)}$  and write the  $m \times (m_s m)$  matrix as a set of  $m_s$   $m \times m$  matrices and also assume that the recursion leads to a fixed point for the projection operator so that we can drop the site-dependence index  $n$ , by recursively applying the renormalization step in the previous equation, the state of

the chain of length  $n$  takes the form [20, 21]

$$|\alpha\rangle_n = \sum_{s_n, \dots, s_1} (A[s_n]A[s_{n-1}] \dots A[s_1])^{\alpha, \beta} |s_n s_{n-1} \dots s_1\rangle \otimes |\beta\rangle_0. \quad (2.11)$$

We thus see that the renormalization procedure results in a wave function that can be written in a matrix-product form.

Note that although the resulting state is the sum of tensor product of the local Hilbert space of each site, the coefficients (product of the  $A$ -matrices) encode the non-trivial correlations throughout the chain.

The MPS arisen in Eq. (2.11), however, corresponds to the first examples in the literature of MPS, with site-independent  $A$ -matrices, but in the rest of the thesis we shall use this nomenclature more generally, i.e. we shall also consider site-dependent  $A$ -matrices.

Quite recently it was understood [51] that NRG, too, in a natural way produces matrix-product states. More precisely, when applied to a Wilson chain of single-impurity Anderson model [24], NRG and DMRG produce approximate ground states of essentially the same MPS structure. This insight puts NRG and DMRG on a common basis. The detailed relation between them will be explored in Chapter 4.

# Chapter 3

## Matrix-product states in the context of quantum information processing

*Note that the concepts introduced in this chapter will be particularly useful for the calculations of our second and third projects presented in Chapter 5 and 6.*

In this Chapter we shall consider a quantum information perspective on matrix-product states. Apart from its own specific field of applicability, it has been recently shown that quantum information theory may also shed light on our understanding of the condensed matter systems and, in particular, on the DMRG and MPS methods [52, 53, 54]. In Section 3.1 a basic definition of MPS is given in terms of valence-bond picture [55]. This will be followed in Sections 3.2 and 3.3 by several algebraic tools which are of crucial importance for obtaining an efficient representation of MPS in the context of quantum information processing. An MPS description of some familiar low-dimensional entangled multiqubit states will be provided in Section 3.4. Finally, the main ideas of sequential generation of states within MPS formalism is presented in Section 3.5.

### 3.1 Definition and graphical representation of MPS

We will throughout consider pure quantum states  $|\psi\rangle \in \mathbb{C}^{\otimes d^n}$  characterizing a system of  $n$  sites, each of which represents a  $d$ -dimensional Hilbert space. For instance, each site could represent a qubit with  $d = 2$ . A description of MPS may be intuitively given in terms of a valence-bond picture which proves useful for understanding multipartite entanglement [23, 55]:<sup>1</sup>

---

<sup>1</sup> This valence-bond-based description of MPS will be in turn useful for the generation of multipartite entangled states studied in Chapter 5 as well as the decomposition of multipartite entangling global

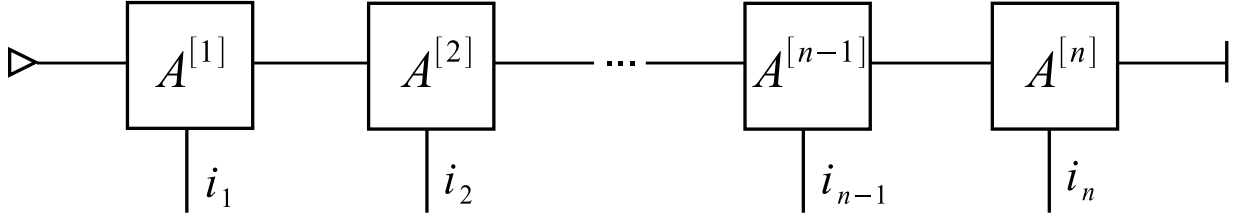


**Figure 3.1:** Graphical representation of an OBC-MPS

We assign two auxiliary sites of dimension  $D_k$ ,  $|\alpha_k, \beta_k\rangle$  to each site of the chain. Assume that every pair of neighboring auxiliary sites are in a maximally entangled state of the form

$$|I\rangle = \sum_{\alpha_1=1}^{D_1} \sum_{\alpha_2=1}^{D_2} \cdots \sum_{\alpha_{n-1}=1}^{D_{n-1}} |\alpha_0, \alpha_1\rangle |\alpha_1, \alpha_2\rangle \cdots |\alpha_{n-1}, \alpha_n\rangle . \quad (3.1)$$

Then if we apply the map

$$\mathcal{A}^{[k]} = \sum_{i_k=1}^d \sum_{\alpha_k, \beta_k=1}^{D_k} A_{i_k, \alpha_k, \beta_k}^{[k]} |i_k\rangle \langle \alpha_k, \beta_k| , \quad (3.2)$$

to each of the  $n$  sites, we are left with a state of a matrix-product form

$$|\psi\rangle = \sum_{i_1, \dots, i_n} A_{i_1}^{[1]} A_{i_2}^{[2]} \cdots A_{i_{n-1}}^{[n-1]} A_{i_n}^{[n]} |i_1 \dots i_n\rangle , \quad (3.3)$$

where  $A_{i_k}^{[k]}$  is a  $D_k \times D_{k+1}$  matrix corresponding to the site  $k \in \{1, \dots, N\}$ . The *bond dimension* of an MPS is defined by

$$D \equiv \max_k D_k . \quad (3.4)$$

A very helpful graphical representation of an MPS is given in Fig. 3.1 and will be heavily used throughout this thesis. Each matrix is represented by a square and the link in between denotes the contraction (sum) over the common indices. In the case of the MPS of Eq. (3.3), the product of the  $A$ -matrices leads to the links (contractions) of the squares in Fig. 3.1. Here  $i_k$  denotes the local state index. In the case of qubits  $i_k = \{0, 1\}$ . Note that  $A_{i_k}^{[k]}$  in Eq. (3.3) are indeed tensors of rank 3 with three indices (see  $A_{i, \alpha, \beta}$  arising in Eq. (3.2)), but for a fixed  $i_k$  we get a matrix (or tensor of rank 2). In other words,  $A_{i, \alpha, \beta}$  encodes the information of  $d$  matrices. Note also that throughout this thesis we only consider MPS with open-boundary conditions (OBC-MPS), which means the first and last matrices of Eq. (3.3) are indeed vectors:  $D_1 = D_{n+1} = 1$ .

---

operations studied in Chapter 6.



It is noteworthy to mention that any state admits such a matrix-product representation obtained by performing successive Schmidt decomposition (or singular value decomposition) on the coefficients of the expansion of the state in the computational basis [53, 26].

In the subsequent sections we will show how the MPS language can be exploited for an efficient representation of multiqubit states.

## 3.2 Schmidt decomposition and singular value decomposition

Quantum systems typically lose their individual identities within a highly correlated *whole* that can not be described by merely the knowledge of its constituents. Nevertheless, there exists a useful construction that provides a transparent description of the relation between the composite system and its constituents given through the Schmidt decomposition [56].

Suppose the composite system  $|\Psi\rangle$  is made of two subsystems  $A$  and  $B$  with which the Hilbert spaces  $\mathcal{H}_A$  and  $\mathcal{H}_B$  are associated, respectively. Then there exist orthonormal bases  $\{|a_i\rangle\} \in \mathcal{H}_A$  and  $\{|b_j\rangle\} \in \mathcal{H}_B$ , such that

$$|\Psi\rangle = \sum_i \lambda_i |a_i\rangle \otimes |b_i\rangle, \quad (3.5)$$

with non-negative scalars  $\lambda_i$  satisfying  $\sum_i \lambda_i = 1$  known as *Schmidt coefficients*. The number of non-vanishing Schmidt coefficients is defined as the *Schmidt rank* of the decomposition. The vectors  $|a_i\rangle$  and  $|b_i\rangle$  are also called the *Schmidt vectors* associated with the partitions  $A$  and  $B$ , respectively.

The decomposition implies that an arbitrary bipartite pure state can be written as a sum of biorthogonal products. Note that the summation in Eq. (3.5) goes over a *single* common index (the smaller of the dimensionalities of Hilbert spaces  $\mathcal{H}_A$  and  $\mathcal{H}_B$ ) whereas in the most general case the sum could go over two indices  $i$  and  $j$  (see Eq. (3.6)).

The Schmidt decomposition theorem can be proved with the aid of singular value decomposition (SVD) as follows [57]:

Let  $\{|c_i\rangle\}$  and  $\{|d_j\rangle\}$  be any fixed orthonormal bases for subsystems  $A$  and  $B$ , respectively. The state of the composite system  $|\Psi\rangle$  can be obviously written as

$$|\Psi\rangle = \sum_{i,j} g_{i,j} |c_i\rangle \otimes |d_j\rangle. \quad (3.6)$$

Treating the coefficients  $g_{ij}$  as a matrix and performing SVD on it yields

$$g = usv, \quad (3.7)$$

where  $u$  and  $v$  are unitary matrices and  $s$  is a diagonal matrix with non-negative elements. Inserting this decomposition for  $g$  in Eq. (3.6) gives

$$|\Psi\rangle = \sum_{i,j,k} u_{ik} s_{kk} v_{kj} |c_i\rangle \otimes |d_j\rangle. \quad (3.8)$$

Making the identifications

$$\begin{aligned} |a_k\rangle &\equiv \sum_i u_{ik} |c_i\rangle \\ |b_k\rangle &\equiv \sum_j u_{kj} |d_j\rangle \\ \lambda_k &\equiv s_{kk} , \end{aligned} \tag{3.9}$$

we arrive at

$$|\Psi\rangle = \sum_k \lambda_k |a_k\rangle \otimes |b_k\rangle , \tag{3.10}$$

which is the Schmidt decomposition of Eq. (3.5). Moreover, it can be easily verified that  $|a_i\rangle$  and  $|b_i\rangle$  in Eq. (3.9) are orthonormal bases

$$\langle a_i | a_{i'} \rangle = \sum_{i, i'} \langle c_i | u_{ki}^* u_{i'k'} | c_{i'} \rangle = \sum_{i, i'} u_{ki}^* u_{i'k'} \delta_{ii'} = \sum_i (u^\dagger)_{ki} u_{ik} = \delta_{kk'} , \tag{3.11}$$

where in the last step use has been made of the unitarity of  $u$ .

### 3.3 Vidal decomposition

Vidal proposed an efficient classical protocol for simulation of slightly entangled pure-state quantum computation on  $n$  qubits which exploits computational resources that grow linearly in  $n$  and exponentially in the amount of entanglement [53]. This decomposition also proves useful in many one-dimensional many-body system, such as quantum spin chains at zero temperature that turn out to contain sufficiently small amount of entanglement to be classically simulatable.

Let us consider the expansion of a  $n$ -qubit state in the computational basis

$$|\Psi\rangle = \sum_{i_1=0}^1 \cdots \sum_{i_n=0}^1 c_{i_1 \dots i_n} |i_1\rangle \otimes \cdots \otimes |i_n\rangle . \tag{3.12}$$

The Vidal decomposition is then given by [53]

$$c_{i_1 i_2 \dots i_n} = \sum_{\alpha_1, \dots, \alpha_{n-1}} \Gamma_{\alpha_1}^{[1]i_1} \lambda_{\alpha_1}^{[1]} \Gamma_{\alpha_1 \alpha_2}^{[2]i_2} \lambda_{\alpha_2}^{[2]} \Gamma_{\alpha_2 \alpha_3}^{[3]i_3} \cdots \Gamma_{\alpha_{n-1}}^{[n]i_n} , \tag{3.13}$$

employing  $n$  tensors (of rank 3)  $\{\Gamma^{[1]}, \dots, \Gamma^{[n]}\}$  and  $n - 1$  vectors  $\{\lambda^{[1]}, \dots, \lambda^{[n-1]}\}$  whose indices take the values in  $\{0, 1\}$  and  $\{1, \dots, \chi\}$ , respectively. Here  $\chi \equiv \max_A \chi_A$ , and  $\chi_A$  denotes the rank of the reduced density matrix in the bipartite splitting of the multipartite state Eq. (3.12). This decomposition essentially re-expresses the  $2^n$  coefficients  $c_{i_1 i_2 \dots i_n}$  of Eq. (3.12) in terms of  $2(n-2)\chi^2 + (n+3)\chi$  parameters.

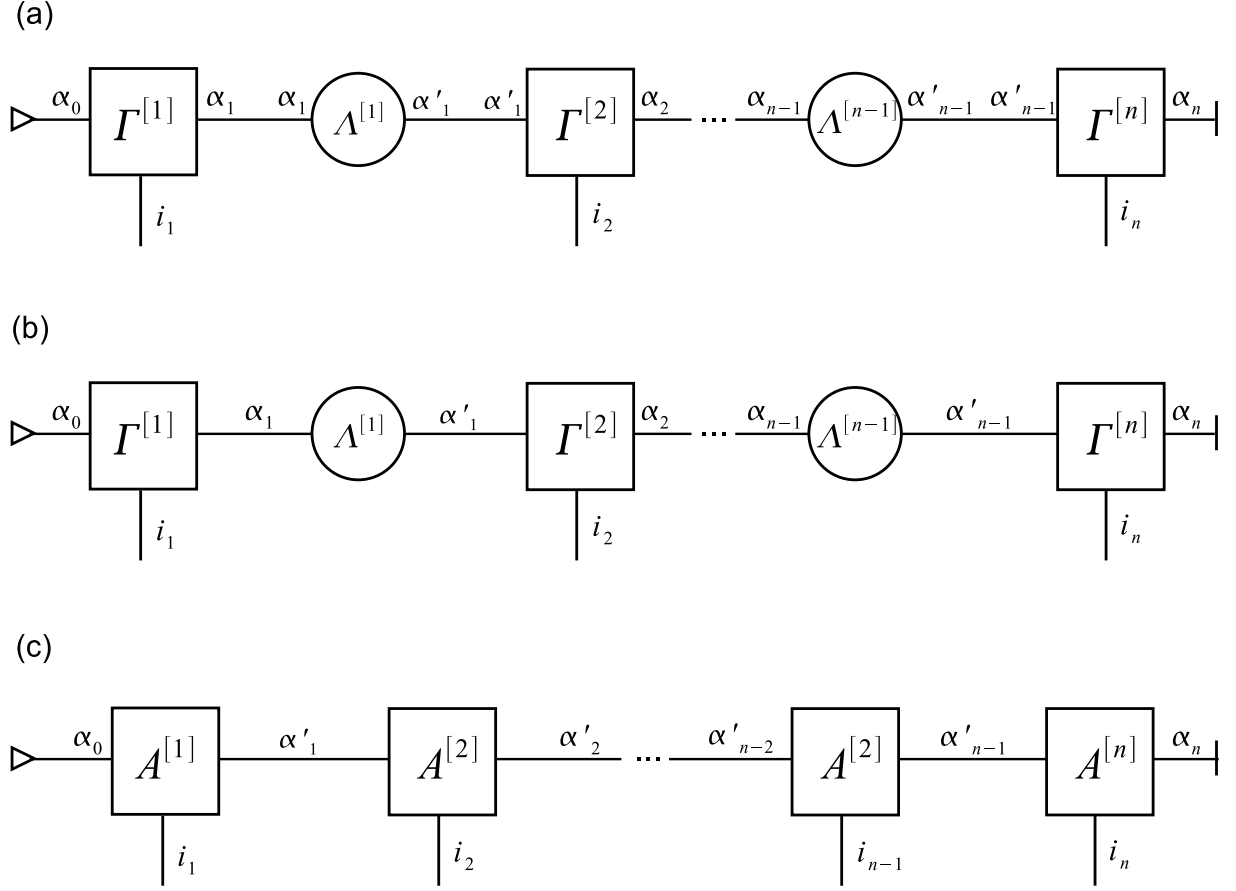


**Figure 3.2:** Graphical representation of the general recipe to arrive at the usual MPS representation of Eq. (3.1) from Vidal decomposition Eq. (3.13) by performing the contractions over the intermediate indices. In (a) the Vidal representation of Eq. (3.3) has been depicted in which tensors  $\Gamma$ 's are shown by squares and the newly defined matrices  $\Lambda$  in Eq. (3.15) by circles. In (b) we have avoided repeating the common indices of the joint links and we would stick to this convention throughout this thesis for all graphical representations of this type. In (c) the contraction between  $\Gamma$ 's and  $\Lambda$ 's are performed and the resulting objects are illustrated by new  $A$  squares, leading to Eq. (3.20).

The decomposition above at the first glance may look different from the standard MPS decomposition introduced by Eq. (3.1) at the beginning of the chapter, but it is easy to show that it can be reshaped into the usual MPS form by performing the contractions between  $\Gamma$ 's and  $\lambda$ 's. To see this, we introduce a new dummy primed index, along with a Kronecker delta

$$\Gamma_{\alpha_{n-1}\alpha_n}^{[n]i_n} \lambda_{\alpha_n}^{[n]} \Gamma_{\alpha_n\alpha_{n+1}}^{[n+1]i_{n+1}} = \sum_{\alpha'_n} \Gamma_{\alpha_{n-1}\alpha_n}^{[n]i_n} \lambda_{\alpha'_n}^{[n]} \delta_{\alpha_n\alpha'_n} \Gamma_{\alpha'_n\alpha_{n+1}}^{[n+1]i_{n+1}}, \quad (3.14)$$

and define the new diagonal matrix  $\Lambda^{[n]}$  of the form

$$\Lambda_{\alpha_n \alpha'_n}^{[n]} \equiv \delta_{\alpha_n \alpha'_n} \lambda_{\alpha'_n}^{[n]} \quad (\text{no sum over } \alpha'_n) . \quad (3.15)$$

Therefore Eq. (3.13) reads

$$c_{i_1 \dots i_n} = \sum_{\alpha_1, \dots, \alpha_{n-1}} \sum_{\alpha'_1, \dots, \alpha'_{n-1}} \Gamma_{\alpha_0 \alpha_1}^{[1]i_1} \Lambda_{\alpha_1 \alpha'_1}^{[1]} \Gamma_{\alpha'_1 \alpha_2}^{[2]i_2} \Lambda_{\alpha_2 \alpha'_2}^{[2]} \Gamma_{\alpha'_2 \alpha_3}^{[3]i_3} \dots \Gamma_{\alpha'_{n-2} \alpha_{n-1}}^{[n-1]i_{n-1}} \Lambda_{\alpha_{n-1} \alpha'_{n-1}}^{[n-1]} \Gamma_{\alpha'_{n-1} \alpha_n}^{[n]i_n} \quad (3.16)$$

with  $\alpha_0 = \alpha_n = 1$ .

Performing the summations (contractions) over the indices  $\{\alpha_1, \alpha_2, \dots, \alpha_{n-1}\}$ , yields

$$c_{i_1 \dots i_n} = \sum_{\alpha'_1, \dots, \alpha'_{n-1}} A_{\alpha_0 \alpha'_1}^{[1]i_1} A_{\alpha'_1 \alpha'_2}^{[2]i_2} \dots A_{\alpha'_{n-2} \alpha'_{n-1}}^{[n-1]i_{n-1}} A_{\alpha'_{n-1} \alpha_n}^{[n]i_n} , \quad (3.17)$$

where we have defined

$$A^{[x]} \equiv \begin{cases} \Gamma^{[n]} & \text{for } x = n , \\ \sum_{\alpha_x} \Gamma^{[x]} \Lambda^{[x]} & \text{otherwise .} \end{cases} \quad (3.18)$$

If we also perform further summations over the indices  $\{\alpha'_1, \alpha'_2, \dots, \alpha'_{n-1}\}$ , we arrive at

$$c_{i_1 \dots i_n} = A^{[1]i_1} A^{[2]i_2} \dots A^{[n-1]i_{n-1}} A^{[n]i_n} , \quad (3.19)$$

which when inserted in Eq. (3.13) yields

$$|\Psi\rangle = \sum_{i_1, \dots, i_n=0}^1 A^{[1]i_1} A^{[2]i_2} \dots A^{[n-1]i_{n-1}} A^{[n]i_n} |i_1\rangle \otimes |i_2\rangle \otimes \dots \otimes |i_n\rangle , \quad (3.20)$$

which is nothing but the standard representation of the MPS in Eq. (3.3). The graphical representation of the procedure above has been depicted schematically in Fig. 3.2.

All in all, we may conclude that the Vidal decomposition offers a general recipe for the MPS representation of *any arbitrary* state. On the other hand, this decomposition also allows to define a *canonical* representation of MPS given by the following theorem [23]:

**THEOREM** (canonical representation of an MPS): Any state  $|\psi\rangle \in \mathbb{C}^{\otimes d^n}$  has an OBC-MPS representation of the form Eq. (3.3) with bond dimension  $D \leq d^{\lfloor n/2 \rfloor}$  and

1.  $\sum_i A_i^{[m]} A_i^{[m]\dagger} = \mathbb{1}_{D_m}$  for all  $1 \leq m \leq n$ .
2.  $\sum_i A_i^{[m]\dagger} \Lambda^{[m-1]} A_i^{[m]} = \Lambda^{[m]}$  for all  $1 \leq m \leq n$ .
3.  $\Lambda^{[0]} = \Lambda^{[n]} =$  and each  $\Lambda^{[m]}$  is a  $D_{m+1} \times D_{m+1}$  diagonal matrix which is positive, full-rank and with  $\text{Tr}(\Lambda^{[m]}) = 1$

This theorem is proven in Ref. [53] by successive singular value decompositions in  $|\psi\rangle$ . If the *gauge conditions* 1.-3. are satisfied for an MPS, then the MPS is said to be in the *canonical* form [23].

### 3.4 Prototypical low-dimensional MPS in quantum information theory

The generation and manipulation of multipartite entanglement lies at the very heart of quantum mechanics. Among the various kinds of entangled multiqubit states, the  $W$  state [29, 58, 59] plays a distinguished role and provides a test-bed for theoretical studies of multipartite entanglement, as their entanglement is believed to be maximally persistent and robust under particle loss [60, 61]. A scalable and deterministic generation of up to eight-particle entangled states of the  $W$  type with trapped ions has recently been reported in Innsbruck [61].

A  $W$ -state of  $n$  qubits is defined by

$$|W_n\rangle = \frac{1}{\sqrt{n}}(|10\dots 0\rangle + |010\dots 0\rangle + \dots |00\dots 01\rangle), \quad (3.21)$$

with equal superposition of all permutations of  $|10\dots 0\rangle$ . Since states of this type are believed to be immune against global dephasing and rather robust against bit flip noise, they are suitable candidates for quantum communication tasks [62, 63].

Another type of highly entangled states of multiple quantum systems is Greenberger-Horne-Zeilinger state (GHZ) [28]. They are equal superpositions of two maximally different states. A GHZ state of  $n$  qubits is given by

$$|\text{GHZ}_n\rangle = \frac{1}{\sqrt{2}}(|11\dots 1\rangle + |00\dots 0\rangle). \quad (3.22)$$

Creation of GHZ states with up to six ions have been recently realized in Boulder [64].

It is worth to mention that the  $W$  and GHZ states both can be represented with MPS with bond-dimension  $D = 2$  for *any* number of qubits  $n$ . As an illustrative case, we now demonstrate explicitly [27] how to obtain such a canonical representation of these paradigmatic multipartite states for  $n = 3$  by employing the Vidal decomposition introduced in the previous section.

We first consider the  $W$  state with three qubits given by

$$|W_3\rangle = c_1|\downarrow\downarrow\uparrow\rangle + c_2|\downarrow\uparrow\downarrow\rangle + c_3|\uparrow\downarrow\downarrow\rangle. \quad (3.23)$$

The Vidal decomposition of such state according to Eq. (3.13) is given by

$$|W_3\rangle = \sum_{i_1, i_2, i_3} \left( \sum_{\alpha_1, \alpha_2} \Gamma_{\alpha_1}^{[1]i_1} \lambda_{\alpha_1}^{[1]} \Gamma_{\alpha_1 \alpha_2}^{[2]i_2} \lambda_{\alpha_2}^{[2]} \Gamma_{\alpha_2}^{[3]i_3} \right) |i_1 i_2 i_3\rangle. \quad (3.24)$$

The aim is now to find the set of tensors  $\{\Gamma^{[1]}, \Gamma^{[2]}, \Gamma^{[3]}\}$  and vectors  $\{\lambda^{[1]}, \lambda^{[2]}\}$ . We start by performing the Schmidt decomposition of such state for the partition 1|23 given by

$$|W_3\rangle = N_\uparrow |\uparrow\rangle \underbrace{\frac{c_3}{N_\uparrow} |\downarrow\downarrow\rangle}_{|\Phi_\uparrow^{[23]}\rangle} + N_\downarrow |\downarrow\rangle \underbrace{\left[ \frac{c_1}{N_\downarrow} |\downarrow\uparrow\rangle + \frac{c_2}{N_\downarrow} |\uparrow\downarrow\rangle \right]}_{|\Phi_\downarrow^{[23]}\rangle}, \quad (3.25)$$

where  $|\Phi_\uparrow^{[23]}\rangle$  and  $|\Phi_\downarrow^{[23]}\rangle$  are the Schmidt vectors of the subsystems corresponding to qubits 2 and 3.  $N_\uparrow$  and  $N_\downarrow$  are the Schmidt coefficients in our case given by  $N_\uparrow^2 = c_3^2$  and  $N_\downarrow^2 = c_1^2 + c_2^2$ . Comparing Eq. (3.25) with the Vidal decomposition of the partition 1|23

$$|W_3\rangle = \sum_{i_1, \alpha_1} \Gamma_{\alpha_1}^{[1]i_1} \lambda_{\alpha_1}^{[1]} |i_1\rangle |\Phi_{\alpha_1}^{[23]}\rangle = \lambda_\uparrow^{[1]} \Gamma_\uparrow^{[1]\uparrow} |\uparrow\rangle |\Phi_\uparrow^{[23]}\rangle + \lambda_\downarrow^{[1]} \Gamma_\downarrow^{[1]\uparrow} |\uparrow\rangle |\Phi_\downarrow^{[23]}\rangle \\ + \lambda_\uparrow^{[1]} \Gamma_\uparrow^{[1]\downarrow} |\downarrow\rangle |\Phi_\uparrow^{[23]}\rangle + \lambda_\downarrow^{[1]} \Gamma_\downarrow^{[1]\downarrow} |\downarrow\rangle |\Phi_\downarrow^{[23]}\rangle, \quad (3.26)$$

gives

$$\lambda^{[1]} = (N_\uparrow, N_\downarrow); \quad \Gamma^{[1]\uparrow} = (1, 0); \quad \Gamma^{[1]\downarrow} = (0, 1). \quad (3.27)$$

Proceeding with the Schmidt decomposition of partition 12|3 yields

$$|W_3\rangle = N_{12,\uparrow} \frac{c_1}{N_{12,\uparrow}} |\downarrow\downarrow\rangle \underbrace{|\uparrow\rangle}_{|\Phi_{12,\uparrow}^{[3]}\rangle} + N_{12,\downarrow} \left[ \frac{c_2}{N_{12,\downarrow}} |\downarrow\uparrow\rangle + \frac{c_3}{N_{12,\downarrow}} |\uparrow\downarrow\rangle \right] \underbrace{|\downarrow\rangle}_{|\Phi_{12,\downarrow}^{[3]}\rangle}, \quad (3.28)$$

with Schmidt coefficients  $N_{12,\uparrow}^2 = c_1^2$  and  $N_{12,\downarrow}^2 = c_2^2 + c_3^2$ . Again comparing with the Vidal decomposition of the partition 12|3, in a similar manner to that of 1|23 above, yields

$$\lambda^{[2]} = (N_{12,\uparrow}, N_{12,\downarrow}); \quad \Gamma^{[2]\uparrow} = \begin{pmatrix} 0 & 0 \\ 0 & \frac{1}{N_\uparrow} \end{pmatrix} \quad \Gamma^{[2]\downarrow} = \begin{pmatrix} 0 & \frac{1}{N_\uparrow} \\ \frac{1}{N_\downarrow} & 0 \end{pmatrix}. \quad (3.29)$$

The remaining  $\Gamma_{\alpha_2}^{[3]i_3}$  may be easily read off from the previous Schmidt decomposition of the state

$$\Gamma^{[3]\uparrow} = \begin{pmatrix} 1 \\ 0 \end{pmatrix} \quad \Gamma^{[3]\downarrow} = \begin{pmatrix} 0 \\ 1 \end{pmatrix}. \quad (3.30)$$

In general, one may verify that

$$\Gamma_{\alpha_{n-1}\alpha_n}^{[n]i_n} = \langle \alpha_{n-1} i_n | \alpha_n \rangle \frac{1}{\lambda_{\alpha_{n-1}}^{[n-1]}}. \quad (3.31)$$

The construction already indicates the minimal bond dimension of the MPS representation of  $W$  state is  $D = 2$ , since this is the maximal rank of Schmidt decomposition of the multipartite state over all possible bipartite splittings  $A|B$  of the three qubits,  $\chi = \max_A \chi_A = 2$ .

In a similar manner, the same construction for a GHZ state of three qubits

$$|\text{GHZ}_3\rangle = c_1 |\uparrow\uparrow\uparrow\rangle + c_2 |\downarrow\downarrow\downarrow\rangle, \quad (3.32)$$

yields

$$\begin{aligned} \lambda^{[1]} &= (N_\uparrow, N_\downarrow) & \lambda^{[2]} &= (N_{12,\uparrow}, N_{12,\downarrow}) \\ \Gamma^{[1]\uparrow} &= (1, 0) & \Gamma^{[1]\downarrow} &= (0, 1) \\ \Gamma^{[2]\uparrow} &= \begin{pmatrix} \frac{1}{N_\uparrow} & 0 \\ 0 & 0 \end{pmatrix} & \Gamma^{[2]\downarrow} &= \begin{pmatrix} 0 & 0 \\ 0 & \frac{1}{N_\downarrow} \end{pmatrix} \\ \Gamma^{[3]\uparrow} &= \begin{pmatrix} 1 \\ 0 \end{pmatrix} & \Gamma^{[3]\downarrow} &= \begin{pmatrix} 0 \\ 1 \end{pmatrix}, \end{aligned} \quad (3.33)$$

where  $N_{12,\uparrow} = N_\uparrow = c_1$  and  $N_{12,\downarrow} = N_\downarrow = c_2$ . Again we end up with matrices of maximal dimensions  $D = 2$  for the MPS representation of a GHZ state with  $n = 3$ .

A similar construction may be easily generalized to any number of qubits  $n$ , and in all cases, we observe that any bipartite decomposition of the state gives a Schmidt rank of  $\chi = 2$ , which accounts for the fact that GHZ and  $W$  states with any number of qubits  $n$  can be described by MPS of *optimal* bond dimension  $D = 2$ .

### 3.5 MPS for sequential generation of entangled multiqubit states

The generation of multiqubit entangled states via a single global unitary operation acting on initially decoupled qubits is in general known to be a difficult problem. Therefore, several theoretical and experimental efforts have been made to develop *sequential* protocols for the generation of paradigmatic entangled multiqubit states [26, 31, 32]. Sequentiality can in principle enormously reduce the complexity in the physical implementation of a global operation [39].

A complete characterization of all multipartite quantum states achievable within a sequential generation scheme was provided by Schön *et al* in terms of matrix-product states [26, 31, 32]. They considered a trapped  $D$ -level atom coupled to a cavity qubit with energy eigenstates  $|0\rangle$  and  $|1\rangle$ . The ancilla performs arbitrary bipartite source-qubit interactions with each qubit in a row, creating the desired entangled multiqubit state (see Fig. 3.3). The role of the ancillary system, in practice, is performed by a  $D$ -level atom coupled to a single mode of an optical cavity. The sequentially generated qubits describe the absence  $|0\rangle$  or presence  $|1\rangle$  of a photon emitted from the cavity in a certain time interval.

Assuming that all qubits are initially in  $|0\rangle$ , the ancilla-qubit interaction may be described in the form of an isometry  $V = \sum_{i,\alpha,\beta} V_{\alpha,\beta}^i |\alpha, i\rangle \langle \beta|$  with  $\{\alpha, \beta\}$  denoting the ancilla levels. Applying  $n$  ancilla operations of this type on some initial state of the ancilla  $|\phi_I\rangle$  in

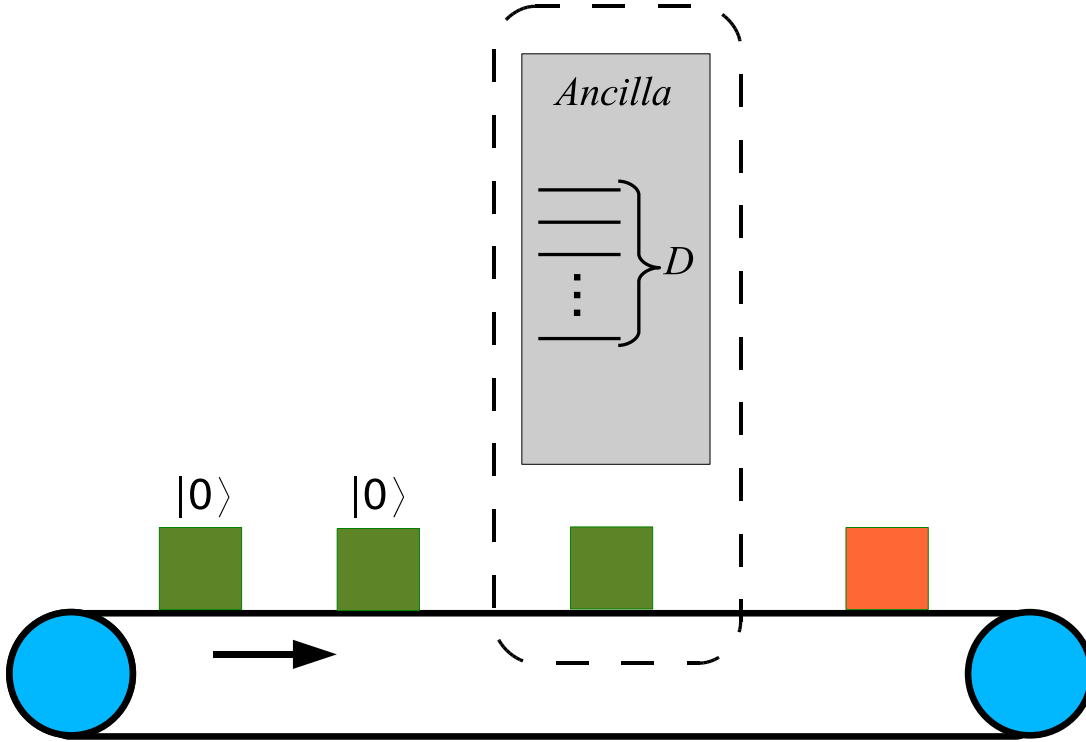


**Figure 3.3:** Sequential “quantum factory” of states. A trapped  $D$ -level atom as an itinerant ancilla performs bipartite interactions with a sequence of initially uncorrelated qubits. After ancilla-qubit operations, the qubits will be in general entangled with the ancilla as well as among themselves.

a sequential manner, gives rise to the state of the joint system (ancilla+qubit) of the form

$$|\Psi\rangle = V_{[n]} \dots V_{[2]} V_{[1]} |\phi_I\rangle. \quad (3.34)$$

Assuming that the ancilla decouples in the last step from the  $n$ -qubit system, such that  $|\Psi\rangle = |\phi_F\rangle \otimes |\psi\rangle$  with  $|\phi_F\rangle$  being some final state of the ancilla, the qubits end up in a state of matrix-product form [31]

$$|\psi\rangle = \sum_{i_n \dots i_1=0}^1 \langle \phi_F | V_{[n]}^{i_n} \dots V_{[1]}^{i_1} | \phi_I \rangle |i_n, \dots, i_1\rangle. \quad (3.35)$$

Note that the optimal ancilla dimension is given by the bond dimension of the canonical MPS representation of  $|\psi\rangle$ .

Moreover, it was shown in Ref. [31] that the converse is also true, i.e. every open-boundary MPS of the form

$$|\psi\rangle = \sum_{i_n \dots i_1=0}^1 \langle \phi_F | A_{[n]}^{i_n} \dots A_{[1]}^{i_1} | \phi_I \rangle |i_n, \dots, i_1\rangle, \quad (3.36)$$



---

with arbitrary maps  $A$ , not necessarily isometries, can be generated sequentially by isometries of the same dimension and such that the ancilla decoupled in the last step.

The physical implementation of the outlined sequential recipe within cavity QED setup [65, 66, 67] is detailed in Ref. [32].

It is noteworthy to mention that the extension of the family of sequentially generated matrix-product states to two dimensions has also been recently investigated in Ref. [68].



# Part II

## Results



# Chapter 4

## Matrix-product-state comparison of the numerical renormalization group and the variational formulation of the density-matrix renormalization group

*This chapter, together with Appendices A, B, D have been published in Physical Review B:*

H. Saberi, A. Weichselbaum, and J. von Delft, Phys. Rev. B **78**, 035124 (2008).

### 4.1 Introduction

Wilson's numerical renormalization group (NRG) is a highly successful method for solving quantum impurity models which allows the non-perturbative calculation of static and dynamic properties for a variety of impurity models [2, 3, 4, 69, 70, 71, 72, 73, 74]. NRG is formulated on a "Wilson chain", i.e. a tight-binding fermionic quantum chain with hopping matrix elements that decrease exponentially along the chain as  $\Lambda^{-n/2}$ , where  $\Lambda > 1$  is a discretization parameter defined below and  $n \geq 0$  is the chain's site index. It is thus not applicable to real space quantum lattice problems featuring constant hopping matrix elements. For these, White's density-matrix renormalization group (DMRG) is the method of the choice [5, 6, 7, 8]. It has been known for some time [20, 21, 22] that the approximate ground states produced by DMRG have the form of matrix-product states (MPS) (see Eq. (4.7) below) that had previously arisen in certain stochastic models [50] and quantum information processing [75]. This fact can be exploited to reinterpret the DMRG algorithm (more precisely, its one-site finite-size version) as a variational optimization scheme, in which the ground state energy is minimized in the space of all matrix-product states

with specified dimensions [22, 76, 52]. To emphasize this fact, we shall refer to DMRG as “variational matrix-product state” (VMPS) approach throughout this thesis.

Quite recently it was understood [51] that NRG, too, in a natural way produces matrix-product states. In other words, when applied to the same Wilson chain, NRG and VMPS produce approximate ground states of essentially the same MPS structure. The two approximate ground states are not identical, though, since the two methods use different truncation schemes to keep the size of the matrices involved manageable even for very long Wilson chains: NRG truncation relies on energy scale separation, which amounts to discarding the highest-energy eigenstates of a sequence of effective Hamiltonians, say  $\mathcal{H}_n$ , describing Wilson chains of increasing length  $n$  and yielding spectral information associated with the energy scale  $\Lambda^{-n/2}$ . This truncation procedure relies on the exponential decrease of hopping matrix elements along the Wilson chain, which ensures that adding a new site to the Wilson chain perturbs it only weakly. In contrast, VMPS truncation relies on singular value decomposition of the matrices constituting the MPS, which amounts to discarding the lowest-weight eigenstates of a sequence of reduced density matrices [6]. This procedure makes no special demands on the hopping matrix elements, and indeed works also if they are all equal, as is the case of standard quantum chain models for which DMRG was designed.

The fact that a *Wilson chain* model can be treated by two related but nonequivalent methods immediately raises an interesting and fundamental methodological question: How do the two methods compare? More precisely, to what extent and under which circumstances do their results agree or disagree? How do the differences in truncation schemes manifest themselves? VMPS, being a variational method operating in the same space of states as NRG, will yield a lower-energy ground state than NRG. However, it variationally targets *only* the ground state for the full Wilson chain, of length  $N$ , say. In contrast, NRG produces a set of eigenenergies  $\{E_\beta^n\}$  and eigenstates  $\{|E_\beta^n\rangle\}$  for each of the sequence of effective Hamiltonians  $\mathcal{H}_n$ , with  $n \leq N$ , mentioned above. From these, a wealth of information about the RG flow, fixed points, relevant and irrelevant operators, their scaling dimensions, as well as static and dynamic physical properties can be extracted. Are these accessible to VMPS, too?

The goal of this chapter is to explore such questions. We shall exploit the common matrix-product state structure of the NRG and VMPS approaches to perform a systematic comparison of these two methods, as applied to the single-impurity Anderson model [24]. It should be emphasized that our purpose is not to advocate using one method instead of the other. Instead, we hope to arrive at a balanced assessment of the respective strengths and weaknesses of each method.

In a nutshell, the main conclusion (which confirms and extends the results of Ref. [51]) is the following: when applied to a Wilson chain with exponentially decreasing hopping, the VMPS approach is able to fully reproduce *all* information obtainable from NRG, despite being variationally optimized with respect to the ground state only. The reason is that the VMPS ground state is characterized by products of matrices of the form  $\prod_{n=0}^N B^{[\sigma_n]}$  (details will be explained below), where the matrices with the same index  $n$  contain information

about the energy scale  $\Lambda^{-n/2}$ . As will be shown below, this information can be used to construct eigenenergies  $\{E_\beta^n\}$  and eigenstates  $\{|E_\beta^n\rangle\}$  for a sequence of effective Hamiltonians  $\mathcal{H}_n$  in *complete* analogy with (but not identical to) those of NRG. The agreement between NRG and VMPS results for these eigenenergies and eigenstates is excellent quantitatively, provided sufficient memory resources are used for both (and  $\Lambda$  is not too close to 1, see below). In this sense, NRG and VMPS can be viewed as yielding essentially equivalent results when applied to Wilson chains amenable to NRG treatment. In particular, *all* physical properties obtainable from the eigenspectra and eigenstates of NRG can likewise be obtained from those of VMPS.

Nevertheless, NRG and VMPS do differ in performance, flexibility and numerical cost. First, since NRG truncation relies on energy scale separation, it works well only if the discretization parameter  $\Lambda$  is not too close to 1 (although the continuum limit of the model is recovered only in the limit  $\Lambda \rightarrow 1$ ). This restriction does not apply to VMPS. Indeed, we shall find that NRG and VMPS agree well for  $\Lambda = 2.5$ , but less well for  $\Lambda = 1.5$ . This in itself is not surprising. However it does illustrate the power of VMPS to get by without energy scale separation. This very useful feature can be exploited, for example, to obtain resolve sharp spectral features at high energies in dynamical correlation functions [51], using projection operator techniques. However, the latter results go beyond the scope of the present work and will be published separately.

Second, since VMPS does not rely on energy scale separation, it does not need to treat all terms in the Hamiltonian characterized by the same scale  $\Lambda^{-n/2}$  at the same time, as is required for NRG. This allows VMPS to achieve a significant reduction in memory cost compared to NRG for representing the ground state. To be specific: For NRG, we use the standard “folded” representation of the Wilson chain, in which each site represents both spin down and spin up electrons, with the impurity site at one end (see Fig. 4.1(a) below). However, it turns out that apart from the first few sites of the folded chain, the spin-down and -up degrees of freedom of each site are effectively not entangled with each other at all (see Fig. 4.3 below). For VMPS, we exploit this fact by using an “unfolded” representation of the Wilson chain instead [77, 51], in which the spin up and spin down sites lie on opposite sides of the impurity site, which sits at the center of the chain (see Fig. 4.1(b) below). This unfolded representation greatly reduces the memory cost, as characterized by the dimensions,  $D$  for NRG or  $D'$  for VMPS, of the effective Hilbert spaces needed to capture the low energy properties with the same precision: We find that with the choice  $D' = 2^m \sqrt{D}$ , VMPS can reproduce the results of NRG in the following manner: (i) if  $m = 0$ , the NRG ground state is reproduced qualitatively; (ii) if  $m = 1$ , all the “kept” states of NRG are reproduced quantitatively; and (iii) if  $m = 2$  all the “kept” *and* “discarded” states of NRG are reproduced quantitatively. However, in cases (ii) and (iii) the reduction in memory costs of VMPS is somewhat offset by the fact that the calculation of the excited eigenstates needed for the sake of direct comparison with NRG requires diagonalizing matrices of effective dimension  $D'^2$ . Note, nevertheless, that all information needed for this comparison is already fully contained within the VMPS *ground state* characterized by dimension  $D'$ , since its constituent matrices contain information

from all energy scales represented by the Wilson chain.

The chapter is organized as follows: Section 4.2 sets the scene by introducing a folded and an unfolded version of the Wilson chain. In Sections 4.3 and 4.4 we review the NRG and VMPS approaches for finding the ground state of a folded or unfolded Wilson chain, respectively, emphasizing their common matrix-product state structure. We also explain how an unfolded MPS states may be “refolded”, allowing it to be compared directly to folded NRG states. In Section 4.5 we compare the results of NRG and VMPS, for ground state energies and overlaps (Section 4.5.1), excited state eigenenergies and density of states (Section 4.5.2), and the corresponding energy eigenstates themselves (Section 4.5.3). This allows us, in particular, to obtain very vivid insights into the differences in the truncation criteria used by the NRG and VMPS approaches, being sharp or smooth in energy space, respectively (Figs. 4.8 to 4.10). In Section 4.6 we demonstrate that NRG results for the ground state can be improved upon systematically by first producing an unfolded “clone” of a given NRG ground state, and subsequently lowering its energy by performing variational energy minimization sweeps in the space of variational matrix-product states. Finally, Section 4.7 contains our conclusions and an assessment of the relative pros and cons of NRG and VMPS in relation to each other.

## 4.2 Folded and unfolded representations of Wilson chain

For definiteness, we consider the single-impurity Anderson model. It describes a spinful fermionic impurity level with energy  $\epsilon_d$  and double occupancy cost  $U$  (with associated creation operators  $f_{0\mu}^\dagger$ , where  $\mu = \downarrow, \uparrow$  denotes spin), which acquires a level width  $\Gamma$  due to being coupled to a spinful fermionic bath with bandwidth  $W = 1$ . Since the questions studied in this work are of a generic nature and do not depend much on the specific parameter values used, we consider only the symmetric Anderson model and take  $U = \frac{1}{2}$ ,  $U/\pi\Gamma = 1.013$  and  $\epsilon_d = -\frac{1}{2}U$  throughout this chapter. To achieve a separation of energy scales, following Wilson [2, 3], the bath is represented by a set of discrete energy levels with logarithmically spaced energies  $\Lambda^{-n}$  (with associated creation operators  $f_{n\mu}^\dagger$ ), where  $n \geq 1$ ,  $\Lambda > 1$  is a “discretization parameter”, and the limit  $\Lambda \rightarrow 1$  reproduces a continuous bath spectrum. The discretized Anderson model Hamiltonian can then be represented as

$$\mathcal{H}_{\text{AM}} = \lim_{N \rightarrow \infty} \mathcal{H}_N, \quad (4.1)$$

where  $\mathcal{H}_N$  describes a Wilson chain of “length  $N$ ” (i.e., up to and including site  $N$ ):

$$\mathcal{H}_N = \mathcal{H}_{N\downarrow} + \mathcal{H}_{N\uparrow} + U(f_{0\uparrow}^\dagger f_{0\uparrow} f_{0\downarrow}^\dagger f_{0\downarrow} + \frac{1}{2}), \quad (4.2a)$$

$$\mathcal{H}_{N\mu} = \epsilon_d f_{0\mu}^\dagger f_{0\mu} + \sum_{n=0}^{N-1} t_n (f_{n\mu}^\dagger f_{(n+1)\mu} + \text{h.c.}), \quad (4.2b)$$



with hopping coefficients given by

$$\begin{aligned}
t_n &\equiv \begin{cases} \sqrt{\frac{2\Gamma}{\pi}} & \text{for } n = 0, \\ \frac{1}{2}(1 + \Lambda^{-1})\Lambda^{-(n-1)/2}\xi_n & \text{for } n \geq 1, \end{cases} \\
\xi_n &= (1 - \Lambda^{-n})(1 - \Lambda^{-2n+1})^{-1/2}(1 - \Lambda^{-2n-1})^{-1/2}.
\end{aligned} \tag{4.3}$$

In passing, we note that for our numerics we have found it convenient (following Refs. [77] and [51]) to keep track of fermionic minus signs by making a Jordan-Wigner transformation [78] of the Wilson chain to a spin chain, using  $f_{n\mu}^\dagger = P_{n\mu}s_{n\mu}^+$  and  $f_{n\mu} = P_{n\mu}s_{n\mu}^-$ . Here  $s_{n\mu}^\pm$  are a set of spin- $\frac{1}{2}$  raising and lowering operators, that for equal indices satisfy  $\{s_{n\mu}^-, s_{n\mu}^+\} = 1$ ,  $(s_{n\mu}^-)^2 = (s_{n\mu}^+)^2 = 0$ , but commute if their indices are unequal. The fermionic anticommutation relations for the  $f_{n\mu}$  are ensured by the operators  $P_{n\mu} = (-1)^{\sum_{(\bar{n}\bar{\mu}) < (n\mu)} s_{\bar{n}\bar{\mu}}^+ s_{\bar{n}\bar{\mu}}^-}$ , where  $<$  refers to some implicitly specified ordering for the composite index  $(n\mu)$ . The  $P_{n\mu}$  need to be kept track of when calculating certain correlation functions, but do not arise explicitly in the construction of the matrix-product states that are the focus of this work. This transformation will implicitly be assumed to have been implemented throughout the ensuing discussion.

For the Anderson model, site  $n$  of the Wilson chain represents the set of four states  $|\sigma_n\rangle$ , with  $\sigma_n = (\sigma_{n\downarrow}, \sigma_{n\uparrow}) \in \{(00), (10), (01), (11)\}$ , where  $\sigma_{n\mu} \in \{0, 1\}$ , to be viewed as eigenvalue of  $s_{n\mu}^+ s_{n\mu}^-$ , gives the occupancy on site  $n$  of electrons with spin  $\mu$ . Thus, the dimension of the spinful index  $\sigma_n$  is  $d = 4$ , and that of the spin-resolved index  $\sigma_{n\mu}$  is  $d' = 2$ . As a general rule, we shall use the absence or presence of primes,  $d$  vs.  $d'$  (and  $D$  vs.  $D'$  below), to distinguish dimensions referring to spinful or spin-resolved indices, respectively, and correspondingly to folded or unfolded representations of the Wilson chain. For other quantum impurity models, such as the Kondo model or multilevel Anderson models, the dimension of the local impurity site, say  $d_0$ , differs from that of the bath sites,  $d_0 \neq d$ . It is straightforward to generalize the discussion below accordingly.

The Hamiltonian  $\mathcal{H}_N$  of a Wilson chain of length  $N$  is defined on a Hilbert space of dimension  $d^{N+1}$ . It is spanned by an orthonormal set of states that, writing  $|\sigma_n\rangle = |\sigma_{n\downarrow}\rangle|\sigma_{n\uparrow}\rangle$ , can be written in either spinful or spin-resolved form,

$$|\boldsymbol{\sigma}^N\rangle = |\sigma_0\rangle|\sigma_1\rangle \dots |\sigma_N\rangle, \tag{4.4a}$$

$$= |\sigma_{0\downarrow}\rangle|\sigma_{0\uparrow}\rangle|\sigma_{1\downarrow}\rangle|\sigma_{1\uparrow}\rangle \dots |\sigma_{N\downarrow}\rangle|\sigma_{N\uparrow}\rangle, \tag{4.4b}$$

corresponding to a ‘‘folded’’ or ‘‘unfolded’’ representation of the Wilson chain, illustrated by Figs. 4.1(a) or (b), respectively. The unfolded representation of Fig. 4.1(b) makes explicit that the Anderson Hamiltonian of Eq. (4.2) has the form of two separate Wilson chains of specified spin, described by  $\mathcal{H}_{N\downarrow}$  and  $\mathcal{H}_{N\uparrow}$ , *which interact only at site zero*. This fact will be exploited extensively below. Note that the ordering chosen for the  $|\sigma_{n\mu}\rangle$  states in Eq. (4.4b) fixes the structure of the many-body Hilbert space once and for all. The fact that the sites of the unfolded chain in Fig. 4.1 are connected in a different order than that specified in Eq. (4.4b) is a statement about the dynamics of the model and of no consequence at this stage, where we simply fix a basis.

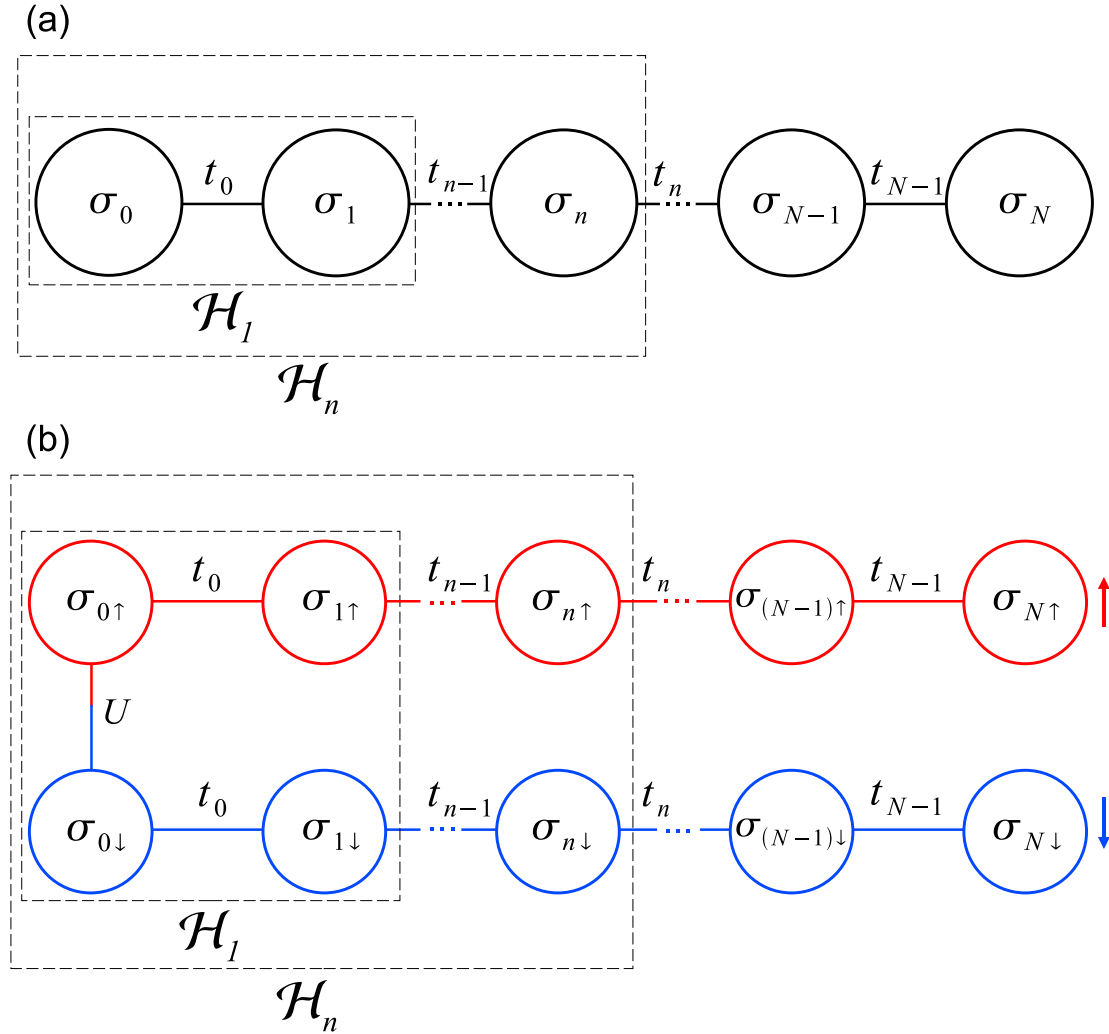


**Figure 4.1:** (a) The standard spinful or “folded” representation of the Wilson chain of the single-impurity Anderson model, and (b) its spin-resolved or “unfolded” representation. The latter makes explicit that spin-down and -up states are coupled *only* at the impurity sites and not at any of the bath sites. The dashed boxes indicate the chains described by  $\mathcal{H}_1$  and  $\mathcal{H}_n$ , respectively.

### 4.3 NRG treatment of folded Wilson chain

#### 4.3.1 NRG matrix-product state arises by iteration

Wilson proposed to diagonalize the folded Wilson chain numerically using an iterative procedure, starting from a short chain and adding one site at a time. Consider a chain of length  $n$ , sufficiently short that  $\mathcal{H}_n$  can be diagonalized exactly numerically. Denote

its eigenstates by  $|E_\alpha^n\rangle_f$ , ordered by increasing energy  $(E_\alpha^n)_f$ , with  $\alpha = 1, \dots, D_n$  and  $D_n = d^{n+1}$ . (We use subscripts f and u to distinguish quantities obtained from a folded or unfolded Wilson chain, respectively; similarly, in later parts of the chapter we will use the subscripts r and c for “refolded” and “cloned”.) E.g., for a chain consisting of only the impurity site,  $n = 0$ , the  $d$  eigenstates can be written as linear combinations of the form  $|E_\alpha^0\rangle_f = \sum_{\sigma_0} |\sigma_0\rangle A_{1\alpha}^{[\sigma_0]}$ , where the coefficients have been arranged into  $d$  matrices  $A^{[\sigma_0]}$  of dimensions  $1 \times d$  (i.e.,  $d$ -dimensional vectors), with matrix elements  $A_{1\alpha}^{[\sigma_0]}$ . Then add to the chain the site  $n + 1$  and diagonalize  $\mathcal{H}_{n+1}$  in the enlarged Hilbert space spanned by the  $(D_n d)$  states  $|E_\alpha^n\rangle_f |\sigma_{n+1}\rangle$ . The new orthonormal set of eigenstates, with energies  $(E_\beta^{n+1})_f$ , can be written as linear combinations of the form

$$|E_\beta^{n+1}\rangle_f = \sum_{\sigma_{n+1}=1}^d \sum_{\alpha=1}^{D_n} |E_\alpha^n\rangle_f |\sigma_{n+1}\rangle A_{\alpha\beta}^{[\sigma_{n+1}]}, \quad (4.5)$$

with  $\beta = 1, \dots, (D_n d)$ . Here the coefficients specifying the linear combination have been arranged into a set of  $d$  matrices  $A^{[\sigma_{n+1}]}$  of dimension  $D_n \times D_{n+1}$ , with matrix elements  $A_{\alpha\beta}^{[\sigma_{n+1}]}$ . The orthonormality of the eigenstates at each stage of the iteration,  ${}_f\langle E_\beta^n | E_{\beta'}^n \rangle_f = \delta_{\beta\beta'}$ , implies that the  $A$ -matrices automatically satisfy the orthonormality condition

$$\sum_{\sigma_n} A^{[\sigma_n]\dagger} A^{[\sigma_n]} = \mathbb{1}. \quad (4.6)$$

We remark that it is possible to exploit symmetries of  $\mathcal{H}_n$  (e.g. under particle-hole transformation) to cast  $A$  in block-diagonal form to make the calculation more time- and memory-efficient. However, for the purposes of the present work, this was not required.

Iterating the above procedure by adding site after site and repeatedly using Eq. (4.5), we readily find that the NRG eigenstates of  $\mathcal{H}_N$  on the folded Wilson chain can be written in the form of a so-called *matrix-product state* [51],

$$|E_\beta^N\rangle_f = \sum_{\{\sigma^N\}} |\sigma^N\rangle (A^{[\sigma_0]} A^{[\sigma_1]} \dots A^{[\sigma_N]})_{1\beta}, \quad (4.7)$$

illustrated in Fig. 4.2(a). Here matrix multiplication is implied in the product

$$(A^{[\sigma_n]} A^{[\sigma_{n+1}]})_{\alpha\beta} = \sum_{\gamma} A_{\alpha\gamma}^{[\sigma_n]} A_{\gamma\beta}^{[\sigma_{n+1}]}, \quad (4.8)$$

and  $\{\sigma^N\}$  denotes the set of all sequences  $\sigma_0, \sigma_1, \dots, \sigma_N$ . This matrix multiplication generates entanglement between neighboring sites, with the capacity for entanglement increasing with the dimension  $D_n$  of the index being summed over.

### 4.3.2 NRG truncation

In practice, it is of course not possible to carry out the above iteration strategy explicitly for chains longer than a few sites, because the size of the  $A$ -matrices grows exponentially with

$N$ . Hence Wilson proposed the following NRG truncation procedure: Once  $D_n$  becomes larger than a specified value, say  $D$ , only the lowest  $D$  eigenstates  $|E_\alpha^n\rangle_f$ , with  $\alpha = 1, \dots, D$ , are retained or kept at each iteration, and all higher-lying ones discarded. It has recently been shown [69, 70] that the discarded states can be used to construct a complete basis of many-body states spanning the full  $d^{N+1}$ -dimensional Hilbert space of  $\mathcal{H}_N$ , and that this basis can be used to greatly improve the accuracy of the NRG-calculations of spectral functions [71, 72]. Explicitly, the upper limit for the sum over  $\alpha$  in Eq. (4.5) is redefined to be

$$D_n = \min(d^{n+1}, D). \quad (4.9)$$

As a result, the dimensions of the  $A^{[\sigma_n]}$  matrices occurring in the matrix-product state (4.7) start from  $1 \times d$  at  $n = 0$  and grow by a factor of  $d$  for each new site until they saturate at  $D \times D$  after truncation has set in. The structure of the resulting states  $|E_\beta^N\rangle_f$  is schematically depicted in Figs. 4.2(a) and 4.2(b), in which the site index is viewed as a single or composite index,  $\sigma_n$  or  $(\sigma_{n\downarrow}, \sigma_{n\uparrow})$ , respectively.

Wilson showed that this truncation procedure works well in practice, because the hopping parameters  $t_n$  of Eq. (4.3) decrease exponentially with  $n$ : the resulting separation of energy scales along the chain ensures that high-lying eigenstates from iteration  $n$  make only a small contribution to the low-lying eigenstates of iteration  $n + 1$ , so that discarding the former hardly affects the latter. The output of the NRG algorithm is a set of eigenstates  $|E_\beta^n\rangle_f$  and eigenenergies  $(E_\beta^n)_f$  for each iteration, describing the physics at energy scale  $\Lambda^{-n/2}$ . The NRG eigenenergies are usually plotted in rescaled form,

$$(\varepsilon_\beta^n)_f = (E_\beta^n - E_1^n)_f / \Lambda^{-n/2}, \quad (4.10)$$

as functions of  $n$ , to obtain a so-called NRG flow diagram; it converges to a set of fixed-point values as  $n \rightarrow \infty$ . Figure 4.7 in Section 4.5.2 below shows some examples. The ground state energy of the entire chain is given by the lowest energy of the last iteration,  $(E_G^N)_f = (E_1^N)_f$ .

Despite the great success of NRG, Wilsonian truncation does have some drawbacks. Firstly, its errors grow systematically as  $\Lambda$  tends to 1, because then the separation of energy scales on which it relies becomes less efficient. Secondly, it is not variational, and hence it is not guaranteed to produce the best possible approximation for the ground state within the space of all matrix-product states of similar form and size. We shall return to this point later in Section 4.6 and study quantitatively to what extent the NRG ground state wavefunction can be improved upon by further variational optimization.

### 4.3.3 Mutual information of opposite spins on site $n$

A crucial feature of the folded Wilson chain is that all degrees of freedom associated with the same energy scale,  $\Lambda^{-n/2}$ , are represented by one and the same site and hence are all added during the same iteration step. Since the spin-down and -up degrees of freedom associated

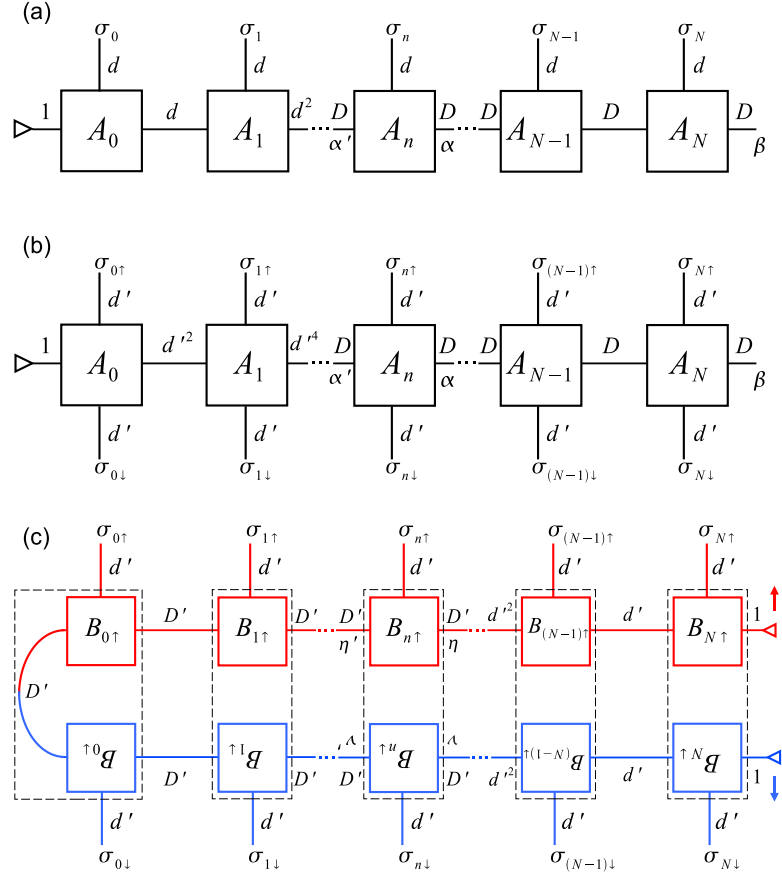


**Figure 4.2:** (a) and (b) show the matrix-product structure of the state  $|E_\beta^N\rangle_f$  of Eq. (4.7), depicting the site index as a single or composite index,  $\sigma_n$  or  $(\sigma_{n\downarrow}, \sigma_{n\uparrow})$ , respectively. (c) shows the matrix-product structure of the state  $|\Psi^N\rangle_u$  of Eq. (4.16). (For the sake of illustrating Eq. (B.5) of Appendix B, the labels  $(B_{n\downarrow})_{\nu\nu'}$  in the bottom row are purposefully typeset “upside down”, so that they would be right-side up if the chain of boxes were all drawn in one row in the order indicated by Eq. (4.16). Thus, the latter contains the factors  $\dots(B_{n\downarrow})_{\nu\nu'} \dots (B_{n\uparrow})_{\eta'\eta} \dots$ , in that order, compare Eq. (B.5).) Each matrix  $A$  or  $B$  is represented by a box, summed-over indices by links, free indices by terminals, and dummy indices having just a single value, namely 1, by ending in a triangle. The dimensions ( $d$ ,  $D$ ,  $d'$ ,  $D'$ , etc.) next to each link or terminal give the number of possible values taken on by the corresponding index, assuming Wilsonian truncation for (a) and (b), and VMPS truncation for (c). Note the similarity in structure between (c) and (b): the dashed boxes in the former, containing  $B_{\nu\nu'}^{[\sigma_{n\downarrow}]} \otimes B_{\eta'\eta}^{[\sigma_{n\uparrow}]}$ , play the role of the  $A_{\alpha'\alpha}^{[(\sigma_{n\downarrow}, \sigma_{n\uparrow})]}$  matrices in the latter. Their capacity for entangling neighboring sites is comparable if one chooses  $D'^2 \propto D$  [cf. Eq. (4.24)], since neighboring dashed boxes in (c) are connected by two links of combined dimension  $D'^2$ , whereas neighboring  $A$ -matrices in (b) are connected by only a single link of dimension  $D$ .

with each site are thus treated on an equal footing, the resulting matrix-product state provides comparable amounts of resources for encoding entanglement between local states of the same spin, involving  $|\sigma_{n\mu}\rangle|\sigma_{n+1\mu}\rangle$ , or between states of opposite spin (indicated by the bar), involving  $|\sigma_{n\mu}\rangle|\sigma_{n\bar{\mu}}\rangle$  or  $|\sigma_{n\mu}\rangle|\sigma_{n+1\bar{\mu}}\rangle$ . However, it turns out that for the Anderson model this feature, though *a priori* attractive, is in fact an unnecessary (and memory-costly) luxury: Since the Anderson model Hamiltonian (4.2) couples spin-down and -up electrons only at the impurity site, the amount of entanglement between states of opposite spin rapidly decreases with  $n$ .

To illustrate and quantify this claim, it is instructive to calculate the so-called mutual information  $M_n^{\downarrow\uparrow}$  of the spin-down and -up degrees of freedom of a given site  $n$ . This quantity is defined via the following general construction [57]. Let  $C$  denote an arbitrary set of degrees of freedom of the Wilson chain, represented by the states  $|\sigma^C\rangle$ . Let  $\rho^C$  be the reduced density matrix obtained from the ground state density matrix by tracing out all degrees of freedom except those of  $C$ , denoted by  $N\setminus C$ :

$$\rho^C = \sum_{\{\sigma^{N\setminus C}\}} \langle \sigma^{N\setminus C} | E_G^N \rangle_{\text{ff}} \langle E_G^N | \sigma^{N\setminus C} \rangle . \quad (4.11)$$

For example, if  $C$  represents the spin-down and up-degrees of freedom of site  $n$ , its matrix elements are:

$$\rho_{\sigma_n \sigma'_n}^C = \sum_{\{\sigma^{N\setminus n}\}} (A^{[\sigma_N]\dagger} \dots A^{[\sigma_n]\dagger} \dots A^{[\sigma_0]\dagger})_{G1} \times (A^{[\sigma_0]} \dots A^{[\sigma'_n]} \dots A^{[\sigma_N]})_{1G} . \quad (4.12)$$

If  $C$  represents only the spin- $\mu$  degree of freedom of site  $n$ , a similar expression holds, with  $n$  replaced by  $n\mu$ . The entropy associated with such a density matrix is given by

$$S^C = - \sum_i w_i^C \ln w_i^C , \quad (4.13)$$

where  $w_i^C$  are the eigenvalues of  $\rho^C$ , with  $\sum_i w_i^C = 1$ . Now, consider the case that  $C = AB$  is a combination of the degrees of freedom of two distinct subsets  $A$  and  $B$ , represented by states of the form  $|\sigma^C\rangle = |\sigma^A\rangle|\sigma^B\rangle$ . Then the mutual information of  $A$  and  $B$ , defined by

$$M^{AB} = S^A + S^B - S^{AB} , \quad (4.14)$$

characterizes the information contained in  $\rho^{AB}$  beyond that contained in  $\rho^A \otimes \rho^B$ . The mutual information  $M^{AB} = 0$  if there is no entanglement between the degrees of freedom of  $A$  and  $B$ , since then  $\rho^{AB} = \rho^A \otimes \rho^B$  and its eigenvalues have a product structure,  $w_{ij}^{AB} = w_i^A w_j^B$ .

We define the mutual information between spin-down and -up degrees of freedom of site  $n$  of the folded chain,  $M_n^{\downarrow\uparrow}$ , by Eq. (4.14), taking  $A = n\downarrow$  and  $B = n\uparrow$ . Figure 4.3 shows this quantity as function of  $n$  for the symmetric Anderson model. Evidently  $M_n^{\downarrow\uparrow}$  is

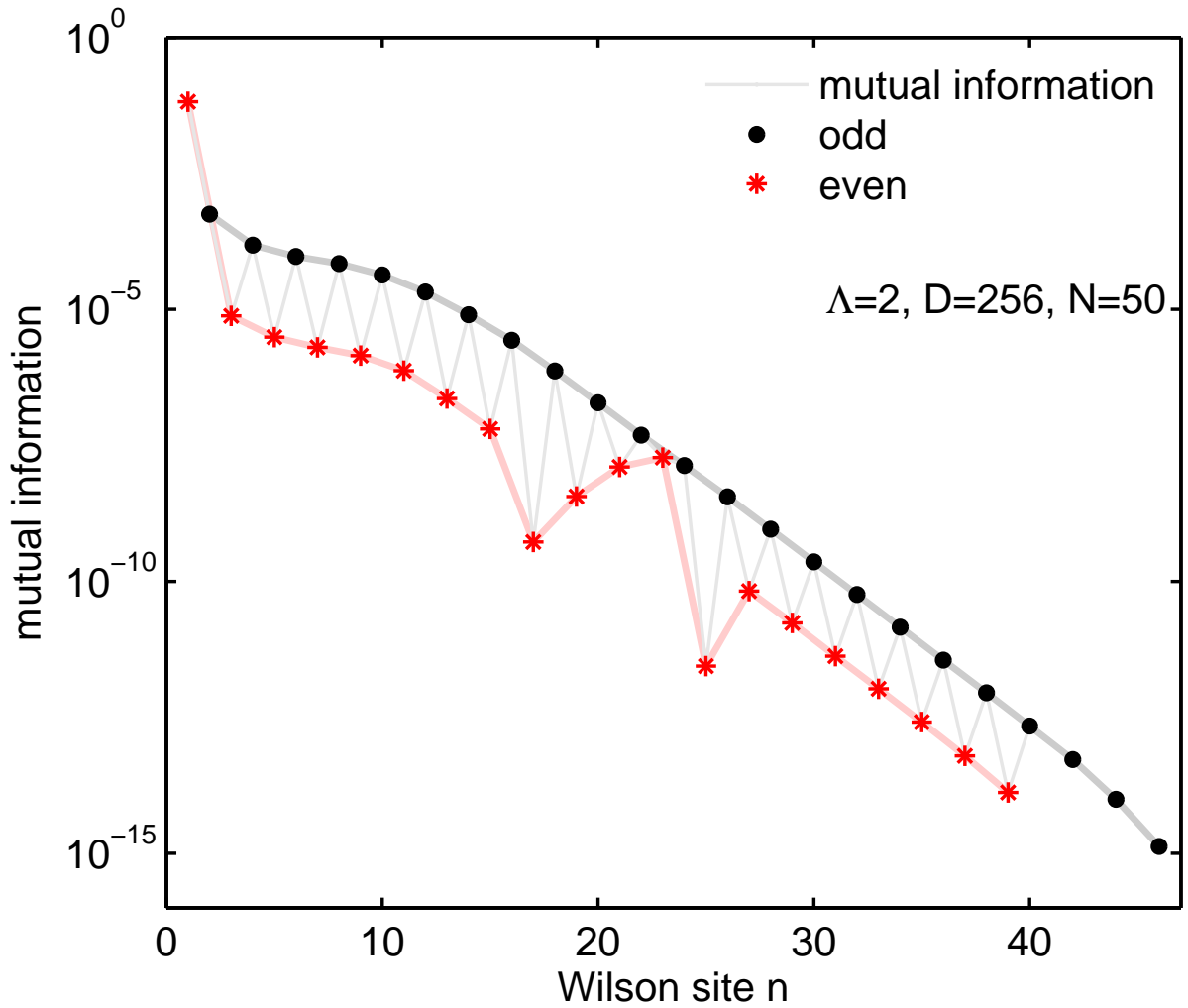


**Figure 4.3:** NRG result for the mutual information  $M_n^{\downarrow\uparrow}$  between spin-down and -up degrees of freedom of site  $n$  of a folded Wilson chain of length  $N = 50$ . The Anderson model parameters are fixed at  $U = \frac{1}{2}$ ,  $U/\pi\Gamma = 1.013$ ,  $\epsilon_d = -\frac{1}{2}U$  throughout this chapter. Lines connecting data points are guides for the eye. The slight differences in behavior observed for even or odd  $n$  are reminiscent of the well-known fact [2] that the ground state degeneracy of a Wilson chain is different for even or odd  $N$ .

very small for all but the first few sites, and decreases exponentially with  $n$ . This implies that for most of the folded chain, there is practically no entanglement between the spin-down and -up degrees of freedom. Consequently, the corresponding matrices occurring in Eq. (4.7) for  $|E_G^N\rangle_f$  in effect have a direct product structure: loosely speaking, we may write  $A^{[\sigma_n]} \simeq B^{[\sigma_{n\downarrow}]} \otimes B^{[\sigma_{n\uparrow}]}$ . In the next subsection, we will exploit this fact to achieve a significant reduction in memory cost, by implementing the effective factorization in an alternative matrix-product ansatz [see Eq. (4.16) below], defined on an *unfolded* Wilson chain which represents  $n\downarrow$  and  $n\uparrow$  of freedom by two separate sites.

## 4.4 DMRG treatment of unfolded Wilson chain

### 4.4.1 Variational matrix-product state ansatz

As pointed out by Verstraete *et al.* [51], an alternative approach for finding a numerical approximation for the ground state can be obtained by *variationally minimizing* the ground state energy in the space of all “variational matrix-product states” (VMPS) of fixed norm. Implementing the latter constraint via a Lagrange multiplier  $\lambda$ , one thus considers the following minimization problem,

$$\min_{|\Psi\rangle \in \{|\Psi^N\rangle_{\text{u}}\}} [\langle \Psi | \mathcal{H}_N | \Psi \rangle - \lambda (\langle \Psi | \Psi \rangle - 1)] . \quad (4.15)$$

The minimization is to be performed over the space of all variational matrix-product states  $|\Psi^N\rangle_{\text{u}}$  having a specified structure (see below), with specified dimensions  $D'_n$  for the matrices, whose matrix elements are now treated as variational parameters. This minimization can be performed by a “sweeping procedure”, which optimizes one matrix at a time while keeping all others fixed, then optimizing the neighboring matrix, and so forth, until convergence is achieved. The resulting algorithm is equivalent to a single-site DMRG treatment of the Wilson chain. Our main goal is to analyze how the energies and eigenstates so obtained compare to those produced by NRG.

Having decided to use a variational approach, it becomes possible to explore matrix-product states having different, possibly more memory-efficient structures than those of Eq. (4.7) and Fig. 4.2(a). In particular, we can exploit [77] the fact that the Anderson model Hamiltonian (4.2) couples spin-down and -up electrons only at the impurity site, as emphasized in Eq. (4.2) and Fig. 4.1(b). For such a geometry, it is natural to consider matrix-product states defined on the *unfolded* Wilson chain (subscript u) and having the following form, depicted schematically in Fig. 4.2(c):

$$|\Psi^N\rangle_{\text{u}} = \sum_{\{\sigma^N\}} |\sigma^N\rangle (B^{[\sigma_{N\downarrow}]} \dots B^{[\sigma_{0\downarrow}]} B^{[\sigma_{0\uparrow}]} \dots B^{[\sigma_{N\uparrow}]})_{11}. \quad (4.16)$$

The order in which the  $B^{[\sigma_{n\mu}]}$  matrices occur in the product mimics the order in which the sites are connected in the unfolded Wilson chain. (The fact that this order differs from the order in which the basis states  $|\sigma_{n\mu}\rangle$  for each site are arranged in the many-body basis state  $|\sigma^N\rangle$ , see Eq. (4.4b), does not cause minus signs complications, because we work with Jordan-Wigner-transformed effective spin chains.) Each  $B^{[\sigma_{n\mu}]}$  stands for a set of  $d' = 2$  matrices with matrix elements  $B_{\nu\eta}^{[\sigma_{n\mu}]}$ , with dimensions  $D'_n \times D'_{n-1}$  for  $B^{[\sigma_{n\downarrow}]}$  and  $D'_{n-1} \times D'_n$  for  $B^{[\sigma_{n\uparrow}]}$ , where

$$D'_n = \min(d'^{N-n}, D'), \quad (4.17)$$

as indicated on the links connecting the squares in Fig. 4.2(c). This choice of matrix dimension allows the outermost few sites at both ends of the unfolded chain to be described



exactly (similarly to the first few sites of the folded Wilson chain for NRG), while introducing truncation, governed by  $D'$ , for the matrices in the central part of the chain. The first index on  $B_{1\nu}^{[\sigma_{N1}]}$  and the second index on  $B_{\nu 1}^{[\sigma_{N1}]}$  are dummy indices taking on just a single value, namely 1, since they represent the ends of the chain. The triangles in Fig. 4.2(c) are meant to represent this fact. As a result, Eq. (4.16) represents just a single state, namely the ground state, in contrast to Eq. (4.7), which represents a set of states, labeled by the index  $\beta$ . Moving inward from the endpoints by decreasing  $n$ , the matrix dimension parameter  $D'_n$  increases by one factor of  $d'$  for each site, in such a way that the resulting matrices are of just the right size to describe the outside ends of the chain (from  $n$  to  $N$ ) *exactly*, i.e. without truncation. After a few sites, however, truncation sets in and the matrix dimensions saturate at  $D' \times D'$  for the central part of the chain.

To initialize the variational search for optimal  $B$ -matrices, it turns out to be sufficient to start with a set of random matrices with normally distributed random matrix elements. Next, singular value decomposition is used to orthonormalize the  $B$ -matrices in such a way [see Eq. (A.1)] that the matrix-product state Eq. (4.16) has norm 1 (see App. A for details). Thereafter, variational optimization sweeps are performed to minimize Eq. (4.15) one  $B$ -matrix at a time [51]. The technical details of this procedure will be published separately. After a sweeping back and forth through the entire chain a few times, the variational state typically converges (as illustrated by Fig. 4.13 in Sec. 4.6.2 below), provided that  $D'$  is sufficiently large. We shall denote the resulting converged variational ground state by  $|E_G^N\rangle_u$ . Its variational energy,  $(E_G^N)_u$ , turns out to be essentially independent of the random choice of initial matrices.

#### 4.4.2 VMPS truncation

Since  $D' \times D'$  is the maximal dimension of  $B$ -matrices,  $D'$  is the truncation parameter determining the effective size of the variational space to be searched and hence the accuracy of the results. Its role can be understood more explicitly using a technique that is exceedingly useful in the VMPS approach, namely singular value decomposition: any rectangular matrix  $\mathcal{B}$  of dimension  $m \times m'$  can be written as

$$\mathcal{B} = \mathcal{U}\mathcal{S}\mathcal{V}^\dagger, \quad \text{with} \quad \mathcal{U}^\dagger\mathcal{U} = \mathcal{V}^\dagger\mathcal{V} = \mathbb{1}, \quad (4.18)$$

where  $\mathcal{S}$  is a diagonal matrix of dimension  $\min(m, m')$ , whose diagonal elements, the so-called ‘‘singular values’’, can always be chosen to be real and non-negative, and  $\mathcal{U}$  and  $\mathcal{V}^\dagger$  are column- and row-unitary matrices (with dimensions  $m \times \min(m, m')$  and  $\min(m, m') \times m'$ , respectively). Due to the latter fact, the matrix norm of  $\mathcal{B}$  is governed by the magnitude of the singular values.

For any given site of the unfolded Wilson chain, this decomposition can be applied in one of two ways (depending on the context, see App. A) to the set of matrices with elements  $B_{\nu\eta}^{[\sigma_{n\mu}]}$ : introduce a composite index  $\bar{\nu} = (\sigma_{n\mu}, \nu)$  (or  $\bar{\eta} = (\sigma_{n\mu}, \eta)$ ) to arrange their matrix elements into a rectangular matrix carrying only two labels, with matrix elements  $\mathcal{B}_{\bar{\nu}\bar{\eta}} = B_{\nu\eta}^{[\sigma_{n\mu}]}$  (or  $\tilde{\mathcal{B}}_{\bar{\nu}\bar{\eta}} = B_{\nu\eta}^{[\sigma_{n\mu}]}$ ), and decompose this new matrix as  $\mathcal{B} = \mathcal{U}\mathcal{S}\mathcal{V}^\dagger$ .

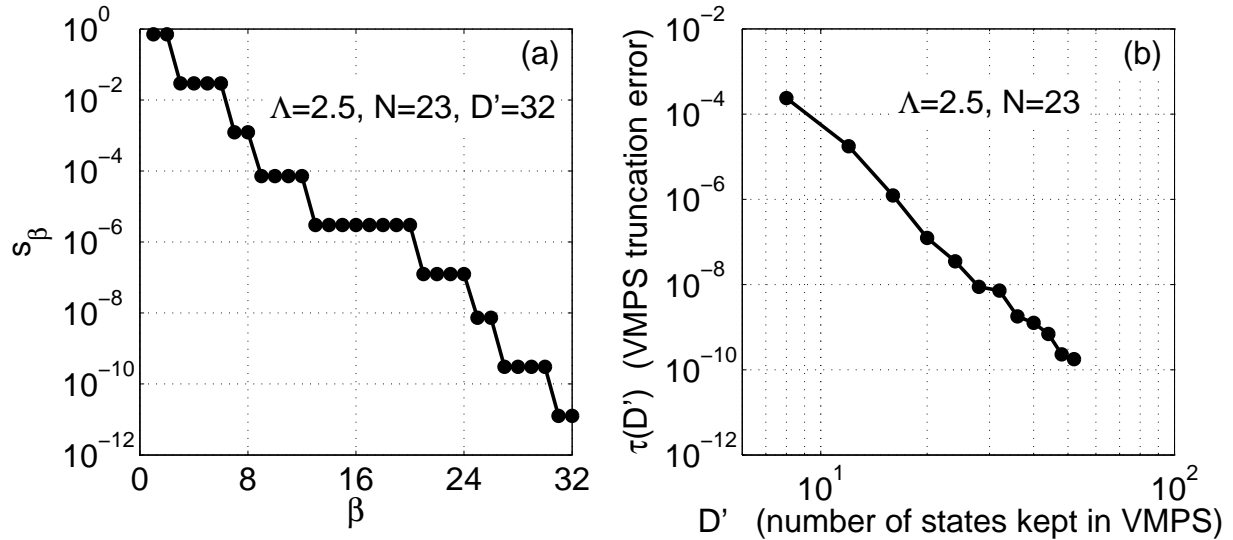


**Figure 4.4:** (a) Typical singular value spectrum for site  $5\downarrow$  of the unfolded Wilson chain, obtained by singular value decomposition of  $B^{[\sigma_{5\downarrow}]}$ . It shows, roughly, power-law decrease for large enough  $\beta$ , modulo steps due to degeneracies in the singular value spectrum. (b)  $D'$ -dependence of the truncation error  $\tau(D')$  [Eq. (4.19)].

Now, if this is done for any site for which the set of matrices  $B^{[\sigma_{n\mu}]}$  have maximal dimensions  $D' \times D'$ , the corresponding matrix  $\mathcal{S}$  will likewise have dimensions  $D' \times D'$ . Let its diagonal elements, the singular values  $s_\nu$  (with  $\nu = 1, \dots, D'$ ), be labelled in order of decreasing size. (Their squares,  $s_\nu^2$ , correspond to the eigenvalues of the density matrix constructed in the course of the single-site DMRG algorithm [6].) If  $D'$  is sufficiently large, the  $s_\nu$  are typically found to decrease with increasing  $\nu$  roughly as some negative power of  $\nu$ , as illustrated in Fig. 4.4(a). The last and smallest of the singular values,  $s_{D'}^2$  (squared, following Ref. [6]), thus indicates the weight of the information that is lost at that site due to the given (finite) choice of  $D'$ : by choosing  $D'$  larger, less information would be lost since more singular values (though of smaller size) would be retained. Repeating such an analysis for all sites of the unfolded Wilson chain, one may define the largest of the  $s_{D'}^2$  parameters of the entire chain,

$$\tau(D') = \max_{\{n\mu\}}(s_{D'}^2), \quad (4.19)$$

as “truncation error” characterizing the maximal information loss for a given value of  $D'$ . Typically,  $\tau(D')$  decreases as some negative power of  $D'$ , as illustrated in Fig. 4.4(b). In this way,  $D'$  assumes the role of a cutoff parameter that directly governs the accuracy of the VMPS approach, in a way analogous to the parameter  $D$  of NRG.

### 4.4.3 Refolding

The VMPS approach purposefully focusses on finding an optimal description of the variational *ground* state  $|E_G^N\rangle_u$ . Nevertheless, the  $B$ -matrices from which the latter is constructed contain information about all energy scales of the model, due to the logarithmic discretization of the Wilson chain. In particular, information about the scale  $\Lambda^{-n/2}$  is encoded in the set of matrices  $B^{[\sigma_{n\mu}]}$  associated with the two site  $n\downarrow$  and  $n\uparrow$ . From these, it is possible to extract excited-state eigenspectra and energy flow diagrams in complete analogy to those produced by NRG. In this subsection we explain how this can be accomplished by a technique to be called “refolding”, which combines the two matrices  $B^{[\sigma_{n\downarrow}]}$  and  $B^{[\sigma_{n\uparrow}]}$  into a single matrix, say  $B^{[\sigma_n]}$ , and thereby recasts unfolded matrix-product states into folded ones. It should be emphasized that this procedure simply amounts to an internal reorganization of the representation of the VMPS ground state.

Consider a given matrix-product state  $|\Psi^N\rangle_u$  of the form (4.16), defined on an unfolded Wilson chain of length  $N$  (e.g. the converged ground state  $|E_G^N\rangle_u$ ). To *refold* it (subscript  $r$ ), it is expressed as a state of the following form [same as Eq. (4.7)]

$$|\Psi^N\rangle_r = \sum_{\{\sigma^N\}} |\sigma^N\rangle (B^{[\sigma_0]} B^{[\sigma_1]} \dots B^{[\sigma_N]})_{11}, \quad (4.20)$$

defined on a folded Wilson chain of length  $N$  and normalized to unity,  ${}_r\langle\Psi^N|\Psi^N\rangle_r = 1$ . Graphically speaking, this corresponds to rewriting a state of the form shown in Fig. 4.2(c) in terms of states of the form of Fig. 4.2(a). To obtain the matrices needed for Eq. (4.20), one constructs, for every site  $n$  of the refolded chain, a set of  $d$  matrices  $B^{[\sigma_n]}$  from a combination of the two sets of spin-resolved matrices  $B^{[\sigma_{n\downarrow}]}$  and  $B^{[\sigma_{n\uparrow}]}$  of the unfolded chain (App. B gives the details of this construction). This is done in such a way, using singular value decomposition, that (i) the resulting matrices  $B^{[\sigma_n]}$  satisfy the orthonormality conditions (4.6) (with  $A \rightarrow B$ ), thereby guaranteeing the unit normalization of the the refolded state  $|\Psi^N\rangle_r$ ; and (ii) the  $B^{[\sigma_n]}$  matrices have a structure similar to that of the matrices  $A^{[\sigma_n]}$  generated by NRG, except that their dimensions,  $D_n^r \times D_{n+1}^r$ , are governed by

$$D_n^r = \min(d^n, d^{N+1-n}, D^2) \quad (4.21)$$

[instead of Eq. (4.9)], for reasons explained in App. B. Thus, their dimensions have the maximal value  $D^r \times D^r$ , with  $D^r = D^2$ , in the central part of the refolded chain, while decreasing at its ends towards  $1 \times d$  or  $d \times 1$  for  $n = 0$  or  $N$ , respectively.

Now, suppose that a converged variational ground state  $|E_G^N\rangle_u$  has been obtained and refolded into the form  $|\Psi^N\rangle_r$ , so that the corresponding orthonormalized matrices  $B^{[\sigma_n]}$  for the refolded Wilson chain of length  $N$  are the building blocks of the ground state of the system. Then it is possible to extract from them information about the many-body excitation spectrum at energy scale  $\Lambda^{-n/2}$  that is analogous to the information produced by NRG. To this end, consider a *subchain* of length  $n$  of the full refolded Wilson chain, and use the definition

$$|\Psi_\beta^n\rangle_r = \sum_{\{\sigma^n\}} |\sigma^n\rangle (B^{[\sigma_0]} B^{[\sigma_1]} \dots B^{[\sigma_n]})_{1\beta}, \quad (4.22)$$

[as in Eq. (4.20), but with  $N$  replaced by  $n$ ] to construct a set of states  $|\Psi_\beta^n\rangle_r$  on this subchain. These states, shown schematically by sites 0 to  $n$  of Fig. 4.2(a), form an orthonormal set,  ${}_r\langle\Psi_\alpha^n|\Psi_\beta^n\rangle_r = \delta_{\alpha\beta}$ , due to the orthonormality [Eq. (4.6)] of their constituent matrices. They can thus be viewed as a basis for that *subspace* of the many-body Hilbert space for the length- $n$  Wilson chain, i.e. of that subspace of  $\text{span}\{|\sigma^n\rangle\}$ , which VMPS sweeping has singled out to be most relevant for describing the ground state  $|E_G^N\rangle_u$  of the full chain of length  $N$ . Therefore we shall henceforth call the  $|\Psi_\beta^n\rangle_r$  “(refolded) VMPS basis states” for this subchain.

This basis can be used to define an effective “refolded Hamiltonian”  $\mathcal{H}_r^n$  for this subchain, with matrix elements

$$(\mathcal{H}_r^n)_{\alpha\beta} = {}_r\langle\Psi_\alpha^n|\mathcal{H}_n|\Psi_\beta^n\rangle_r. \quad (4.23)$$

Appendix C gives the details of how  $(\mathcal{H}_r^n)_{\alpha\beta}$  can be calculated efficiently in the MPS basis in a recursive manner. Its eigenvalues and eigenstates, say  $(E_\beta^n)_r$  and  $|E_\beta^n\rangle_r$ , are the VMPS analogues of the NRG eigenvalues and eigenstates,  $(E_\beta^n)_f$  and  $|E_\beta^n\rangle_f$ , respectively. They differ, in general, because VMPS and NRG use different truncation criteria, but are expected to agree well for sufficiently large choices of  $D'$  and  $D$ . This is indeed found to be the case, as will be shown in detail in the next section.

## 4.5 Comparison of NRG and VMPS results

Having outlined the NRG and VMPS strategies in the previous section, we now turn to a comparison of their results. This will be done, in successive subsections, by comparing their ground state energies and the overlaps of the corresponding ground states; the eigenspectra and density of states obtained from both approaches; and finally, the energy eigenstates used in the two approaches. We will thereby gain more insights into the differences between NRG and VMPS truncation criteria. Before embarking on a detailed comparison, though, some remarks on the choices to be made for  $D$  and  $D'$  are in order.

Since the structure of the matrix products occurring in Eqs. (4.7) and (4.16) differ, the spaces consisting of all states of the type  $|E_\beta^n\rangle_f$  or  $|E_\beta^n\rangle_r$ , to be called the “NRG-subspace” or “VMPS-subspace” for a length- $n$  chain, respectively, constitute nonidentical subspaces of the  $d^{n+1}$ -dimensional Hilbert space spanned by the basis states  $|\sigma^n\rangle$ . The extent to which they describe the energy eigenstates of  $\mathcal{H}_N$  with comparable accuracy will depend very strongly on the choices made for  $D$  and  $D'$ . It turns out (numerical evidence will be presented below) that with the choice

$$D' = d^m \sqrt{D}, \quad (4.24)$$

the VMPS-subspace is sufficiently large to give highly accurate representations of all kept states of NRG (including, in particular, the ground state) for the choice  $m = 1$ , or of all kept *and* discarded states of NRG for the choice  $m = 2$ . The fact that  $D'$  should be proportional to  $\sqrt{D}$  can be made plausible by considering the following question: given

a folded Wilson subchain of length  $n$  (i.e. consisting of sites 0 to  $n$ ) and its equivalent unfolded version, what are the smallest values for the dimensions  $D$  and  $D'$  for which both approaches describe the ground state *exactly*, i.e. without any truncation? Answer: On the one hand, the folded subchain has  $n + 1$  sites of dimension  $d$ , and hence a total dimension  $d^{n+1}$ ; to ensure that the ground state in this space is described exactly, the kept space of the previous iteration must not involve any truncation, implying  $D = d^n$ . On the other hand, for the equivalent unfolded subchain, the spin  $\downarrow$  and  $\uparrow$  parts each have  $n + 1$  sites of dimension  $d'$ , hence each have a Hilbert space of total dimension  $d'^{(n+1)}$ ; to ensure that this space is described without truncation, its dimension should equal the maximal dimension of the  $B$ -matrices at sites  $0\mu$ , implying  $D' = d'^{n+1}$ . Using  $d' = \sqrt{d}$  we readily find  $D' = d'\sqrt{D}$ , establishing the proportionality between  $D'$  and  $\sqrt{D}$  and suggesting the choice  $m = 1$  to achieve an accurate VMPS-representation of the ground state. Actually, we find numerically that already  $m = 0$  yields good qualitative agreement between the VMPS and NRG ground states, while  $m = 1$  yields a *quantitatively* accurate VMPS-representation of the NRG ground state also for larger chain lengths, that do involve truncation. Since such ground states are built from the kept spaces of previous iterations, this implies that for  $m = 1$ , all *kept* states in NRG (not only the ground state) are likewise well represented by VMPS. Indeed, we will find this to be the case. Moreover, it turns out numerically that with  $m = 2$ , it is also possible to achieve an accurate VMPS-representation of all kept *and* discarded NRG-type states, as will be extensively illustrated below.

For the results reported below, we show data only for even iteration number  $n$ , to avoid even/odd oscillation effects that are typical and well-understood for Wilsonian logarithmic discretization, but not of particular interest here. We set  $D' = d^m \sqrt{D}$  throughout and specify the choices made for  $m$ . All VMPS results shown in this section are extracted from randomly initialized, fully converged variational ground states  $|E_G^N\rangle_u$  of the form (4.16).

### 4.5.1 Ground state energies and overlaps

Figures 4.5(a) and 4.5(b) compare the NRG and VMPS *ground state energies*,  $(E_G^N)_f$  and  $(E_G^N)_u$ , for three values of  $\Lambda$  and, in (a), two values of  $m$ . They illustrate three points. Firstly, for a given  $\Lambda$  the VMPS ground state energies are smaller than those of NRG,  $(E_G^N)_u < (E_G^N)_f$ , as expected, since VMPS is a variational method and NRG is not. Secondly, Fig. 4.5(a) shows that larger values of  $m$  yield lower VMPS ground state energies, as expected, since their variational space is larger. Thirdly, the improvement of VMPS over NRG, as measured by the energy difference  $(E_G^N)_f - (E_G^N)_u$  shown in Fig. 4.5(b), becomes more significant for smaller  $\Lambda$ , as expected, since the truncation scheme of NRG relies heavily on energy scale separation, and hence becomes less efficient for smaller  $\Lambda$ .

Figure 4.5(c) compares the overlap between NRG and VMPS ground states, characterized by the deviation from 1 of the overlap  $|\langle E_G^N|E_G^N\rangle_u|$ . The latter can be calculated

straightforwardly from

$$\begin{aligned} {}_f\langle E_G^N | E_G^N \rangle_u &= \sum_{\{\sigma^N\}} (A^{[\sigma_N]^\dagger} \dots A^{[\sigma_0]^\dagger})_{G1} \\ &\quad \times (B^{[\sigma_{N1}]} \dots B^{[\sigma_{01}]} B^{[\sigma_{0\dagger}]} \dots B^{[\sigma_{N\dagger}]})_{11} \end{aligned} \quad (4.25)$$

where the index contractions associated with the summation over repeated indices are illustrated in Fig. 4.6(a). Fig. 4.5(c) shows that the deviation of the overlap from 1 becomes larger the smaller  $\Lambda$ , again illustrating that then the NRG truncation scheme becomes less reliable.

### 4.5.2 Comparison of eigenspectra and density of states

Figure 4.7 compares the energy *flow diagrams* obtained from NRG and refolded VMPS data, the latter obtained by diagonalizing the effective Hamiltonian of Eq. (4.23). It shows the rescaled energies  $(\varepsilon_\beta^n)_{f,r}$  of Eq. (4.10) as functions of  $n$ , for four combinations of  $m$  and  $\Lambda$ , and illustrates the same trends as found in the previous subsection: Firstly, the NRG and VMPS flow diagrams clearly agree not only for the ground state but also for a significant number of excited states. Evidently, the variational space searched by VMPS is large enough to capture considerable information about excited states, too, although the VMPS method was designed to optimize only the ground state. Moreover, for a given choice of  $\Lambda$ , NRG and VMPS eigenenergies coincide for a larger number of states for  $m = 2$  than for  $m = 0$  [compare (b) to (a) and (d) to (c)], because the variational space is larger. Secondly, for a given choice of  $m$ , NRG and VMPS eigenenergies agree better for  $\Lambda = 2.5$  than for  $\Lambda = 1.5$  [compare (c) to (a) and (d) to (b)], as expected, because larger  $\Lambda$  leads to better energy scale separation and reduces the inaccuracies inherent in NRG's Wilsonian truncation scheme.

As a complementary way of analyzing spectral information we also consider the “density of states”, for a given iteration number  $n$ ,

$$\rho_n(\varepsilon) = \sum_{\alpha=1}^{D_{\max}} \delta_\sigma(\varepsilon - \varepsilon_\alpha^n), \quad (4.26)$$

using the rescaled eigenenergies  $\varepsilon_\beta^n$  of Eq. (4.10). Here  $\delta_\sigma(\varepsilon) = e^{-\varepsilon^2/\sigma^2}/(\sigma\sqrt{\pi})$  is a Gaussian peak of width  $\sigma$  and unit weight, used to broaden the discrete spectrum in order to be able to plot it, and the number of states included in the sum is taken as  $D_{\max} = dD$  or  $d^m D$  for NRG or VMPS results, respectively. Figure 4.8 shows such a density of states for several choices of  $m$  and iteration number  $n$ . It illustrates three points:

Firstly, although for small energies  $\rho_n(\varepsilon)$  grows rapidly with  $\varepsilon$ , as expected for a many-body density of states, it does not continue to do so for larger  $\varepsilon$  (the exact density of states would), due to the truncation inherent in both NRG and VMPS strategies. For NRG,  $\rho_n(\varepsilon)$  drops to 0 very abruptly, because by construction Wilsonian truncation is sharp in

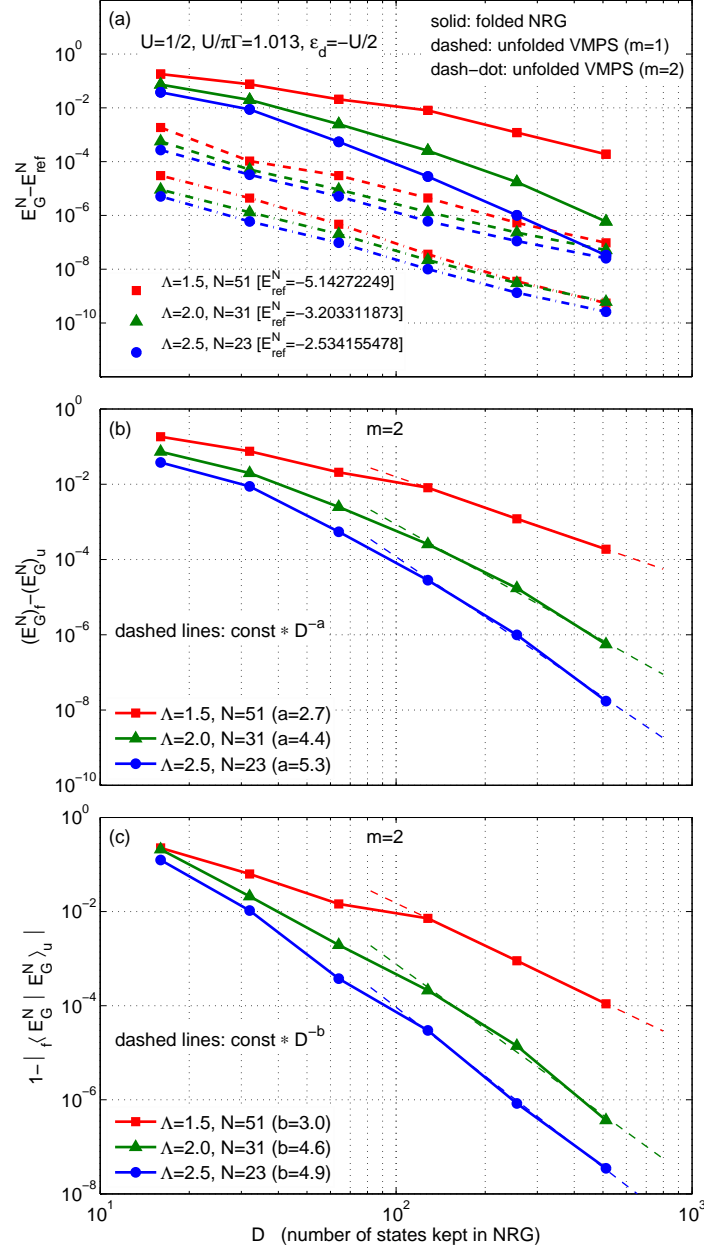


**Figure 4.5:** Comparison of NRG and VMPS results for (a,b) the ground state energies and (c) the ground state overlaps, plotted as a functions of  $D$  with  $D' = d^m \sqrt{D}$ , for three values of  $\Lambda$  and, in (a), for two values of  $m$ . In (a) the reference energies  $E_{\text{ref}}^N$  for each  $\Lambda$  were obtained by extrapolating the VMPS data points for  $m = 2$  to  $D' \rightarrow \infty$ , which represents the best estimate of the true ground state energy available within the present set of methods. The power law fits to the numerical data in (b) and (c), shown as dashed lines, were made for the three data points with largest  $D$ , for which the dimensions are large enough to have reliable NRG data.

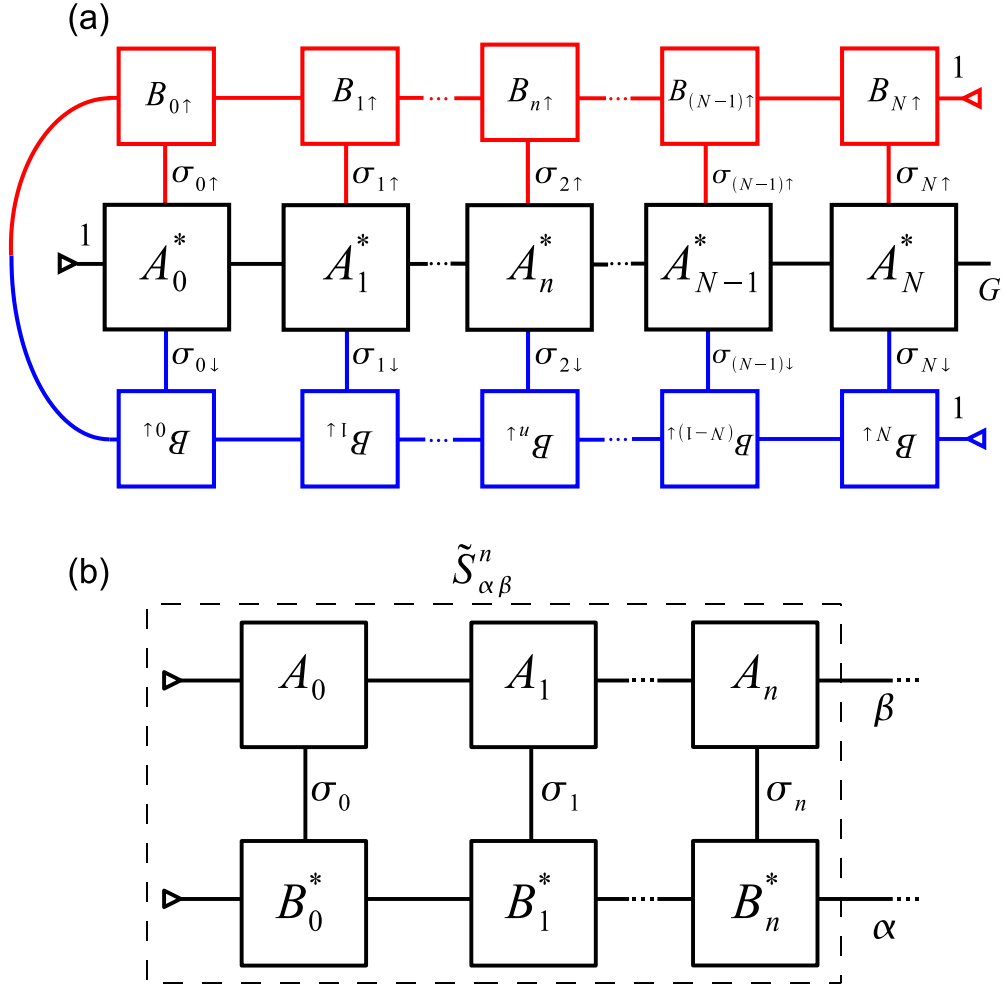


**Figure 4.6:** Contraction patterns used to calculate (a) the overlap  ${}_f\langle E_G^N | E_G^N \rangle_u$  [Eq. (4.25)] between folded NRG and unfolded VMPS ground states, and (b) the overlap matrix  $\tilde{S}_{\alpha\beta}^n = {}_r\langle \Psi_\alpha^n | E_\beta^n \rangle_f$  [Eq. (4.28b)] between refolded VMPS basis states and folded NRG eigenstates. Boxes represent  $A$  or  $B$  matrices in the graphical representation of Figs. 4.2(a) and 4.2(c), respectively (including the labelling conventions used there), and links connecting them represent indices that are being summed over.

energy space (at each iteration only the lowest  $dD$  eigenstates are calculated). In contrast, for VMPS  $\rho_n(\varepsilon)$  decreases more gradually for large  $\varepsilon$ , because VMPS truncation for states at site  $n$  is based not on their energy, but on the variationally determined weight of their contribution to the ground state of the full Wilson chain of length  $N$ . Evidently, these weights decrease with increasing  $\varepsilon$  less rapidly than assumed by NRG.

Secondly, the agreement of the VMPS curve for  $\rho_n(\varepsilon)$  with that of NRG is rather poor for  $m = 0$  (disagreement sets in already within the range of kept states of NRG, indicated by the shaded region), better for  $m = 1$  (the range of kept states is fully reproduced), and



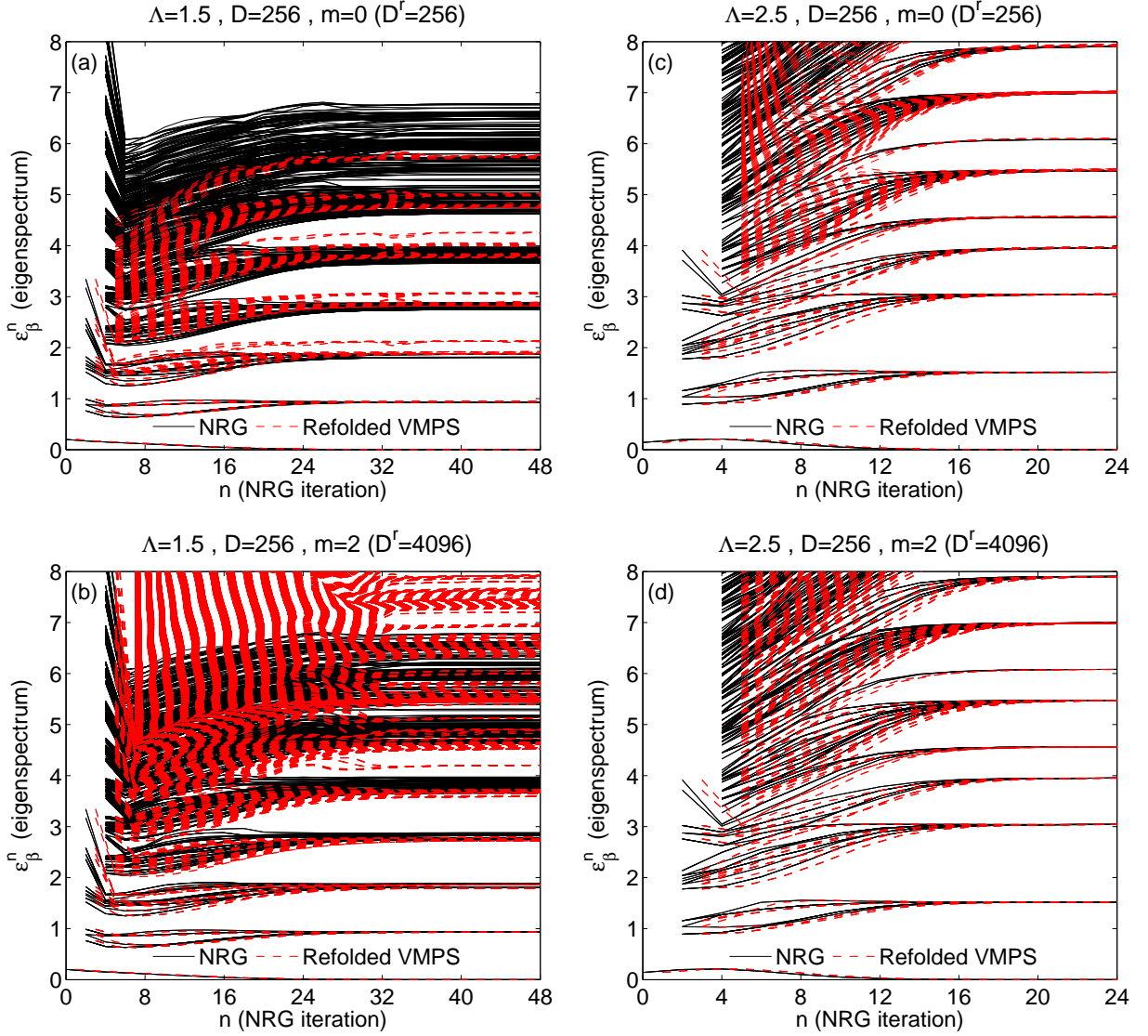


**Figure 4.7:** Comparison of energy flow diagrams from NRG (dashed red lines) and refolded VMPS data (solid black lines), showing the rescaled energies  $(\varepsilon_\beta^n)_{f,r}$  [Eq. (4.10)] versus  $n$ , calculated for even iteration numbers and four combinations of  $m$  ( $= 0$  or  $2$ ) and  $\Lambda$  ( $= 1.5$  or  $2.5$ ). The number of NRG states shown (kept *and* discarded) is  $Dd$ ; the number of refolded VMPS states shown is  $D^r = D'^2 = d^m D$ , this being the maximal dimension of refolded matrices  $B^{[\sigma_n]}$ . For  $m = 2$  and  $\Lambda = 2.5$ , the NRG and DMRG flow diagrams agree very well, see (d).

very good for  $m = 2$  (disagreement sets in only close to the upper end of range of discarded states).

Thirdly, for large  $n$ ,  $\rho_n(\varepsilon)$  becomes increasingly spiky. This reflects the fact that the spectrum approaches a fixed point with regularly-spaced eigenenergies, as is evident in the

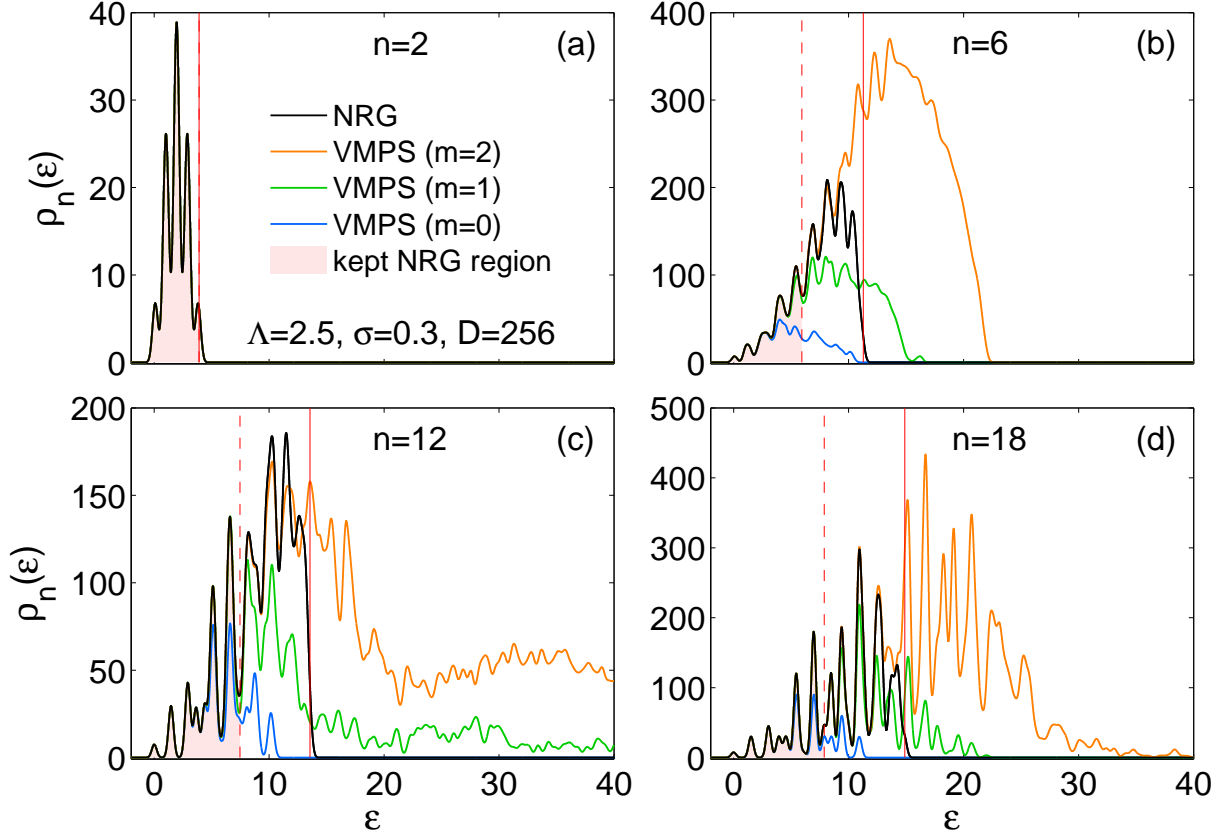


**Figure 4.8:** Results for the density of states,  $\rho_n(\epsilon)$  [Eq. (4.26)], broadened with a Gaussian broadening function. In each panel, the red vertical dashed and solid lines [which coincide in (a)] indicate the energies of the highest-lying kept and discarded NRG states of that iteration, while the shaded area indicates the range of kept NRG states.

energy flow diagrams of Fig. 4.7.

### 4.5.3 Comparison of energy eigenstates

To compare the energy *eigenstates* produced by NRG and refolded VMPS for a chain of length  $n$ , we analyze the overlap matrix

$$S_{\alpha\beta}^n = {}_r\langle E_\alpha^n | E_\beta^n \rangle_f. \quad (4.27)$$

It can be conveniently calculated from  $S^n = U^n \tilde{S}^n$ , where  $U_{\alpha\beta}^n = {}_r\langle E_\alpha^n | \Psi_\beta^n \rangle_r$  is the matrix that diagonalizes the effective Hamiltonian matrix  $\mathcal{H}_{\alpha\beta}^n$  of Eq. (4.23), and the matrix

$$\tilde{S}_{\alpha\beta}^n = {}_r\langle \Psi_\alpha^n | E_\beta^n \rangle_f, \quad (4.28a)$$

$$= \sum_{\{\sigma^N\}} (B^{[\sigma_n]^\dagger} \dots B^{[\sigma_0]^\dagger})_{\alpha 1} (A^{[\sigma_0]} \dots A^{[\sigma_n]})_{1\beta} \quad (4.28b)$$

characterizes how much weight the NRG eigenstates have in the space spanned by the refolded VMPS basis states, and vice versa. The contractions implicit in Eq. (4.28b) are illustrated in Fig. 4.6(b).

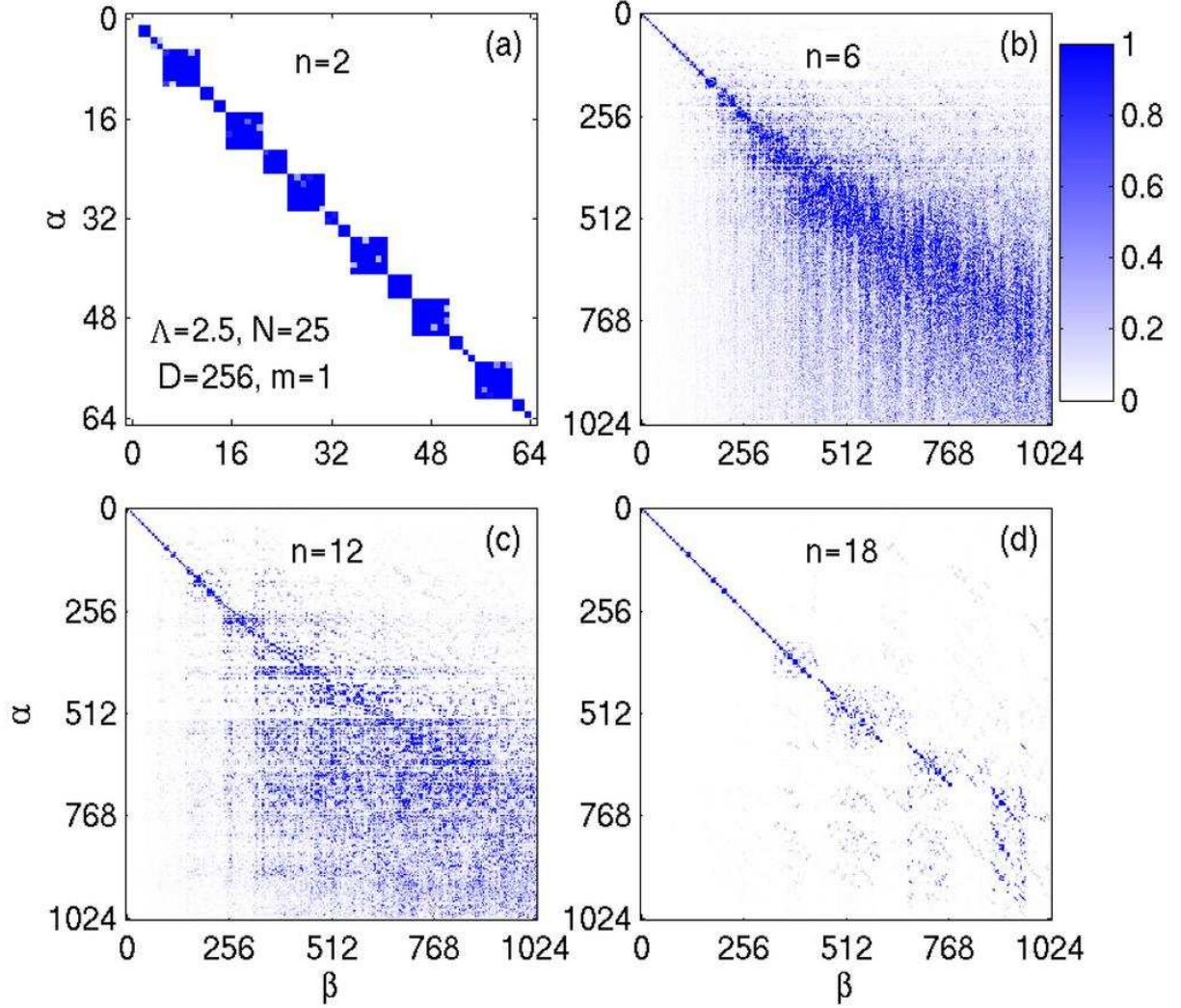
Figure 4.9 shows the overlap matrix  $S_{\alpha\beta}^n$  on a color scale ranging from 0 to 1, for  $m = 1$  and several values of  $n$ . For the region of low excitation energies (about the first hundred or so states) its structure is evidently close to block-diagonal, indicating that both sets of states from which it is built are reasonably good energy eigenstates. Had both sets been perfect energy eigenstates, as would be the case for  $D'$  and  $D$  large enough to avoid all truncation, the blocks would be completely sharp, with sizes determined by the degeneracies of the corresponding energies. Sharp blocks are indeed observed for  $n = 2$  [Fig. 4.9(a)], because no truncation has occurred yet. The “fuzziness” shown by the blocks in Fig. 4.9(b) to 4.9(d) for larger  $n$  implies that truncation is beginning to make itself felt, causing NRG and VMPS to increasingly disagree on how to construct the eigenstates corresponding to a given range of eigenenergies. Note that the fuzziness becomes markedly more pronounced for  $\alpha, \beta > 256$ . The reason is that whenever  $S_{\alpha\beta}^n$  is nonzero for  $\beta > D$ , the associated VMPS states have weight among the discarded states of NRG, implying that NRG discards some states relevant for building the VMPS ground state. Thus,  $S_{\alpha\beta}^n$  quite literally measures to what extent the truncation criteria of NRG and VMPS are compatible. Near the end of the chain, for  $n = 18$  [Fig. 4.9(d)], the off-diagonal spread is significantly reduced compared to the middle of the chain ( $n = 6, 12$ ) [Fig. 4.9(b,c)], for two reasons. Firstly, the dimensions of the refolded  $B$ -matrices become small for  $n$  near  $N$ , see Eq. (4.21), so that the amount of truncation is much less severe near the end of the chain than in its middle. Secondly, the eigenspectra have converged to their fixed point values, so that the number of different eigenenergies in a given energy interval is reduced, thus reducing the fuzziness in Fig. 4.9(d).

Next consider the total weight which a given NRG-state  $|E_\beta^n\rangle_f$  has within the refolded VMPS-subspace for that  $n$ ,

$$w_\beta^{(n)} = \sum_{\alpha=1}^{D_n^r} |S_{\alpha\beta}|^2 = \sum_{\alpha=1}^{D_n^r} |\tilde{S}_{\alpha\beta}|^2. \quad (4.29)$$

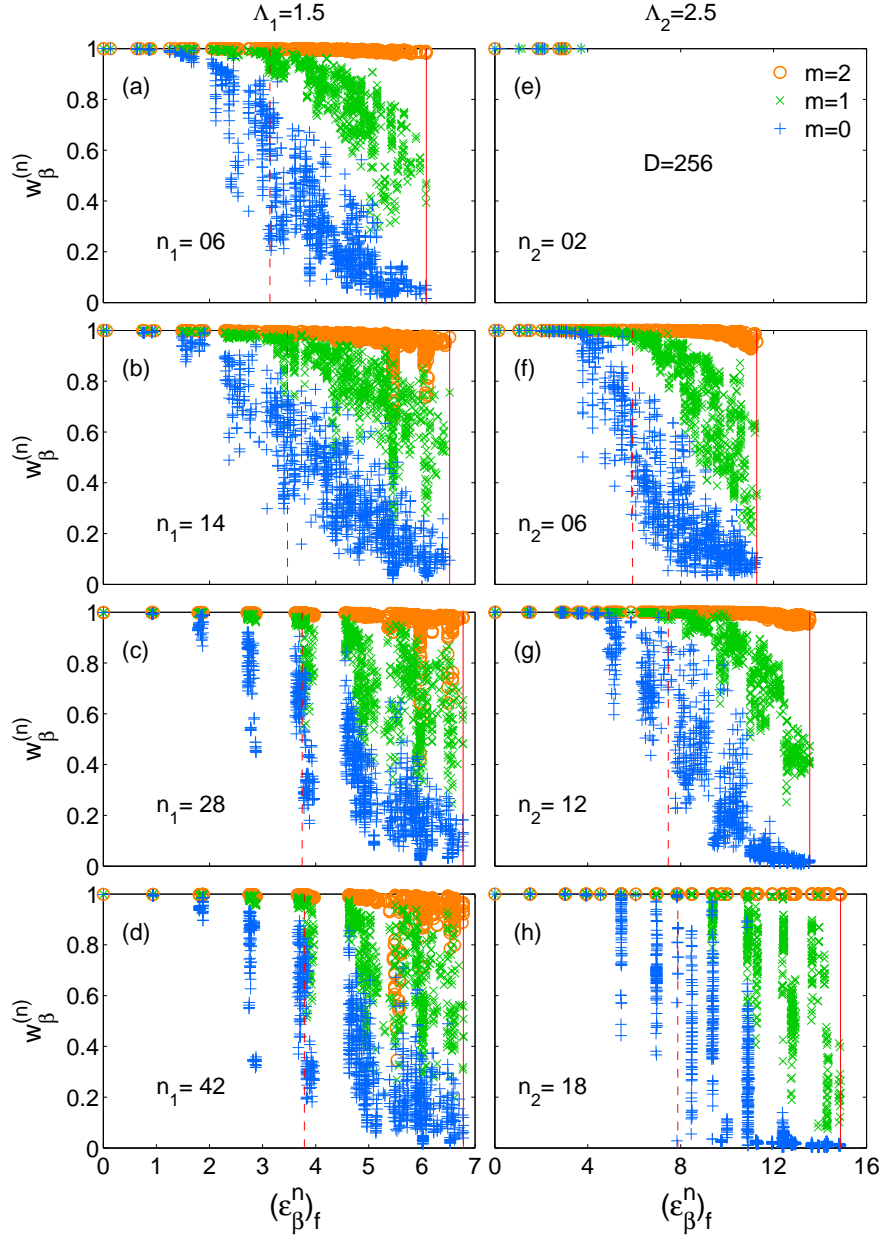
It satisfies  $0 \leq w_\beta^{(n)} \leq 1$ . Weights less than 1 imply that the VMPS-subspace is too small to adequately represent the corresponding NRG state. The second equality in Eq. (4.29), which follows from the unitarity of  $U$ , is useful since it implies that these weights can also be calculated directly from the refolded states  $|\Psi_\beta^n\rangle_r$  [Eq. (4.22)], without the need for diagonalizing the large ( $D'^2 \times D'^2$ -dimensional) effective refolded Hamiltonian  $\mathcal{H}_r^n$  [Eq. (4.23)].

Figure 4.10 shows such weights  $w_\beta^{(n)}$  for various choices of  $n$ ,  $\Lambda$  and  $m$ . Their dependence on  $m$  reinforces the conclusions of the previous subsection: For  $m = 0$  (blue + symbols), the weights are equal to 1 for the lowest state of each iteration, but less than 1 for many of the kept states. This shows that the VMPS subspace is large enough to accurately represent the NRG ground state, but significantly too small to accurately represent all kept states. For  $m = 1$  (green  $\times$  symbols), the weights are close to 1 only for the kept



**Figure 4.9:** Plot of the overlap matrix  $S_{\alpha\beta}^n = {}_r\langle E_\alpha^n | E_\beta^n \rangle_f$  [Eq. (4.27)] between refolded VMPS and NRG energy eigenstates, with a color scale ranging between 0 and 1. In (a), with  $n = 2$ , no truncation occurs at all, and both state labels  $\alpha$  and  $\beta$  run from 1 to  $d^{n+1} = 64$ . In (b) to (d), truncation does occur: For the folded NRG eigenstates  $|E_\beta^n\rangle_f$ , the label  $\alpha$  runs from 1 to  $Dd = 1024$ , i.e. it includes all kept and discarded NRG states, while for the refolded VMPS eigenstates  $|E_\beta^n\rangle_r$ , the label  $\beta$  runs from 1 to  $D_n^r = D^2 = 1024$  [Eq. (4.21)].

states, while smoothly decreasing towards 0 for higher-lying discarded states. Finally, for  $m = 2$  (orange  $\circ$  symbols), the weights of both kept and discarded NRG states are all close to 1, implying that the VMPS subspace is large enough to accurately represent essentially *all* states kept track of by NRG. Note that for  $m = 0$  and 1, the decrease of the weights  $w_\beta^{(n)}$  with increasing energy occurs in a smooth and gradual fashion, illustrating yet again the smooth nature of VMPS truncation when viewed in energy space. When a smaller value



**Figure 4.10:** For several NRG iteration numbers  $n$  and two values of  $\Lambda$  (different panels), this figure shows the weights  $w_\beta^{(n)}$  [Eq. (4.29)] with which NRG states  $|E_\beta^n\rangle_f$  with rescaled NRG eigenenergies  $(\varepsilon_\beta^n)_f$  [Eq. (4.10)] are found to lie in the VMPS-subspace of dimension  $D' = d'^m \sqrt{D}$ , with  $m = 0, 1$  or  $2$  (indicated by  $+$ ,  $\times$  or  $\circ$ , respectively). In each panel, the red vertical dashed and solid lines indicate the energies of the highest-lying kept and discarded NRG states of that iteration. For  $n = 3$ , both of these lines are missing, since truncation has not yet set in. The choices for  $n$  in the left and right panels of each row are related by  $\Lambda_1^{-n_1/2} = \Lambda_2^{-n_2/2}$ , to ensure that both panels show a comparable energy scale.

of  $\Lambda$  is used [compare panels (a-d) to (e-h)] the weights of the higher-lying states of a given iteration tend to spread out over a larger range of values, since NRG has a weaker energy scale separation for smaller  $\Lambda$ . Finally, the increasing spikyness of the eigenspectrum with increasing  $n$ , see Fig. 4.10(d,h), is due to the approach to a fixed point spectrum with regularly-spaced eigenenergies, as mentioned above.

The results just discussed may be represented more compactly by considering, for a given iteration  $n$ , the integrated weights obtained by summing up the weights of *all* NRG states of type  $X$ ,

$$W_X^{(n)} = \frac{1}{dD} \sum_{\beta \in X} w_\beta^{(n)}, \quad (4.30)$$

where  $X = K, D, A$  stands for *kept*, *discarded* or *all*, respectively. All three types of integrated weights are normalized to the total number  $dD$  of all NRG states calculated at a given iteration (with  $d = 4$  here), and reach their maximal values ( $\frac{1}{4}$ ,  $\frac{3}{4}$  and 1, respectively) when all the individual weights for that iteration equal 1. Figure 4.11 shows such integrated weights for several values of  $m$  and  $\Lambda$ . Upon increasing  $m$  from 0 to 2, the integrated weights tend toward their maximal values, doing so more rapidly for larger  $\Lambda$ . For  $m = 2$ , they essentially saturate their maximal values, indicating yet again that the VMPS variational space is now large enough to fully retain all information kept track of by NRG.

To summarize the result of this section: The VMPS approach reproduces NRG ground state properties much more cheaply, requiring only  $D' = \sqrt{D}$  for qualitative agreement, and  $D' = d'\sqrt{D}$  for quantitative agreement. Moreover, it can also reproduce all kept and discarded NRG eigenstates if  $D' = d'^2\sqrt{D}$  is used. However, to obtain excited energy eigenstates, we have to refold, requiring the diagonalization of matrices of dimension  $D'^2 \times D'^2$ . The numerical cost of doing so is comparable to that of NRG.

The fact that VMPS gives access to the same information on eigenstates and eigenvalues as NRG has a very significant and reassuring consequence: *all* physical properties of the model that can be calculated by NRG can also be calculated by VMPS, in combination with refolding.

## 4.6 Cloning and variational improvement of NRG ground state

Viewed in MPS language, the NRG method constructs the ground state in a single sweep along the chain: each  $A$  is calculated only once, without allowing for possible feedback of information from  $A$ 's describing lower energies to those of higher energies calculated earlier. Thus, the resulting NRG ground state  $|E_G^N\rangle_f$ , to be denoted simply by  $|G\rangle_f$  below, is not optimal in a variational sense. In this section we investigate to what extent the ground state energy can be lowered further by performing variational energy optimization

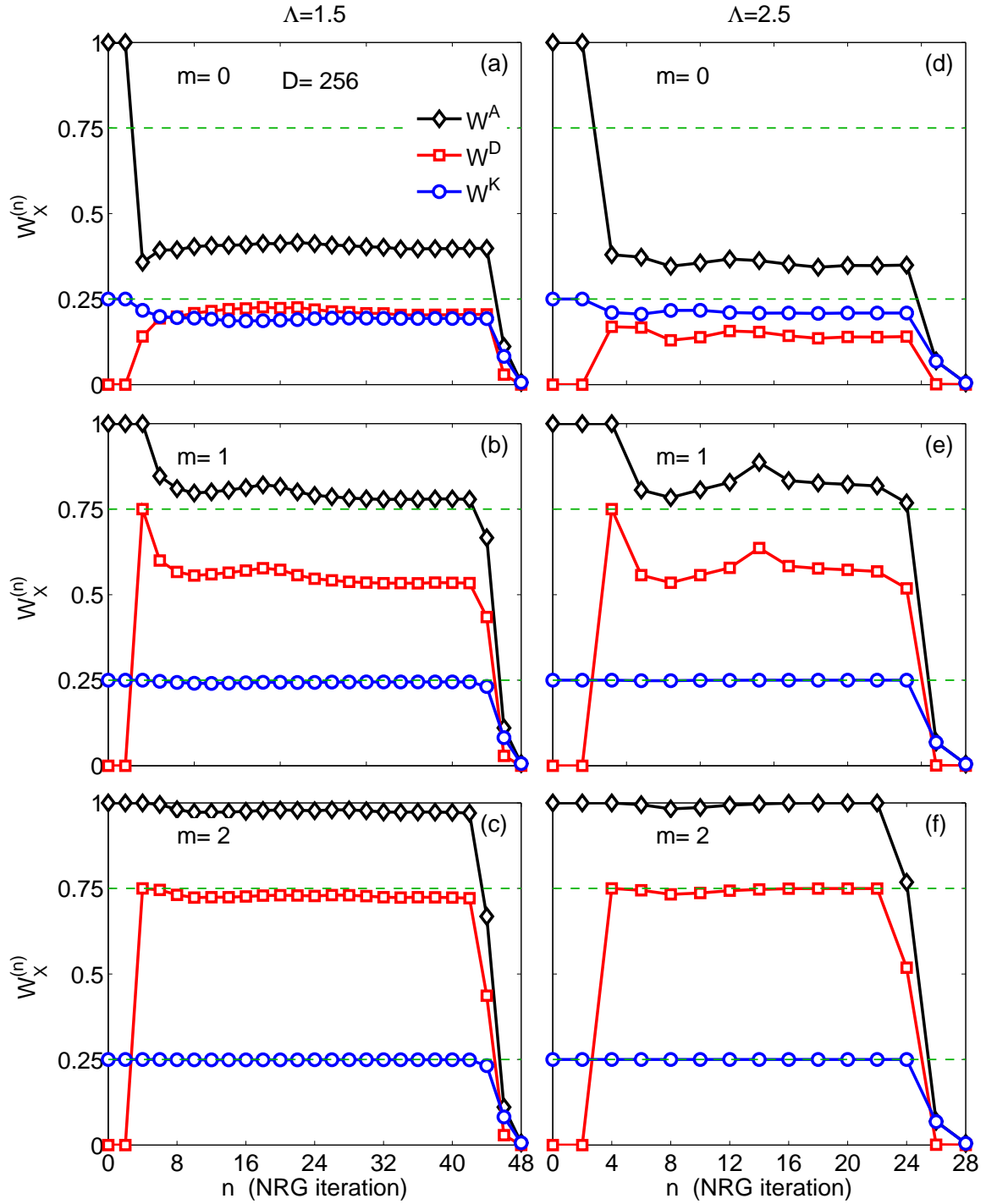


**Figure 4.11:** Integrated weights  $W_X^{(n)}$  (see Eq. (4.30)) for two different  $\Lambda$  and three values of  $m$ . Dashed lines depict the maximum possible values of the kept and discarded weights,  $\frac{1}{4}$  and  $\frac{3}{4}$  for  $W_K^n$  and  $W_D^n$ , respectively.

sweeps on  $|\mathsf{G}\rangle_{\mathsf{f}}$  that serve to account for feedback of information from low to high energy scales. This feedback turns out to be small in practice, as will be seen below, but it is not strictly zero and its importance increases as the logarithmic discretization is refined by taking  $\Lambda \rightarrow 1$ .

### 4.6.1 Mapping folded to unfolded states by cloning

Our first step is to rewrite a given NRG ground state  $|\mathsf{G}\rangle_{\mathsf{f}}$  in a form amenable to subsequent energy minimization sweeps. To this end, we use a variational *cloning* procedure (subscript  $\mathsf{c}$ ),

$$|\mathsf{G}\rangle_{\mathsf{f}} \xrightarrow{\text{cloning}} |\mathsf{G}\rangle_{\mathsf{c}} \in \{|\Psi^N\rangle_{\mathsf{u}}\}, \quad (4.31)$$

which maps  $|\mathsf{G}\rangle_{\mathsf{f}}$  of the form of Eq. (4.7) [Fig. 4.2(a)] onto an unfolded state  $|\mathsf{G}\rangle_{\mathsf{c}}$  of the form  $|\Psi^N\rangle_{\mathsf{u}}$  of Eq. (4.16) [Fig. 4.2(c)]. Since their matrix-product structures differ, this mapping will, for general values of  $D$  and  $D'$ , not be exact, though its accuracy should improve systematically with increasing  $D'$  and hence increasing dimensions of the variational space. To be explicit, we seek the best possible approximation to  $|\mathsf{G}\rangle_{\mathsf{f}}$  in the space of all unfolded states of the form (4.16), by solving the minimization problem

$$\min_{|\mathsf{G}\rangle_{\mathsf{c}} \in \{|\Psi^N\rangle_{\mathsf{u}}\}} \left[ \|\mathsf{G}\rangle_{\mathsf{f}} - |\mathsf{G}\rangle_{\mathsf{c}}\|^2 + \lambda(\|\mathsf{G}\rangle_{\mathsf{c}}\|^2 - 1) \right], \quad (4.32)$$

which minimizes the “distance” between  $|\mathsf{G}\rangle_{\mathsf{c}}$  and  $|\mathsf{G}\rangle_{\mathsf{f}}$  under the constraint, implemented using a Lagrange multiplier  $\lambda$ , that the norm  ${}_c\langle\mathsf{G}|\mathsf{G}\rangle_{\mathsf{c}} = 1$  remains constant. Varying Eq. (4.32) with respect to the matrices defining  $|\mathsf{G}\rangle_{\mathsf{c}}$  leads to a set of equations, one for each  $k\mu$ , of the form

$$\frac{\partial}{\partial B^{[\sigma_{k\mu}]}} \left[ (1 + \lambda) {}_c\langle\mathsf{G}|\mathsf{G}\rangle_{\mathsf{c}} - 2\text{Re}({}_f\langle\mathsf{G}|\mathsf{G}\rangle_{\mathsf{c}}) \right] = 0, \quad (4.33)$$

which determine the  $B$ -matrices of the desired “cloned” state  $|\mathsf{G}\rangle_{\mathsf{c}}$ . These equations can be solved in a fashion entirely analogous to energy optimization: Pick a particular site of the unfolded chain, say  $k\mu$ , and solve the corresponding Eq. (4.33) for the matrix  $B^{[\sigma_{k\mu}]}$  while regarding the matrices of all other sites as fixed. Then move on to the neighboring site and in this fashion sweep back and forth through the chain until convergence is achieved. Appendix D describes some details of this procedure.

A figure of merit for the success of cloning is the deviation of the overlap  ${}_c\langle\mathsf{G}|\mathsf{G}\rangle_{\mathsf{f}}$  from 1. This deviation decreases monotonically with successive cloning sweeps and converges to a small but finite ( $D'$ -dependent) value when the cloning process converges, as illustrated in the inset of Fig. 4.12. The main part of Fig. 4.12 shows that when the number  $D'$  of VMPS states is increased, the converged value of the overlap deviation approaches 0 as a power law in  $D'$  (red circles). It also shows that the corresponding VMPS truncation error  $\tau(D')$  incurred during cloning (blue squares), calculated according to Eq. (4.19), likewise decreases in power-law fashion with  $D'$ . All in all, Fig. 4.12 confirms that cloning works very well if  $D'$  is sufficiently large.



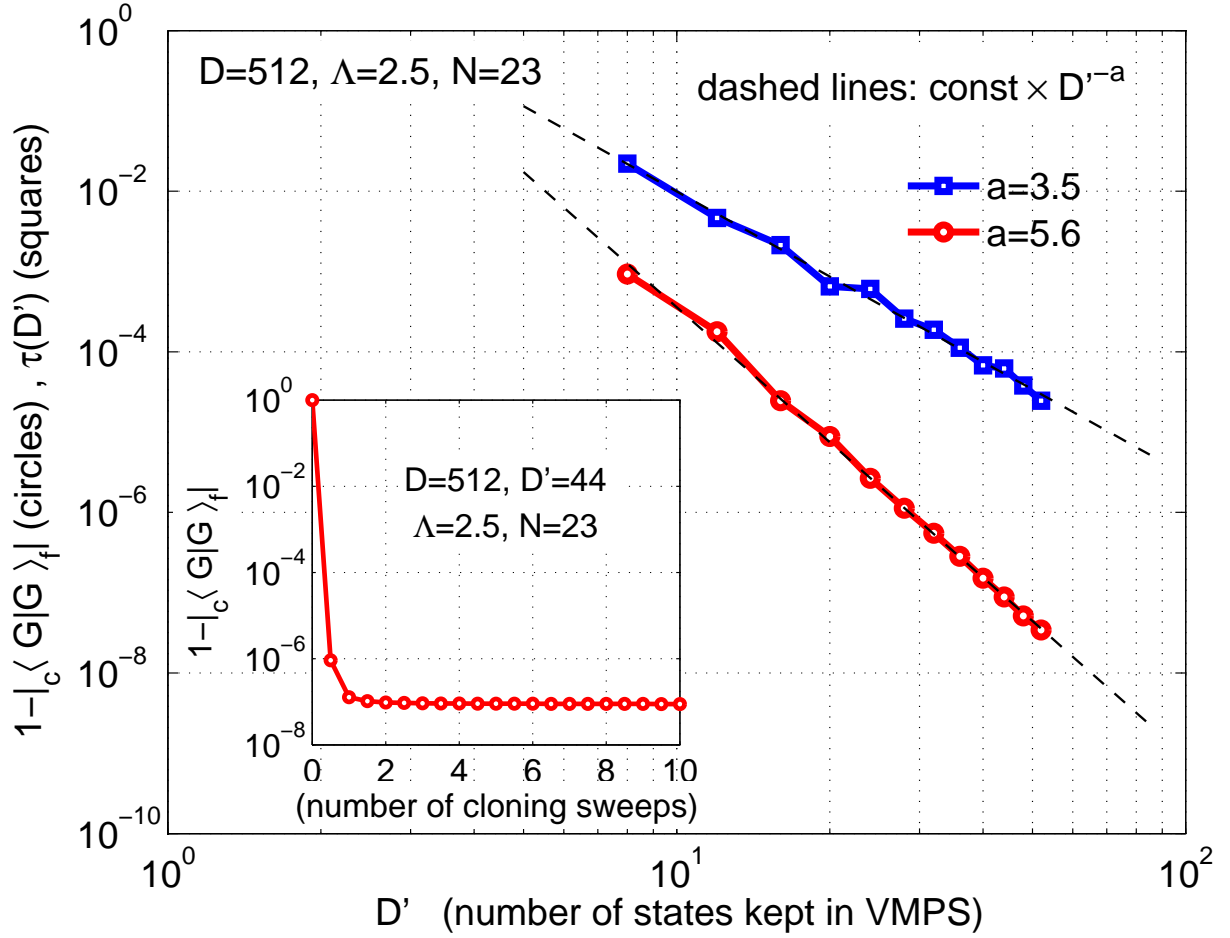


**Figure 4.12:** The deviation of the overlap  $|\langle G|G \rangle_f|$  from 1 (red circles) and the cloning truncation error  $\tau(D')$  (blue squares), as functions of the number  $D'$  of kept states in the cloning procedure. Both approach 0 in power-law fashion, as indicated by the dashed line fits. The inset shows how the overlap deviation from 1 decreases and converges to a small but finite constant in the course of sequential cloning sweeps.

### 4.6.2 Variational energy minimization of $|G\rangle_c$

Having used cloning to find the optimal unfolded representation  $|G\rangle_c$  of the NRG ground state  $|G\rangle_f$ , we now variationally minimize its energy by sweeping. We thereby obtain a sequence of states  $|G\rangle_c^{k_{\text{em}}}$  of ever lower energy,  $E_{k_{\text{em}}}$ , where the index  $k_{\text{em}} = 0, 1, 2, \dots$  gives the number of energy minimization sweeps that have been performed. The procedure is precisely analogous to that described in Section 4.4.1, the only difference being that the random initial state used there is here replaced by the cloned state  $|G\rangle_c^0 = |G\rangle_c$  as initial state.

Figure 4.13(a) shows the evolution of the ground state energy  $E_{k_{\text{em}}}$  as function of the number  $k_{\text{em}}$  of energy minimization sweeps, for both random (squares) and cloned (circles)

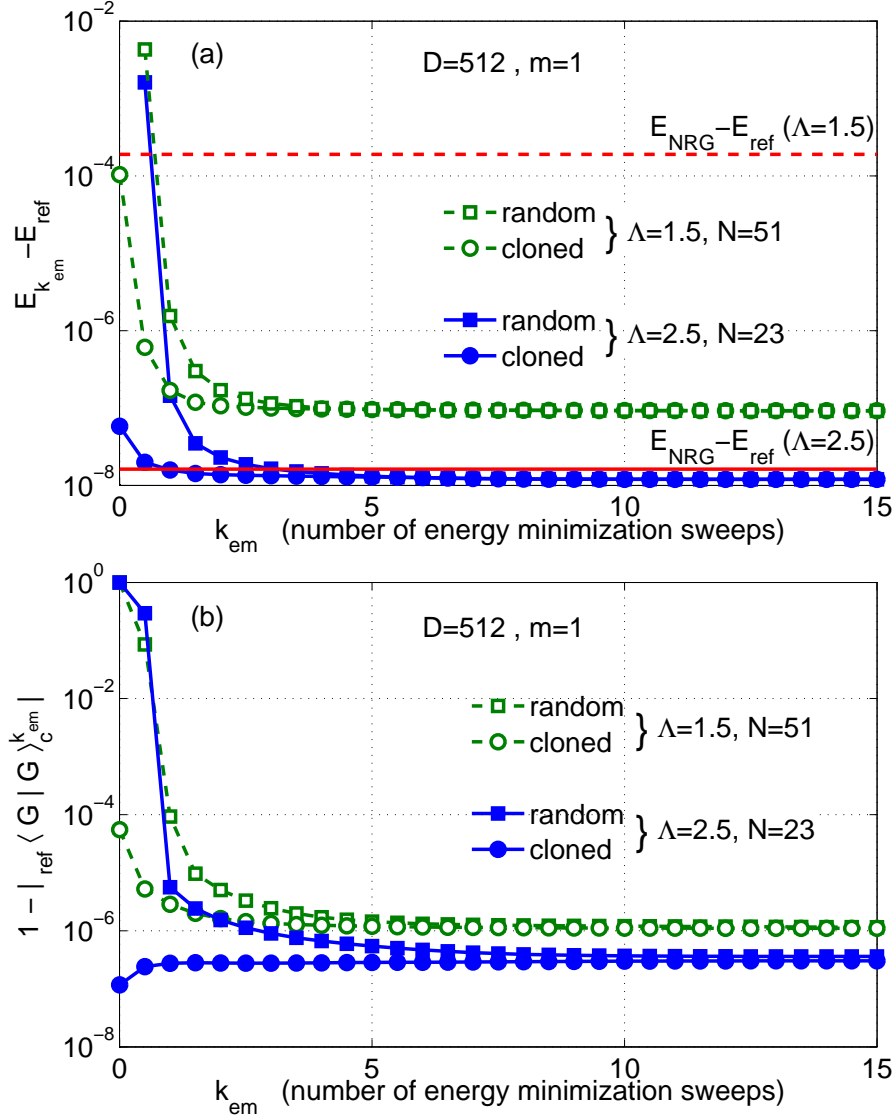


**Figure 4.13:** Comparison of (a) energies and (b) wave function overlaps for random initialization (squares) vs. NRG-cloned initialization (circles), as functions of the number  $k_{em}$  of variational energy minimization sweeps. Results are shown for  $\Lambda = 1.5$  (green, open symbols, dashed lines) and  $\Lambda = 2.5$  (blue, filled symbols, solid lines). The energies in (a) and overlaps in (b) are calculated with respect to a reference ground state  $|G\rangle_{ref}$  with  $D' = 64$ , obtained by performing 50 energy minimization sweeps starting from random initialization. The red horizontal straight lines in (a) (dashed or solid for  $\Lambda = 1.5$  or  $2.5$ , respectively), show the energy difference  $E_{NRG} - E_{ref}$ , where  $E_{NRG}$  is the energy of the NRG ground state  $|G\rangle_f$  used as input into cloning. The fact that  $E_{NRG}$  does not completely coincide with the energy  $E_c = E_{k_{em}=0}$  of the cloned state (horizontal straight lines do not meet circles at  $k_{em} = 0$ ) is due to the fact that the deviation of the overlap  $|\langle G | G \rangle_f|$  from 1 is not strictly equal to 0 (see Fig. 4.12).

initial states.  $E_{k_{\text{em}}}$  is displayed with respect to the energy  $E_{\text{ref}}$  of a reference state  $|G\rangle_{\text{ref}}$ , defined in the figure caption, which represents our best approximation to the true ground state. Figure 4.13(b) shows how  $1 - |\langle G|G\rangle_c|$  decreases as sweeping proceeds, converging to a small but finite value. For a given value of  $\Lambda$  (1.5, shown in green, open symbols connected by dashed lines, or 2.5, shown in blue, filled symbols connected by solid lines), the energies for random and cloned initialization shown in Fig. 4.13(a) converge to the same value within just a few sweeps. However, the convergence is quicker for the cloned (circles) than the random (squares) input state, since the former represents an already rather good initial approximation (namely that of NRG) to the true ground state, whereas the latter is simply a random state. Nevertheless, the circles show strikingly that the NRG ground energy is *not* optimal, in that the energy can be lowered still further by sweeping. Moreover, this improvement is more significant for small than large  $\Lambda$  (for circled data points, compare dashed green to solid blue lines for  $\Lambda = 1.5$  or  $2.5$ , respectively). The reason is that the NRG truncation scheme becomes less accurate the smaller  $\Lambda$  is, implying that the NRG result can be improved more significantly by further sweeping. This is again a reminder that the systematic error of NRG increases as  $\Lambda$  approaches 1, as already observed in Fig. 4.5.

## 4.7 Conclusions

In this chapter we presented a systematic comparison between NRG and DMRG, which we mainly referred to as VMPS, for the single-impurity Anderson model within the framework of matrix-product states. We first reformulated both NRG and DMRG in the language of MPS, using a folded Wilson chain for NRG and an unfolded one for DMRG. Then we quantitatively compared the results of NRG and the VMPS approach for energy eigenvalues and eigenstates and explicitly analyzed the difference in their truncation criteria, which are sharp or smooth in energy space, respectively.

The most important conclusion of our study is this: For the purpose of obtaining the ground state of this model, the VMPS approach applied to the unfolded Wilson chain yields a very significant increase in numerical efficiency compared to NRG ( $D' = d'\sqrt{D}$ ), essentially without loss of relevant information. The physical reason is that the spin-down and -up chains are only weakly entangled for this model, so that the NRG matrices  $A^{[\sigma_n]}$  of dimension  $D$  that describe site  $n$  of the Wilson chain, can, in effect, be factorized as a direct product  $B^{[\sigma_{n\downarrow}]} \otimes B^{[\sigma_{n\uparrow}]}$  of two matrices, each having dimension  $d'\sqrt{D}$ . It should be emphasized, though, that this property relies on the physics of the model, namely the weak entanglement of the spin down and up chains. To what extent this property survives for other impurity models should be a subject for further research, the two-channel Kondo model being a particularly interesting candidate in this respect.

Nevertheless, the possibility of using unfolded Wilson chains to reduce numerical costs for ground state calculations is very attractive for possible applications of the VMPS method to more complicated models involving more than one conduction band [79, 80]. For

example, the conductance through a quantum dot coupled to two leads can under certain conditions (linear response, zero temperature, Fermi liquid behavior, etc.) be expressed in terms a set of phase shifts that are uniquely determined by the ground state occupation of the dot energy levels [81]. Thus, in such situations reliable knowledge of the ground state is sufficient to calculate transport properties.

Going beyond ground state properties, we showed that the entire excited state eigenspectrum of both kept and discarded NRG states can be recovered within the VMPS approach with at least the same accuracy as NRG, by using  $D' = d'^2 \times \sqrt{D}$  and refolding. However, the latter step requires a subsequent additional diagonalization of matrices of dimensions  $D'^2$ , giving rise to a significant increase in numerical resources compared to the case that only ground state information is required. A quantitative comparison between NRG and VMPS for the eigenspectrum's energies and eigenstates showed better agreement for  $\Lambda = 2.5$  than 1.5, due to the fact that the NRG truncation scheme becomes increasingly less accurate the closer  $\Lambda$  approaches 1.

Finally, we used a cloning procedure to recast a given folded NRG ground state into an unfolded form, and showed that its energy could be lowered further by subsequent energy minimization sweeps. As expected, we found that sweeping improves the relative accuracy with which the ground state energy can be determined, the more so the smaller the value of  $\Lambda$ . For example, for  $\Lambda = 1.5$  the accuracy changed from  $\mathcal{O}(10^{-4})$  before sweeping to  $\mathcal{O}(10^{-7})$  thereafter [see Fig. 4.13(a)]. The fact that such a further variational improvement of the NRG ground state is possible, however, is of significance mainly as a matter of principle, not of practice: for the numerous situations where NRG works well (in particular, for  $\Lambda$  not too close to 1), we expect that such further variational improvement of the NRG ground state will not noticeably affect any physical observables.

Let us conclude with some comments about the pros and cons of NRG and VMPS. For quantum impurity models with a comparatively low degree of complexity, such as the single-lead Anderson and Kondo models, NRG works exceedingly well and for practical purposes nothing is to be gained from switching to the VMPS approach. The latter is a potentially attractive alternative to NRG only for two types of situations, namely (i) more complex quantum impurity models, and (ii) non-logarithmic discretization of the leads. We briefly discuss these in turn.

(i) For complex quantum impurity models, in particular ones involving several leads, VMPS achieves a very significant reduction in memory cost, relative to NRG, for describing ground state properties via unfolding the Wilson chain. There are several caveats, though. Firstly, this reduction in memory cost applies only when *only* ground state properties are of interest. To obtain excited state eigenspectra, the memory costs of NRG and VMPS are comparable. Secondly, unfolding is expected to work well only for models for which the subchains that are being unfolded are only weakly entangled, which will not be the case for all impurity models. For example, the two-channel model might be an example where unfolding works less well. In general, one needs to check the extent to which degrees of freedom on different subchains are entangled with each other, by calculating the mutual information of two sites on different subchains. If this does not decrease rather rapidly with

their separation from the impurity site, then unfolding will be a poor strategy. Appealingly, though, such a check can be done purely using NRG data, as illustrated in Section 4.3.3. Thirdly, the fact that VMPS relies on variationally optimizing the ground state might cause convergence problems for models which have degenerate ground states. Conceivably this problem can be reduced by systematically exploiting all relevant symmetries of the Hamiltonian, including non-Abelian symmetries [22, 82, 36]. However, if states in the local state space of a folded Wilson chain are related by a non-Abelian symmetry, then this symmetry would not be manifest in the unfolded representation. Thus, the two possible strategies for achieving significant memory reduction, namely unfolding and exploitation of symmetries might not always be mutually compatible; which one is more favorable will depend on the details of the model, and is an interesting subject for further study.

(ii) The VMPS approach offers clear advantages over NRG in situations where Wilson's logarithmic discretization of the conduction band cannot be applied. In the present work, we found clear indications for this fact in the observation that the improvement of VMPS relative to NRG becomes more significant as  $\Lambda$  is chosen closer to 1. More importantly, VMPS offers the possibility, inaccessible to NRG, to improve the frequency resolution of spectral functions at high frequencies, by using a flexible (non-logarithmic) discretization scheme which reduces the level spacing of effective lead states in the energy regimes where higher frequency resolution is desired. For such a discretization scheme Wilsonian energy scale separation is lost and NRG truncation cannot be applied. However, the ground state can still be found variationally, and spectral functions can be computed using projection operator techniques. In this fashion, it has recently been possible to calculate the spectral function for the Anderson model at large magnetic fields,  $B > T_K$ , and to resolve the split Kondo resonance with sufficient accuracy to reproduce the widths expected from perturbation theory in this regime. These developments, though, go beyond the scope of the present work and will be published separately [51].



# Chapter 5

## Constrained optimization of sequentially generated entangled multiqubit states

*Parts of this chapter has recently been submitted for publication to Physical Review Letters:*

H. Saberi, A. Weichselbaum, L. Lamata, D. Pérez-Garcia, J. von Delft, and E. Solano, arXiv:0810.0977

In this chapter we consider the problem of sequential generation of entangled multiqubit states under real-world experimental constraints and demonstrate explicitly how the matrix-product state formalism provides a flexible structure to overcome these experimental restrictions.

In Section 5.1 a general introduction to the problem of sequential generation of entangled multiqubit states and the associated experimental challenges is presented. In Section 5.2 we address the issue of restrictions on the ancilla dimension. Here we use singular value decomposition (SVD) from linear algebra for approximating an MPS by another of lower bond dimension. More precisely, we explicitly demonstrate how a given MPS can be efficiently represented with the less amount of data originally required to represent it. The MPS formalism which encodes the relevant information in the form of products of matrices, has the advantage that enables us to make use of linear algebra tools for matrix analysis. In Section 5.2.1 we present these mathematical tools, which will be used in Section 5.2.2 for MPS compression. Finally, the issue of restricted source-qubit interactions will be addressed in Section 5.3.

## 5.1 Introduction

Entangled multiqubit states are of central importance in the fields of quantum computation and quantum communication [57], and have been the subject of intensive theoretical and experimental investigations. As pointed out by Schön *et al.* [31, 32], the classes of all sequentially generated multiqubit states, assisted by an itinerant ancilla, are exactly given by the hierarchy of matrix-product states (MPS) [23]. In this context, the required number of ancilla levels is determined by the dimension of the MPS *canonical* representation<sup>1</sup> of the target multiqubit state. Matrix-product states play an important role in the context of strongly correlated systems [75] and describe the approximate ground states produced by density-matrix renormalization group (DMRG) [5, 7, 8, 20, 21] and Wilson’s numerical renormalization group (NRG) [3, 83]. Paradigmatic multiqubit states, such as Greenberger-Horne-Zeilinger (GHZ) [28],  $W$  [29] and cluster [30] states, can be described by low dimensional MPS and are considered valuable resources for quantum information and communication tasks.

The generation of multiqubit entangled states via a single global unitary operation acting on initially decoupled qubits is in general a difficult problem. From this point of view, several theoretical and experimental efforts have been oriented towards the sequential generation of paradigmatic entangled multipartite states. As a matter of fact, a number of sequential and global approaches have been implemented in different physical systems to produce specifically GHZ [84, 64],  $W$  [85, 61, 86], and cluster [87] states. In order to generate sequentially any multiqubit state, a wide range of ancilla levels and ancilla-qubit operations are necessary [31]. In this spirit, two important theoretical and experimental questions appear naturally: will the sequential generation of a desired multiqubit state still be feasible under given restricted experimental conditions? And if the answer is no, can we design an efficient protocol that tells us the best possible approximation to the sequential generation of such state? In this chapter, we answer satisfactorily both questions. We demonstrate how the MPS formalism allows us to exploit linear algebraic tools to study this relevant constrained optimization problem [34].

## 5.2 Restrictions on the number of ancilla levels

It is known that any  $n$ -qubit state  $|\psi\rangle$  can be written canonically as an MPS with minimal dimension  $D(\leq 2^n)$  [23]. It was also shown that such state can be built sequentially with a  $D$ -dimensional ancilla, if we have access to arbitrary ancilla-qubit unitaries [31]. In the sequential generation of states, an ancillary system  $\mathcal{A}$  (e.g. a  $D$ -level atom) couples sequentially to an initially decoupled qubit chain  $|\psi_I\rangle = |\psi_I^{[n]}\rangle \otimes \cdots \otimes |\psi_I^{[1]}\rangle$  (e.g. cavity photonic qubits that leak out after interacting with an atom). Assuming that in the last step the ancilla decouples unitarily from the multiqubit system, we are left with the  $n$ -qubit

---

<sup>1</sup>See Section 3.3 for details on MPS canonical representation.



state [31]

$$|\psi\rangle = \sum_{i_n \dots i_1=0}^1 \langle \varphi_F | V_{[n]}^{i_n} \dots V_{[1]}^{i_1} | \varphi_I \rangle |i_n, \dots, i_1\rangle, \quad (5.1)$$

an MPS of bond dimension  $\dim(|\psi\rangle) = D$ , where the  $D \times D$ -dimensional matrix  $V_{[k]}^{i_k}$  represents the ancilla-qubit operation at step  $k$  of the sequential generation (with *isometry* condition <sup>2</sup>  $\sum_{i_k=0}^1 V^{i_k \dagger} V^{i_k} = \mathbf{1}$ ),  $|\varphi_I\rangle$  and  $|\varphi_F\rangle$  being the initial and final ancilla state, respectively. Hence, a relevant experimental question may be raised: how well can we represent a given multiqubit state  $|\psi\rangle$  if only an ancilla with a smaller number of levels,  $D' < D$ , is available? More formally: given a state  $|\psi\rangle$ , with canonical MPS representation of bond dimension  $D$ , what is the optimal MPS  $|\tilde{\psi}\rangle$  of lower bond dimension  $D' < D$  that minimizes their distance? We want to estimate

$$\min_{\dim(|\tilde{\psi}\rangle)=D' < D} \| |\psi\rangle - |\tilde{\psi}\rangle \|^2. \quad (5.2)$$

We propose two techniques to perform the MPS approximation above, both exploiting a suitably designed local optimization of the  $V$ -matrices in Eq. (5.1). In the first approach, we make use of a corollary of the singular value decomposition (SVD) theorem from linear algebra to perform a local optimization procedure which may be called ‘‘MPS compression’’, in analogy to the image compression technique already used in computer science and engineering [89, 90].

### 5.2.1 SVD for matrix approximation

In this section we make use of a corollary of singular value decomposition from linear algebra for approximating a matrix by another of lower *rank*. The notion of the distance between matrices is quantified in terms of the theory of *matrix norms* which is briefly reviewed in Appendix E. The SVD can be used to obtain an optimal approximation of a rectangular matrix by another of the same dimension, but smaller *rank* [91].

First of all, we draw attention to the fact that SVD provides a recipe to obtain an optimal full-rank representation of a rank-deficient matrix, since SVD inherently reveals an explicit representation of the rank of the matrices. To see this, we include the following corollary of the SVD theorem [91]:

COROLLARY 1: Given the SVD of  $A_{m \times n}$  and

$$\sigma_1 \dots \geq \sigma_r > \sigma_{r+1} = \dots = \sigma_p = 0, \quad (5.3)$$

<sup>2</sup> Note that, if a linear transformation  $U$  on an inner-product space is such that  $U^\dagger U = \mathbf{1}$ ,  $U$  is called an *isometry* or isometric transformation [88]. If, in addition,  $UU^\dagger = \mathbf{1}$ , then the isometry  $U$  is called a *unitary* transformation.

then  $A$  is a *rank-deficient* matrix and

$$\text{rank}(A) = r , \quad (5.4)$$

$$A = \sum_{i=1}^r \sigma_i u_i v_i^\dagger = U_r \Sigma_r V_r^\dagger , \quad (5.5)$$

where  $U_r = [u_1, \dots, u_r]$  and  $V_r = [v_1, \dots, v_r]$  and  $\Sigma_r = \text{diag}(\sigma_1, \dots, \sigma_r)$ .

This corollary reveals a great deal about the rank of a given matrix. Once we obtain the SVD of a matrix, it can be immediately understood whether the given matrix is full-rank or rank-deficient: If all the singular values of the matrix turn out to be non-zero, the matrix has as large a rank as possible and is said to have full-rank, otherwise it is called a rank-deficient matrix and the rank of the matrix is given by the number of non-zero singular values of that matrix. Since the sum in Eq. (5.5) runs from 1 to  $r$  (rather than  $p$ ) and  $r < p$ , this corollary implies that SVD inherently eliminates the superfluous dimensions. Note that Eq. (5.5) is now an *irreducible* representation of the matrix  $A$ , in the sense that the matrix  $A$  can not be represented by a lower dimensional matrix  $\Sigma$  anymore. Note also that Eq. (5.5) is an exact description of the original matrix  $A$  and no approximation has been made yet. Nevertheless, the following corollary of SVD provides us with a recipe to obtain the *best possible* lower-rank *approximation* to a full-rank matrix [91]. Before going through that, from Eq. (5.5) one may notice that the singular values  $\sigma_i$  may also be interpreted as the “weighting factors” of the expansion of matrix  $A$ . If any of the singular values turns out to be comparatively small, then the matrix  $A$  may be well-approximated by discarding the corresponding term of the expansion. This intuition may be justified more rigorously as follows:

**COROLLARY 2:** Let the SVD of the matrix  $A_{m \times n}$  with  $\text{rank}(A) = r$  be given by Eq. (5.5). Then the best possible lower-rank approximation to  $A$  which minimizes the following 2-norm distance

$$\min_{\text{rank}(\tilde{A})=k < r} \|A - \tilde{A}\|_2 , \quad (5.6)$$

is given by

$$\tilde{A} = \sum_{i=1}^k \sigma_i u_i v_i^\dagger . \quad (5.7)$$

Moreover, the distance above is given by

$$\|A - \tilde{A}\|_2 = \sigma_{k+1} . \quad (5.8)$$

Note that the matrix  $\tilde{A}$  in the corollary above has been given in terms of the SVD of the original matrix  $A$  in Eq. (5.5), i.e.  $U$ ,  $\Sigma$  and  $V$  in Eq. (5.7) are those of the matrix  $A$ , even though the matrix  $\tilde{A}$  could have been decomposed in terms of its own SVD matrices say  $\tilde{U}$ ,  $\tilde{\Sigma}$  and  $\tilde{V}$ . In other words, the decomposition (5.7) is identical to (5.5) except that the sum has been restricted to  $k$ . Therefore, the corollary suggests a constructive *truncation* scheme to obtain the nearest matrix of rank  $k$  ( $k < r$ ) to the original one:

1. Perform SVD for  $A$ , yielding  $A = U \Sigma V^\dagger$ .
2. Form the new truncated matrix  $\Sigma_t$  out of the  $\Sigma$  in SVD of  $A$ , by keeping the  $k$  largest singular values of  $A$  and discarding the remaining  $r - k$  ones (setting them to zero).
3. Replace the old  $\Sigma$  by the new truncated one  $\Sigma_t$  to obtain  $\tilde{A} = U \Sigma_t V^\dagger$  as the solution to the minimization problem.

Quite interestingly, it can be shown that the same holds for the  $F$ -norm distance between matrices so that the nearest lower-rank matrix is given by Eq. (5.7) but the corresponding distance reads [91]

$$\|A - \tilde{A}\|_F = \sqrt{\sum_{i=k+1}^r \sigma_i^2}. \quad (5.9)$$

So the corollary can be used as a *reconstruction* recipe to generate the most optimal matrices of lower rank out of a given original matrix. This is exactly the central idea of *image compression* technique used in computer science [89, 90]. Viewed in this language, the relative “compression error” (or truncation error) may be quantified by

$$\varepsilon_c = \frac{\|A - \tilde{A}\|_F}{\|A\|_F} = \frac{\sqrt{\sum_{i=k+1}^r \sigma_i^2}}{\sqrt{\sum_{i=1}^r \sigma_i^2}}, \quad (5.10)$$

where use has been made of Eq. (E.8) to express the error in terms of the singular values of the original matrix  $A$ . Thus, for a reasonably well-decaying singular values spectrum, the original matrix  $A$  may be well-approximated by (or “compressed” into)  $\tilde{A}$  obtained from the outlined procedure above. However,  $\tilde{A}$  will always give the best possible representation of  $A$  in the 2-norm and  $F$ -norm sense with less amount of numerical resources compared to that of the original one.

We now find it useful to define the *inner product* of two matrices in the Frobenius sense<sup>3</sup>

$$\langle A|B \rangle = \sum_{i=1}^m \sum_{j=1}^n a_{ij}^* b_{ij} = \text{Tr}(A^\dagger B). \quad (5.11)$$

---

<sup>3</sup> Note that in the case that  $A$  and  $B$  are matrix representations of *linear* operators, the inner product introduced in Eq. (5.11) will be the familiar *Hilbert-Schmidt* inner product associated with the Hilbert space of linear operators [57].

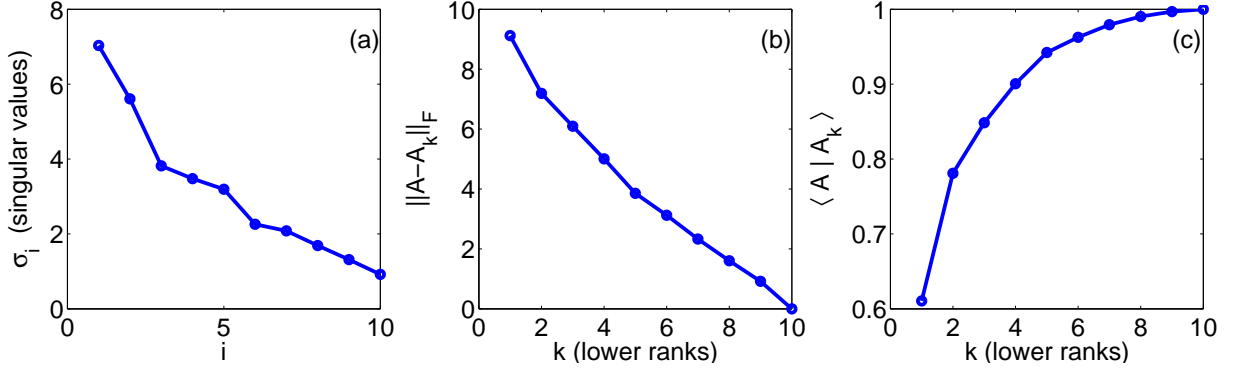


**Figure 5.1:** Matrix approximation with the aid of SVD. (a) The singular values of an arbitrary matrix  $A$  of rank 10. (b) The Frobenius distance between the original matrix  $A$  and the matrix  $A_k$  of rank  $k$  reconstructed out of  $A$  according to Eq. (5.7). (c) The Frobenius overlap between  $A$  and  $A_k$  (see Eq. (5.11)) as a measure of the quality of the matrix approximation procedure.

Note that the Frobenius norm of a matrix already defined in Eq. (E.1) may be recovered by choosing  $B = A$  in the inner product above

$$\|A\|_F = \sqrt{\langle A|A \rangle} = \sqrt{\sum_{i=1}^m \sum_{j=1}^n |a_{ij}|^2} = \sqrt{\text{Tr}(A^\dagger A)}. \quad (5.12)$$

Just as in the case of vectors, this inner product may be geometrically interpreted as the “angle” between two matrices, or alternatively regarding it as an *overlap*, it is also a measure of how much two matrices have in common in the Frobenius sense. To establish this connection note that

$$\|A - B\|_F^2 = \|A\|_F^2 + \|B\|_F^2 - 2 \text{Re}\{\langle A|B \rangle\}, \quad (5.13)$$

which clearly implies minimizing the Frobenius distance between two matrices is equivalent to maximizing their Frobenius overlap. Obviously, after normalizing a matrix, i.e. dividing it by its Frobenius norm, the overlap will be restricted to take values between -1 and 1.

As an illustrative case, Fig. 5.1 shows the results of applying the outlined SVD truncation scheme for an arbitrary matrix of rank 10 in the Frobenius sense.

Since the singular values are sorted in decreasing order and the corresponding distance is given by Eqs. (5.8) and (5.9), the distance-rank diagram will be always a monotonically decreasing function, in complete agreement with Fig. 5.1.

### 5.2.2 SVD for MPS compression

In this section we exploit the result of the last section for a single matrix to approximate an MPS by another of lower bond dimension. We call an MPS to be *compressible* if it can

be rewritten with the smaller bond dimension, otherwise we call it an *incompressible* MPS. Important examples of compressible MPSs are the  $W$ -state and GHZ state with number of qubits  $n > 2$  that can be written with MPS of bond-dimension  $D = 2$  (see Section 3.4).

Let the SVD of matrix  $A$  with  $\text{rank}(A) = r$  be given by  $A = \sum_{i=1}^r \sigma_i u_i v_i^\dagger$ . Then, the best possible lower-rank approximation to  $A$  that minimizes the Frobenius-norm distance  $\min_{\text{rank}(\tilde{A})=r' < r} \|A - \tilde{A}\|_F$  is given by  $\tilde{A} = \sum_{i=1}^{r'} \sigma_i u_i v_i^\dagger$  [91, 92]. This suggests a *truncation* scheme in which one keeps only the  $r'$  largest singular values of  $A$  to form the optimal lower-rank matrix  $\tilde{A}$ . We exploit now this property, valid for a *single* matrix, and apply the outlined truncation to each matrix  $V_{[k]}^{i_k}$ ,  $k = 1, \dots, n$ , in Eq. (5.1), yielding an MPS of lower bond dimension  $D' = D - (r - r')$ . This method offers a good solution for matrices with well-decaying singular values spectrum.

### 5.2.3 Variational optimization technique for the reduction of the ancilla dimension

In the second approach [83], a DMRG-inspired variational optimization of  $V$ -matrices [52], we seek the best possible approximation to  $|\psi\rangle$  in the space of all MPS  $|\tilde{\psi}\rangle$  of the form

$$|\tilde{\psi}\rangle = \sum_{i_n \dots i_1=0}^1 \langle \varphi_F | \tilde{V}_{[n]}^{i_n} \dots \tilde{V}_{[1]}^{i_1} | \varphi_I \rangle |i_n, \dots, i_1\rangle, \quad (5.14)$$

with bond dimension  $D' < D$ , by solving the minimization problem of Eq. (5.2) under the constant-norm condition  $\langle \tilde{\psi} | \tilde{\psi} \rangle = 1$ , which is implemented using a Lagrange multiplier  $\lambda$ . Varying Eq. (5.2) with respect to the matrices defining  $|\tilde{\psi}\rangle$  leads to a set of equations, one for each  $i_k$ , of the form

$$\frac{\partial}{\partial \tilde{V}_{[k]}^{i_k}} \left[ (1 + \lambda) \langle \tilde{\psi} | \tilde{\psi} \rangle - 2 \text{Re}(\langle \psi | \tilde{\psi} \rangle) \right] = 0, \quad (5.15)$$

which determines the optimal  $\tilde{V}$ -matrices of the desired state  $|\tilde{\psi}\rangle$ . These equations can be solved very efficiently using a “sweeping procedure” in which one fixes all but the  $k$ ’th  $\tilde{V}$ -matrix and solves the corresponding Eq. (5.15) for the matrix  $\tilde{V}_{[k]}^{i_k}$ . Then one moves on to the neighboring site and, in this fashion, sweeps back and forth through the chain until the convergence is reached. The optimization technique used here is reminiscent of the so-called “cloning” procedure used in Chapter 4 for mapping a folded state to an unfolded structure. The details of this method is given Appendix D. We point out, however, the main difference here being the target MPS ( $|\psi\rangle$ ) and the “clone” ( $|\tilde{\psi}\rangle$ ) are of the same folded structure.

Figure 5.2 illustrates the two optimization schemes outlined above for two different states, both with  $D = 16$ , namely (i) the ground state of the  $XXZ$  Heisenberg Hamiltonian and (ii) a randomly chosen MPS. For (i), which has a well-decaying singular-value spectrum, the ancilla dimension can be effectively reduced from 16 to 6. Since variational optimization allows for the feedback of information by several sweeps, it generally performs better than MPS compression.

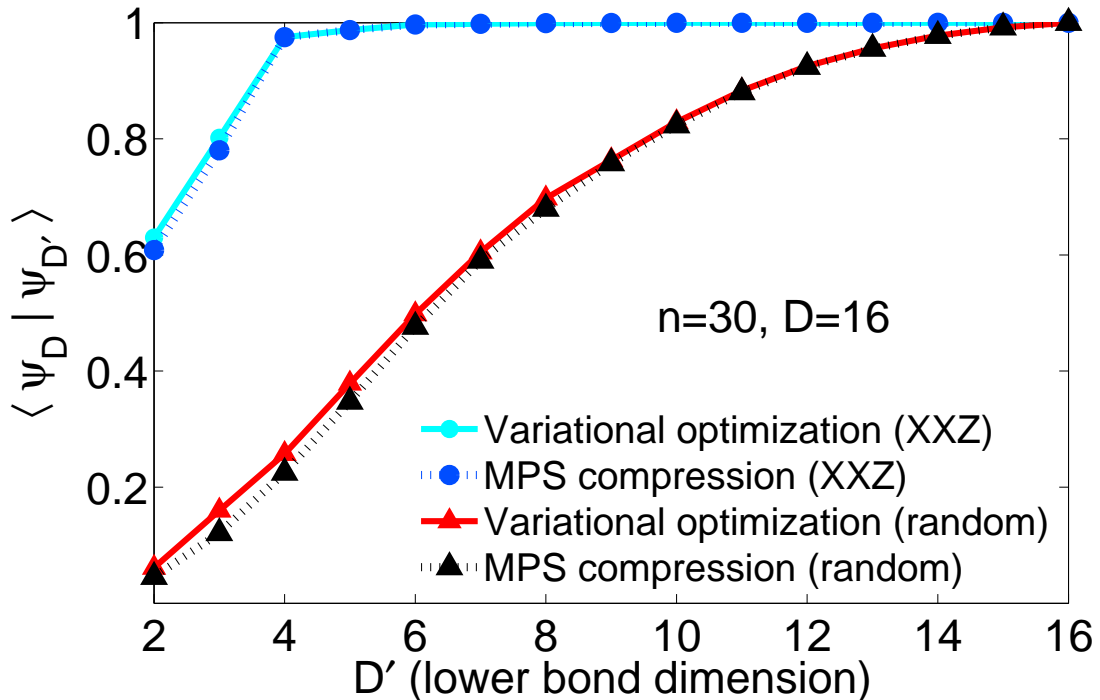


**Figure 5.2:** Comparison of the variational optimization approach (solid lines) with the MPS compression technique (dotted lines). We consider the ground-state of the  $XXZ$  Heisenberg Hamiltonian (circles) and a randomly initialized MPS (triangles), indicating how well these MPS with bond-dimension  $D$  can be approximated with those of dimension  $D' < D$ .

### 5.3 Restrictions on the source-qubit interactions

Every open-boundary MPS of the form

$$|\psi\rangle = \sum_{i_n \dots i_1=0}^1 \langle \varphi_F | A_{[n]}^{i_n} \dots A_{[1]}^{i_1} | \varphi_I \rangle |i_n, \dots, i_1\rangle, \quad (5.16)$$

with *arbitrary*  $A$ -matrices, not necessarily isometries, can be cast into a canonical MPS representation with minimal dimension  $D$  [53]. Such states, as mentioned above Eq. (5.1), can be generated sequentially [31], such that the ancilla decouples unitarily in the last step. We note that the sequential generating isometries can be constructed explicitly by successive SVD of the  $A$ -matrices and exploiting the gauge freedom of the matrix-product states as outlined in Refs. [31, 32]. This is a general recipe for the sequential generation of an *arbitrary* entangled multiqubit state if the required ancilla dimension  $D$  and ancilla-qubit unitaries are available. However, in general, a given physical setup may not have access to some of the required local ancilla-qubit unitaries. Given such a limitation, we face an interesting constrained optimization problem: which is the sequential protocol by

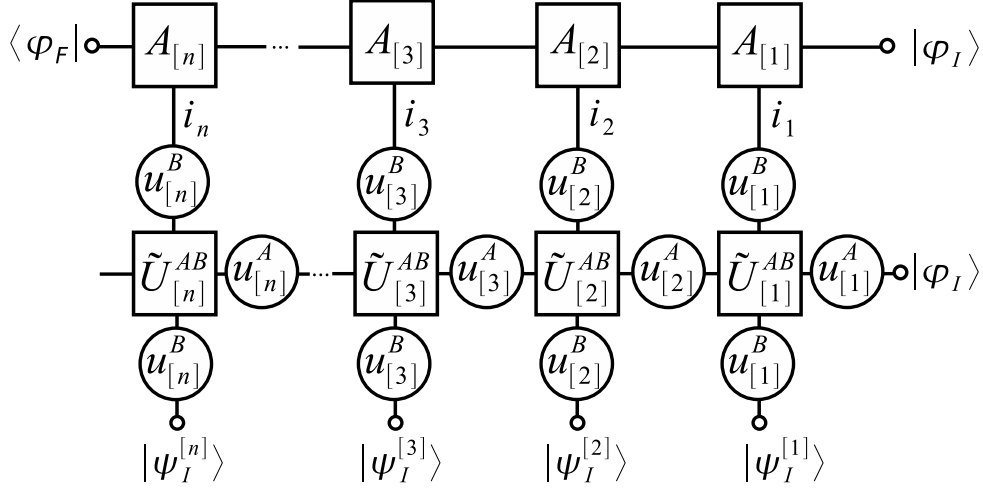


**Figure 5.3:** The contraction pattern used to calculate the cost function in Eq. (5.22) including the local ancilla operations  $\mathcal{U}^A$  and local qubit operations  $\mathcal{U}^B$ . The initial states of the qubits are denoted by  $|\psi_I^{[k]}\rangle$ .

which a given multiqubit “target” state can be approximately generated with maximal fidelity?

To address this problem, let us begin by considering the general unrestricted case: The unitary time evolution of the joint system ancilla-qubit at step  $k$  of the sequential generation may be described by a general unitary  $U_{[k]}^{AB} : \mathcal{H}_A \otimes \mathcal{H}_B \rightarrow \mathcal{H}_A \otimes \mathcal{H}_B$  given by

$$U_{[k]}^{AB} = e^{-iH_{[k]}^{AB}t/\hbar}, \quad (5.17)$$

where  $H_{[k]}^{AB}$  is a general bipartite Hamiltonian that *couples* the ancilla with the  $k$ 'th qubit. The latter can be written as

$$H_{[k]}^{AB} = \sum_{j_A, j_B=0}^3 h_{j_A j_B}^{[k]} \sigma_{j_A} \otimes \sigma_{j_B}, \quad (5.18)$$

where  $h_{j_A j_B}^{[k]}$  are real-valued coupling constants and  $\sigma_1, \sigma_2, \sigma_3$  are the usual Pauli sigma matrices, with  $\sigma_0 \equiv I$  the identity matrix. For the sake of simplicity we have considered the case  $D = 2$ , but similar generators can be found for  $D > 2$ .

Now, suppose that only a restricted set of unitaries are available. As an illustrative case, let the entangling Hamiltonian have the restricted form of the XY-model [93]

$$\tilde{H}_{[k]}^{AB} = h_1^{[k]} (\sigma_1 \otimes \sigma_1 + \sigma_2 \otimes \sigma_2), \quad (5.19)$$

containing a single nonzero contribution  $h_1^{[k]} \equiv h_{11}^{[k]} = h_{22}^{[k]}$ . Given an arbitrary MPS of the form of Eq. (5.16) with arbitrary  $A$ -matrices and the restricted Hamiltonian of Eq. (5.19), the aim is to find the optimal restricted unitary operations  $\tilde{U}_{[k]}^{AB} = e^{-i\tilde{H}_{[k]}^{AB}t/\hbar}$  that when

applied sequentially to an arbitrary initial state of the joint system  $|\Phi_I\rangle = |\varphi_I\rangle \otimes |\psi_I\rangle$ , yield a state of the form

$$|\tilde{\Psi}\rangle = \tilde{U}_{[n]}^{AB} \dots \tilde{U}_{[2]}^{AB} \tilde{U}_{[1]}^{AB} |\Phi_I\rangle, \quad (5.20)$$

that is “closest” to the target state of the form  $|\varphi_F\rangle \otimes |\psi\rangle$ , where  $|\varphi_F\rangle$  is arbitrary. Note that the action of each restricted unitary on initial state of qubit,  $\tilde{U}_{[k]}^{AB} |\psi_I^{[k]}\rangle$ , produces a restricted isometry of the form

$$\sum_{i_k, j_k, \alpha, \beta} \tilde{U}_{\alpha, \beta}^{i_k, j_k} |\alpha i_k\rangle \langle \beta j_k | \psi_I^{[k]}\rangle = \sum_{i_k, \alpha, \beta} \tilde{V}_{\alpha, \beta}^{i_k} |\alpha i_k\rangle \langle \beta |, \quad (5.21)$$

with the definition  $\tilde{V}_{\alpha, \beta}^{i_k} \equiv \sum_{j_k} \tilde{U}_{\alpha, \beta}^{i_k, j_k} \langle j_k | \psi_I^{[k]}\rangle$  for the resulting isometry  $\tilde{V}_{[k]}^{AB}$ . In the ideal case, when the fidelity reaches unity, the ancilla can be set to decouple unitarily in the last step. However, this will not be the case in general when the allowed ancilla-qubit unitaries are restricted. Thus, the optimization problem reads

$$\min_{|\tilde{\Psi}\rangle \in \tilde{H}_{[k]}} \| |\tilde{\Psi}\rangle - |\varphi_F\rangle \otimes |\psi\rangle \|^2, \quad (5.22)$$

involving a multivariable cost function in  $|\varphi_F\rangle$  and  $\{\bar{h}_1^{[n]}, \dots, \bar{h}_1^{[1]}\}$ , with  $\bar{h}_1^{[k]} = h_1^{[k]}t$ , as the *variational parameters*, which can be solved in an iterative procedure. We start by picking a particular unitary, say  $\tilde{U}_{[k]}^{AB}$ , and minimize the cost function in Eq. (5.22), varying over  $\bar{h}_1^{[k]}$  and regarding couplings of all the other unitaries as fixed. Then we move on to the neighboring unitary and optimize its coupling. When all unitaries have been optimized locally, we sweep back again and so forth until convergence. Each iteration of the local optimization procedure requires the calculation of the overlap of the states in the cost function of Eq. (5.22), which can be straightforwardly calculated in MPS representation as illustrated in Fig. 5.3 (with  $\mathcal{U}^A$  and  $\mathcal{U}^B$  set to  $\mathbf{1}$  there). Varying over the vector  $|\varphi_F\rangle$  and using the resulting optimal one, the cost function simplifies to  $2(1 - \|\langle \tilde{\Psi} | \psi \rangle\|)$ , suggesting the definition of the fidelity of the procedure as

$$\mathcal{F} \equiv \|\langle \tilde{\Psi} | \psi \rangle\|. \quad (5.23)$$

For the restricted entangling Hamiltonian of Eq. (5.19), the variational space is so small (only two parameters at each step), that the variational optimization procedure in general does not result in much overlap with the target state  $|\psi\rangle$ , as illustrated in the inset of Fig. 5.4 using the familiar  $|W\rangle_n$  state as target. However,  $\mathcal{F}$  can be improved by enlarging the variational space. For example, consider  $\tilde{U}^{AB}$  in Eq. (5.20) replaced by restricted unitaries of the form  $\mathcal{U}_{[k]}^A \tilde{U}_{[k]}^{AB}$ , where  $\mathcal{U}_{[k]}^A = e^{-iH_{[k]}^A t/\hbar}$  are arbitrary local ancilla unitaries of dimension  $D \times D$ . The new optimization problem can be treated in the same manner as the one described in Eq. (5.22), except that before optimizing each  $\tilde{U}^{AB}$ , we will also vary over the ancilla operation  $\mathcal{U}^A$ . In this way, we are able to produce the  $|W\rangle_n$ -state with almost perfect fidelity (e.g.  $1 - \mathcal{F} \approx 10^{-9}$  for  $n = 4$ ) as illustrated in Fig. 5.4. In both cases, the



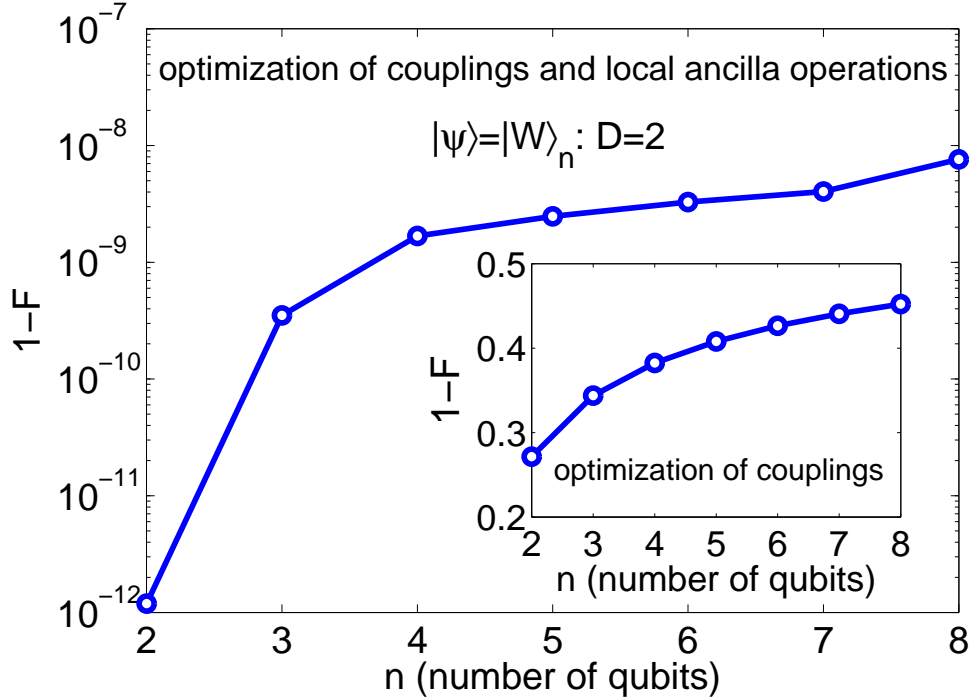


**Figure 5.4:** The deviation of the fidelity  $1 - \mathcal{F} = 1 - \|\langle \tilde{\Psi} | \psi \rangle\|$  as a function of the number  $n$  of qubits for the  $W$  state with  $D = 2$  when optimizing the couplings  $h_{j_A j_B}$  and the local ancilla unitaries  $\mathcal{U}_A$ , with initial qubit states all equal,  $|\psi_I^{[k]}\rangle = |0\rangle$ . The inset shows the case where only the couplings  $h_{j_A j_B}$  are being optimized.

smaller the number of qubits  $n$ , the larger the fidelity, which is a purely numerical issue due to the local optimization. Models requiring the entangling Hamiltonian of the  $XXZ$ -form

$$h_1^{[k]}(\sigma_1 \otimes \sigma_1 + \sigma_2 \otimes \sigma_2) + h_2^{[k]} \sigma_3 \otimes \sigma_3, \quad (5.24)$$

can be simulated in a similar manner.

Moreover, we have found strong numerical evidence that an *arbitrary* MPS with  $D = 2$  can be generated sequentially if the single-parameter restricted unitaries  $\tilde{U}^{AB}$  in Eq. (5.20) are augmented by arbitrary local unitaries for both ancilla and qubit space. The combined unitary employed was

$$\mathcal{U}_{[k]}^A \mathcal{U}_{[k]}^B \tilde{U}_{[k]}^{AB} \mathcal{U}_{[k]}^B, \quad (5.25)$$

where  $\mathcal{U}_{[k]}^B = e^{-iH_{[k]}^B t/\hbar}$  are arbitrary local qubit unitaries (see Fig. 5.3). We have considered, for this purpose, the generation of 100 randomly chosen MPS and have found that  $1 - \mathcal{F}$  remains below  $6 \times 10^{-13}$  up to  $n = 5$ . Note that the combined action of these unitaries includes (at most) 11 real independent parameters, which in practice can be reduced to 10, since varying a global phase has no effect. For the sake of the unrestricted ancilla unitaries

**Table 5.1:** Comparing the optimal couplings of our simulation  $h_1^{\text{sim}}$  to those used for experimental realization of  $W$  state  $h_1^{\text{exp}}$  in Ref. [61] for  $n = 5$ 

site index ( $k$ )	1	2	3	4	5
$((h_1^{\text{sim}}/h_1^{\text{exp}}) - 1) \times 10^5$	36.50	0.72	8.64	0.62	0.59

we exploit the standard  $Z$ - $Y$  decomposition of single-qubit operations given by [57]

$$\mathcal{U}^A = \begin{pmatrix} e^{i(\alpha-\beta/2-\delta/2)} \cos \frac{\gamma}{2} & -e^{i(\alpha-\beta/2+\delta/2)} \sin \frac{\gamma}{2} \\ e^{i(\alpha+\beta/2-\delta/2)} \sin \frac{\gamma}{2} & e^{i(\alpha+\beta/2+\delta/2)} \cos \frac{\gamma}{2} \end{pmatrix}, \quad (5.26)$$

with  $\alpha, \beta, \gamma$  and  $\delta$  being the independent real parameters. In contrast, the unrestricted unitaries  $U^{AB}$  involve 16 real independent parameters. Thus sequential generation of an arbitrary MPS with  $D = 2$ , can be achieved more economically than previously realized: a sufficient condition is the availability of the set of restricted two-qubit *isometries* specified above, instead of the availability of arbitrary two-qubit *unitaries* [31].

Recently, a lot of effort has been devoted to find minimal sets of one-qubit and two-qubit gates, and the minimal number of applications, to generate arbitrary two-qubit *unitaries* [94, 95, 96]. The existence of these universal sets is of central relevance in quantum computing, as it is known that two-qubit gates are universal for quantum computation [97, 98]. Our results suggest consideration of a class of problems involving a different paradigm: which are the universal sets of one-qubit and two-qubit gates that can generate arbitrary two-qubit *isometries*? What is the minimal number of applications and how does this compare to the quantum computing case? We have found numerically, for example, that some parameter-free fixed two-qubit gates (such as CNOT) plus three local unitaries are not *isometrically* universal, as they are not capable of generating an arbitrary state with  $\mathcal{F} = 1$ . The general solution associated with this new paradigm remains open.

As a final test of the proposed protocols, we applied our variational prescription to the sequential generation of  $W$  states in an ion chain. Following closely the recent experiment of Ref. [61], we targeted a  $W$  state with the entangling Hamiltonian of the form  $h_1(\sigma^+ \otimes \sigma^+ + \sigma^- \otimes \sigma^-)$ ,  $\sigma^+$  and  $\sigma^-$  being the usual raising and lowering Pauli operators, respectively, and the initial state  $|\psi_I\rangle = |1\rangle|0\rangle \dots |0\rangle$  used in experiment. The optimal couplings  $h_1^{\text{sim}}$  of the resulting converged variational MPS  $|\tilde{\Psi}\rangle$  (with  $1 - \mathcal{F} \approx 10^{-9}$  for  $n = 5$ ) turned out to agree very well with the two-qubit rotations  $h_1^{\text{exp}}$  used for the experiment of Ref. [61], as illustrated in Table 5.1.

## 5.4 Conclusions

In conclusion, we have developed protocols for an efficient sequential generation of entangled multiqubit states under realistic experimental constraints. We demonstrated how the MPS formalism allows to use optimization techniques for efficiently reducing the high demands on ancilla dimension (e.g. number of atomic levels). We showed even in a very

---

restricted scenario that access to only a limited class of source-qubit interactions is allowed, it is always possible to find the optimal source-qubit interaction that allows realization of the desired multiqubit state with an optimal fidelity. Most strikingly, we demonstrated any *arbitrary* multiqubit state with  $D = 2$  can be generated sequentially with a single-parameter entangling Hamiltonian of the  $XY$  form together with local ancilla and qubit unitaries.

Finally we stress that the proposed optimization methods are of wide applicability and will be of importance for any sequential physical setup. In particular, we can mention photonic qubits, atoms, ions, superconducting qubits, or quantum dots.



# Chapter 6

## Approximate sequential implementation of global operations

*The research reported in this chapter is currently being prepared for publication.*

The aim of this chapter is to quantitatively investigate the extent to which a given global operation can be approximated with subsequent application of local unitary operations. We employ the matrix-product operator (MPO) formalism to perform a suitably chosen variational optimization within the space of sequentially generated unitary operations. In other words, the aim is to see to what extent a global  $n$ -qubit unitary operation ( $n > 2$ ) can be approximated with subsequent application of two-qubit (ancilla-qubit) unitary operations.

The physical background and motivation is introduced in Section 6.1. In Section 6.2 the general methodology is presented and the numerical techniques to approach the problem is developed here. In Section 6.3 we consider the sequential generation of a global *isometry* and contrast the issue to that of a *unitary*. Eventually, a new consideration of the problem within a different metric is presented In Section 6.4.

### 6.1 Introduction

Engineering arbitrary global unitary gates is generically known to be “hard problem”, as it requires exponentially many gates to approximate [57]. However, in quantum computation it would be desirable to perform them efficiently. From this point of view, it will be then desirable to devise a protocol to implement the desired global unitary operation in a sequential unitary procedure in which an itinerant ancillary system (e.g. a  $D$ -level atom) interacts locally and only once with each qubit in a row. This type of quantum

factory of *operations* can be seen as a quantum Turing machine [99]. Note that this is different from the sequential generation of *states* which was studied in Chapter 5 where an entangled multiqubit state was targeted to be generated by sequential coupling of an ancilla to initially uncorrelated qubits. Here the main question will be whether it is possible to design a sequentially generated operation which has the same effect of the desired global unitary or not. The answer to this question turns out to be negative as proved by Lamata *et al* [39]. Nevertheless, in this chapter we provide optimization protocols that allow an optimal realization of a sequential version of the target global unitary with a certain fidelity. Our numerics confirm the “no-go” theorem and all theoretical claims of Ref. [39] and sheds light on the various aspects of this newly-developed line of research.

We first consider the map  $N \rightarrow N$  which was proved to be impossible to be implemented sequentially.

## 6.2 Sequential decomposition of global unitaries within Frobenius norm metric: The map $N \rightarrow N$

Let us assume that  $U_g$  is the target global unitary operator that we wish to implement and  $\tilde{U}$  is the sequentially decomposable unitary operator, implemented through a sequence of unitaries  $U_1, U_2, \dots, U_N$ , that is actually implemented in practice. The sequential implementation of a  $N$ -qubit global unitary  $U_g$  suggests that at a certain step, let's say  $k$ , the two-body unitary operation  $U_{ka}$  entangles the ancilla  $a$  and qubit  $k$  and leaves the other qubits unchanged, the global entangling unitary at step  $k$  being more explicitly  $U_{ka} \otimes \mathbb{1}_{2^{k-1}}$ . Let the resulting sequentially implemented global operation  $\tilde{U}$  with the aid of an ancilla  $a$  of dimension  $D$  be given by

$$\tilde{U} = U_{Na} \dots U_{2a} U_{1a} . \quad (6.1)$$

Expressing each local unitary in terms of a basis

$$U_{ka} = \sum_{i_k, j_k=1}^d \sum_{\alpha_k, \beta_k=1}^D U_{\alpha_k, \beta_k}^{i_k, j_k} |\alpha_k i_k\rangle \langle \beta_k j_k| , \quad (6.2)$$

the sequentially implemented  $\tilde{U}$  reads

$$\tilde{U} = \left( \sum_{i_N, j_N=1}^d \sum_{\alpha_N, \beta_N=1}^D U_{\alpha_N, \beta_N}^{i_N, j_N} |\alpha_N i_N\rangle \langle \beta_N j_N| \right) \dots \left( \sum_{i_1, j_1=1}^d \sum_{\alpha_1, \beta_1=1}^D U_{\alpha_1, \beta_1}^{i_1, j_1} |\alpha_1 i_1\rangle \langle \beta_1 j_1| \right) . \quad (6.3)$$

Summing over the ancillary indices ( $\alpha$  and  $\beta$ ) and defining  $\sum_{\alpha_k, \beta_k} U_{\alpha_k, \beta_k}^{i_k, j_k} |\alpha_k\rangle \langle \beta_k| \equiv U_{[k]}^{i_k, j_k}$  we arrive at

$$\tilde{U} = \sum_{i_N, \dots, i_1=1}^d \sum_{j_N, \dots, j_1=1}^d U_{[N]}^{i_N, j_N} \dots U_{[1]}^{i_1, j_1} |i_N\rangle \langle j_N| \otimes \dots \otimes |i_1\rangle \langle j_1| , \quad (6.4)$$

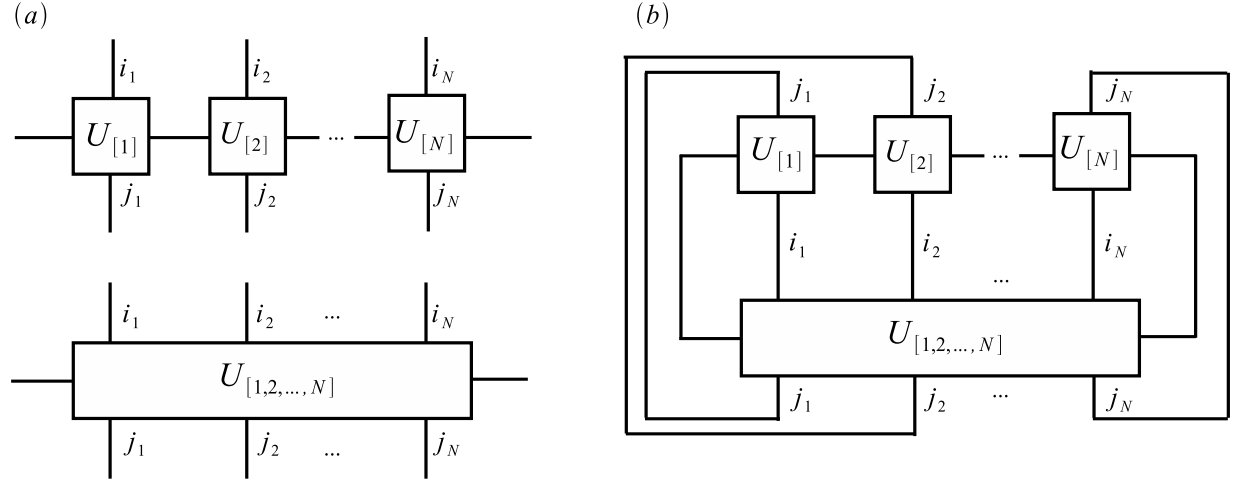


**Figure 6.1:** Graphical representation of (a) the sequentially implemented  $\tilde{U}$  contrasted to the global  $U_g$  and (b) the cost function Eq. (6.8) in MPO language.

as a matrix-product operator (MPO) [35, 36, 37, 38] already arisen in the calculation of finite-temperature density matrices [100]. On the other hand, the target global unitary itself expressed in terms of a basis reads

$$U_g = \sum_{i_N, \dots, i_1=1}^d \sum_{j_N, \dots, j_1=1}^d \sum_{\alpha, \beta=1}^D U_{\alpha, \beta}^{i_N, \dots, i_1, j_N, \dots, j_1} |\alpha i_N \dots i_1\rangle \langle \beta j_N \dots j_1|. \quad (6.5)$$

Summing again over the ancillary degrees of freedom yields

$$U_g = \sum_{i_N, \dots, i_1=1}^d \sum_{j_N, \dots, j_1=1}^d U_{[N \dots 21]}^{i_N, \dots, i_1, j_N, \dots, j_1} |i_N\rangle \langle j_N| \otimes \dots \otimes |i_1\rangle \langle j_1|. \quad (6.6)$$

In Fig. 6.1(a) the graphical representation of  $U_g$  (acting simultaneously on  $N$  qubits) in MPO language has been contrasted to that of sequentially implemented  $\tilde{U}$ . The aim is now to find the best possible sequential representation  $\tilde{U}$  of the global unitary operation  $U_g$  by minimizing the corresponding Frobenius distance [91] as the cost function <sup>1</sup>

$$\mathcal{C} = \|U_g - \tilde{U}\|_F^2 = 2D - 2\text{Re}\{\text{Tr}(U_g^\dagger \tilde{U})\}. \quad (6.7)$$

The cost function exploiting the MPO expressions of  $U_g$  and  $\tilde{U}$  reads

$$\mathcal{C} = 2D - 2\text{Re}\left\{\text{Tr}\left(\sum_{i_N, \dots, i_1} \sum_{j_N, \dots, j_1} \sum_{i'_N, \dots, i'_1} U_{[N \dots 21]}^{i_N, \dots, i_1, j'_N, \dots, j'_1} U_{[N]}^{i_N, j_N} \dots U_{[1]}^{i_1, j_1} \otimes |i_N \dots i_1\rangle \langle i'_N \dots i'_1|\right)\right\} \quad (6.8)$$

The calculation of the trace on the right hand side of the equation above finds a very simple form in MPO representation as depicted in Fig. 6.1(b). So the minimization problem can

<sup>1</sup>See Appendix E for some details on Frobenius norm.

be done very efficiently in an iterative method in which we fix all but one of the local operators, let's say the  $U_{[k]}$ , and minimize the cost function Eq. (6.8) by varying over the matrix elements of  $U_{[k]}$ . In the next iteration, the neighboring local operator is optimized, and once all the operators have been optimized locally, we sweep back again and so on until convergence.

In the case that ancilla is a qubit, i.e.  $D = 2$ , the local two-body unitaries may be expanded in terms of the complete basis of Pauli matrices

$$U_{[k]} = \exp\left(-i \sum_{j_1, j_2=0}^3 h_{j_1, j_2}^{[k]} \sigma_{j_1} \otimes \sigma_{j_2}\right), \quad (6.9)$$

where  $h_{j_1, j_2}^{[k]}$  are real-valued coefficients and  $\sigma_1, \sigma_2, \sigma_3$  are the usual Pauli sigma matrices, with  $\sigma_0 \equiv I$  the identity matrix. The minimization of the cost function Eq. (6.8) then amounts to finding the optimized coupling matrix  $h^{[k]}$  at each step of the iterative optimization. The fidelity of the sequential implementation of the global unitary  $U_g$  may be quantified as  $\mathcal{F} = 1 - \tilde{\mathcal{C}}$  where  $\tilde{\mathcal{C}}$  denotes the normalized converged cost function  $\mathcal{C}$  of Eq. (6.8) at the last sweep. The normalization is taken care of after dividing by the Frobenius norm of the involved operators.

### 6.2.1 Results for ancilla of dimension $D = 2$

We have applied the outlined procedure to some well-known global gates of quantum computing when the ancilla has the dimension  $D = 2$ , as illustrated in Table 6.1:<sup>2</sup>

For instance Controlled-NOT (CNOT) and controlled-phase (C-phase)(as two-qubit global unitary operations) can be implemented sequentially with fidelity 70.71%. The error 29.29% we associate with the existence of a “fidelity gap”, a strict theoretical red-line beyond which the corresponding gate can not be implemented sequentially. We may note also that those global gates that are equivalent up to local operations (e.g CNOT and C-phase where CNOT =  $(I \otimes H)$  C-phase  $(I \otimes H)$  and  $H$  being the Hadamard) give the same values of fidelity.

We now consider the scaling of the fidelity with the number of qubits  $n$ . For this purpose, we have considered a generalized CNOT, defined by  $G^n \equiv C^n$ -NOT depicted schematically in Fig. 6.2(a), and have observed the size of the gap tends to zero when  $n$  becomes large. Figure 6.3(a) illustrates this fact. This may suggest the *classical limit* in analogy to the quantum cloning in which the fidelity increases with the number of clones. This behavior may be also associated with the fact that the matrix representation of  $C^n$ -NOT becomes more and more similar to the identity matrix, as one increases  $n$ .

<sup>2</sup>We point out the C-phase (sometimes also called Controlled-Z) and the so-called “Controlled-i” (C-i, sometimes called C-phase) may be distinguished by their explicit matrix representations as

$$\text{C-phase} = \begin{pmatrix} 1 & 0 & 0 & 0 \\ 0 & 1 & 0 & 0 \\ 0 & 0 & 1 & 0 \\ 0 & 0 & 0 & -1 \end{pmatrix} \quad \text{and} \quad \text{C-i} = \begin{pmatrix} 1 & 0 & 0 & 0 \\ 0 & 1 & 0 & 0 \\ 0 & 0 & 1 & 0 \\ 0 & 0 & 0 & i \end{pmatrix}.$$



**Table 6.1:** The values of the Frobenius fidelity for sequential implementation of various global gates with ancilla of dimension  $D = 2$ .

global unitaries:	CNOT	C-phase	C-i	SWAP	$\sigma_1 \otimes \sigma_2$	Toffoli	Fredkin
Fidelity:	0.7071	0.7071	0.9239	0.50	1	0.75	0.75

However, we have also considered another  $n$ -qubit gate, defined by

$$L^n \equiv (C^1\text{-NOT} \otimes I_{D^{n-2}}) \dots (C^2\text{-NOT} \otimes I_D) C^{n-1}\text{-NOT}, \quad (6.10)$$

depicted schematically in Fig. 6.2(b). Unlike  $G^n \equiv C^n\text{-NOT}$ , the fidelity here saturates to a fixed value for large  $n$  (see Fig. 6.3(b)). We have investigated numerically that the matrix representations of  $L^n$  for all values of  $n > 2$  remain very similar to each other, which explains the observed behavior.

### 6.2.2 Results for ancilla of dimension $D = 4$

Similar techniques can be applied for the case  $D = 4$ , except that we should use a complete basis of  $4 \times 4$  matrices instead of the Pauli matrices which already did the job for  $D = 2$ . The local two-body unitaries may now be expanded by

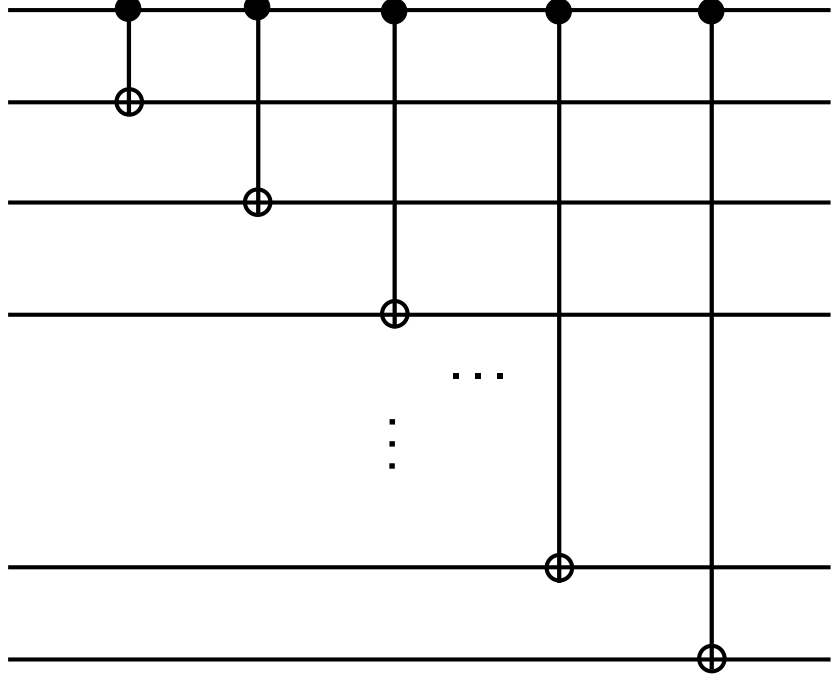
$$U_{[k]} = \exp\left(-i \sum_{j_1=0}^3 \sum_{j_2=0}^{15} h_{j_1, j_2}^{[k]} \sigma_{j_1} \otimes m_{j_2}\right), \quad (6.11)$$

where  $m$  denotes the set of linearly independent Hermitian matrices given by

$$\begin{pmatrix} 1 & 0 & 0 & 0 \\ 0 & 0 & 0 & 0 \\ 0 & 0 & 0 & 0 \\ 0 & 0 & 0 & 0 \end{pmatrix} \quad \begin{pmatrix} 0 & 0 & 0 & 0 \\ 0 & 1 & 0 & 0 \\ 0 & 0 & 0 & 0 \\ 0 & 0 & 0 & 0 \end{pmatrix} \quad \begin{pmatrix} 0 & 0 & 0 & 0 \\ 0 & 0 & 0 & 0 \\ 0 & 0 & 1 & 0 \\ 0 & 0 & 0 & 0 \end{pmatrix} \quad \begin{pmatrix} 0 & 0 & 0 & 0 \\ 0 & 0 & 0 & 0 \\ 0 & 0 & 0 & 0 \\ 0 & 0 & 0 & 1 \end{pmatrix}$$

$$\begin{pmatrix} 0 & 1 & 0 & 0 \\ 1 & 0 & 0 & 0 \\ 0 & 0 & 0 & 0 \\ 0 & 0 & 0 & 0 \end{pmatrix} \quad \begin{pmatrix} 0 & 0 & 1 & 0 \\ 0 & 0 & 0 & 0 \\ 1 & 0 & 0 & 0 \\ 0 & 0 & 0 & 0 \end{pmatrix} \quad \begin{pmatrix} 0 & 0 & 0 & 1 \\ 0 & 0 & 0 & 0 \\ 0 & 0 & 0 & 0 \\ 1 & 0 & 0 & 0 \end{pmatrix} \quad \begin{pmatrix} 0 & 0 & 0 & 0 \\ 0 & 0 & 1 & 0 \\ 0 & 1 & 0 & 0 \\ 0 & 0 & 0 & 0 \end{pmatrix}$$

$$\begin{pmatrix} 0 & 0 & 0 & 0 \\ 0 & 0 & 0 & 0 \\ 0 & 0 & 0 & 1 \\ 0 & 0 & 1 & 0 \end{pmatrix} \quad \begin{pmatrix} 0 & 0 & 0 & 0 \\ 0 & 0 & 0 & 1 \\ 0 & 0 & 0 & 0 \\ 0 & 1 & 0 & 0 \end{pmatrix} \quad \begin{pmatrix} 0 & -i & 0 & 0 \\ i & 0 & 0 & 0 \\ 0 & 0 & 0 & 0 \\ 0 & 0 & 0 & 0 \end{pmatrix} \quad \begin{pmatrix} 0 & 0 & -i & 0 \\ 0 & 0 & 0 & 0 \\ i & 0 & 0 & 0 \\ 0 & 0 & 0 & 0 \end{pmatrix}$$

(a)  $C^n$ -NOT(b)  $L^n$ 

**Figure 6.2:** Quantum logic gate representation of the two  $n$ -qubit global gates,  $C^n$ -NOT and  $L^n$ , studied here.

$$\begin{pmatrix} 0 & 0 & 0 & -i \\ 0 & 0 & 0 & 0 \\ 0 & 0 & 0 & 0 \\ i & 0 & 0 & 0 \end{pmatrix} \quad
 \begin{pmatrix} 0 & 0 & 0 & 0 \\ 0 & 0 & -i & 0 \\ 0 & i & 0 & 0 \\ 0 & 0 & 0 & 0 \end{pmatrix} \quad
 \begin{pmatrix} 0 & 0 & 0 & 0 \\ 0 & 0 & 0 & 0 \\ 0 & 0 & 0 & -i \\ 0 & 0 & i & 0 \end{pmatrix} \quad
 \begin{pmatrix} 0 & 0 & 0 & 0 \\ 0 & 0 & 0 & -i \\ 0 & 0 & 0 & 0 \\ 0 & i & 0 & 0 \end{pmatrix} \quad (6.12)$$

We have applied the same optimization techniques for the gates of Table 6.1 and have found out the values of the gap remain unchanged for  $D = 4$  compared to that of  $D = 2$ . Since  $D = 4$  is the maximum possible ancilla dimension for both  $N = 2$  and  $N = 3$  case (for  $N = 3$  any bipartite decomposition of the qubits yields a Schmidt rank identical to that of  $N = 2$ ), quite interestingly, we can conclude that the reported values of the gap are fundamental of the gates, irrespective of the ancilla dimension.

### 6.3 Sequential decomposition of global isometries within Frobenius norm metric: The map $M \rightarrow N$

Here we consider the possibility of sequential decomposition of a global isometry, i.e. the map  $M \rightarrow N$  when  $M < N$ . The aim here is to investigate this issue within the numerical

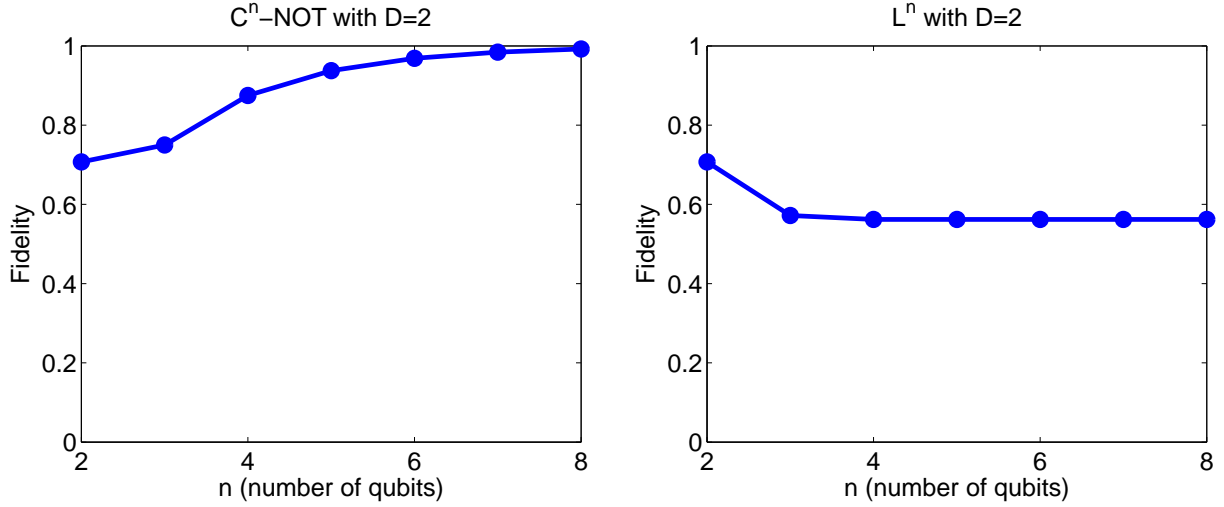


**Figure 6.3:** Scaling of the fidelity with  $n$  for two paradigmatic  $n$ -qubit gates studied here.

framework described in the last section.

### 6.3.1 The map $1 \rightarrow N$

We start with the sequential decomposition of the global isometry when  $M = 1$ , which was proved to be always possible if the ancilla dimension is large enough [101]. In this case, the corresponding index of only the first qubit for both global and sequential operations is free and the rest are contracted with some initial state of the qubits  $|\psi_I\rangle$ . We also consider here an initial state of the ancilla  $|\phi_I\rangle$ . The overlap pattern of Fig. 6.1 will be then modified as depicted in Fig. 6.4. We have applied our numerics for the case  $1 \rightarrow 3$  to Toffoli and Fredkin gates and the fidelity turns out to be 1 even with  $D = 2$ . However, we have also considered some randomly-generated  $1 \rightarrow 3$  isometries and have realized the fidelity remains below 1 with  $D = 2$  and this is not in contradiction with the claim of the last paragraph that the case  $1 \rightarrow N$  can always be done sequentially, since one may require higher ancilla dimension. When we tried  $D = 4$  for these gates, they gave the expected fidelity 1.

In particular, we have considered the  $1 \rightarrow 3$  isometry of the UQCM transformation in the context of the quantum cloning [101, 102] given by Eq. (3.29) of Ref. [103] which it has been proven to be sequentially decomposable with  $D = 4$ . Our numerics applied to this type of global isometry approves this theoretical claim: The so-called Hillery gate can be decomposed sequentially with fidelity 1 when  $D = 4$ . Quite interestingly,  $D = 2$  gives fidelity  $F = 0.9129$ , indicating this type of presumably highly entangling gate requires the maximum ancilla dimension to be implemented sequentially.

All in all, strong numerical confirmation of the theoretical result of Ref. [101].

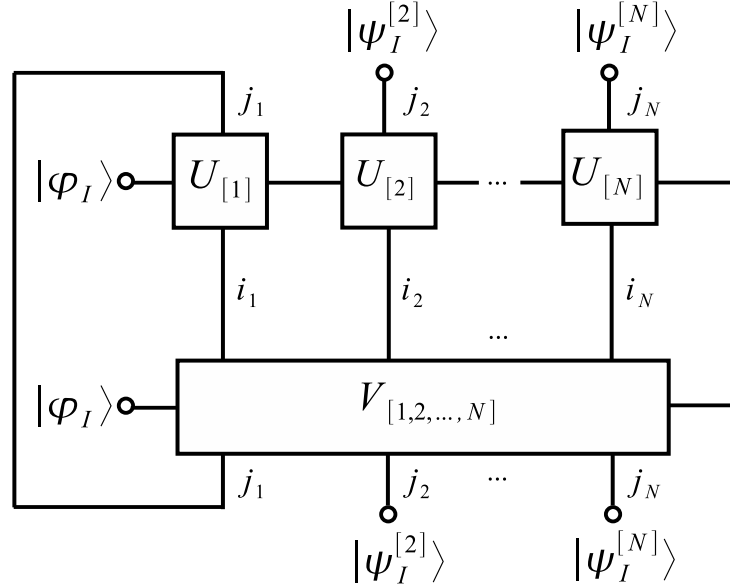


**Figure 6.4:** Graphical representation of the Frobenius overlap of a global isometry with the sequentially implemented one for the case  $1 \rightarrow N$

### 6.3.2 The map $M \rightarrow N$ when $1 < M < N$

This may be or may not be possible sequentially, as proved in Ref. [39]. The numerical framework remains the same as the case for  $1 \rightarrow N$  except that one would contract on some initial states of the qubits in Fig. 6.4 for the last  $N - M$  indices of the qubits on both global and sequential isometries. Our numerics imply that, for example, the map  $2 \rightarrow 3$  for Toffoli can be done with fidelity  $F = 1$  when  $D = 4$ , but some other randomly generated  $2 \rightarrow 3$  isometries do not admit such a sequential decomposition even with  $D = 4$ , in complete agreement with the theoretical claim of Ref. [39].

## 6.4 Sequential decomposition of global unitaries within $p$ -norm metric: The map $N \rightarrow N$

The aim is to study the sequential decomposition of unitaries in terms of the  $p$ -norm of operators instead of the Frobenius one.<sup>3</sup> The same formalism of the Frobenius metric holds also here except that we replace the  $F$ -norm by the  $p$ -norm ( $p = 2$ ) in the corresponding cost function of Eq. (6.7)

$$\mathcal{C} = \|U_g - \tilde{U}\|_2^2. \quad (6.13)$$

Obviously such a cost function may exceed 1. In order to bound the cost function (or equivalently the fidelity defined by  $F = 1 - \mathcal{C}$ ) between 0 and 1, we may make use of the

<sup>3</sup>See Appendix E for  $p$ -norm contrasted to Frobenius norm.

**Table 6.2:** The values of the  $p$ -norm fidelity for sequential implementation of various global gates with ancilla of dimension  $D = 2$  and for several runs of the program

global unitaries:	CNOT	C-phase	C-i	SWAP	Toffoli	Fredkin
F (run 1):	0.8533	0.8535	0.9609	0.5000	0.6578	0.5000
F (run 2):	0.8531	0.8533	0.9593	0.4999	0.6498	0.5000
F (run 3):	0.8519	0.8529	0.9589	0.4999	0.5241	0.4996
F (run 4):	0.8512	0.8526	0.9495	0.4999	0.5000	0.4890
F (run 5):	0.8507	0.8525	0.9481	0.4999	0.4122	0.4491

triangular inequality valid for the  $p$ -norm that [91]

$$\|A + B\|_2 \leq \|A\|_2 + \|B\|_2. \quad (6.14)$$

As a result, the normalized cost function  $\tilde{\mathcal{C}}$  reads

$$\tilde{\mathcal{C}} = \frac{\|U_g - \tilde{U}\|_2^2}{(\|U_g\|_2 + \|\tilde{U}\|_2)^2}, \quad (6.15)$$

which is guaranteed to change only between zero and 1. The same goes with the normalized fidelity  $\tilde{F} = 1 - \tilde{\mathcal{C}}$ . On the other hand, it is known that the 2-norm of any unitary matrix is 1. So the normalization factor in this case is always 4, irrespective of the dimension of the unitaries. Note that in the Frobenius norm case, the normalization factor used to grow with the dimension of the matrices, whereas in the 2-norm case it remains constant. In the case of the Frobenius metric, the trace product of the unitaries allowed for a very straightforward calculation of the norm within MPO language (see Eq. (6.8) and Fig. 6.1(b)). This ceases to be the case for the  $p$ -norm, since there is no such a trace product relation. The  $p$ -norm of a matrix  $A$  is defined by [91]

$$\|A\|_p = \max_{x \neq 0} \frac{\|Ax\|_p}{\|x\|_p}, \quad (6.16)$$

and in the specific case that  $p = 2$ , it finds the characterization  $\|A\|_2 = \rho(A^\dagger A)^{1/2}$ , where  $\rho$  denotes the spectral radius [104].<sup>4</sup> Alternatively, it is known that  $\|A\|_2 = \max_i(\sigma_i)$  where  $\sigma_i$  are the singular values of  $A$  [91]. It is clear from the definition that computing  $\|A\|_p$  is a nonlinear optimization problem over  $\mathbb{C}^n$ . The objective function is non-convex, so there will usually be local maxima having function values less than the global maximum  $\|A\|_p$  [104]. Up to now, no reliable numerical method has been developed that can guarantee to compute the global maximum at a reasonable cost. It is a well-known issue in numerical analysis that 2-norm computation is iterative and decidedly more complicated than the

<sup>4</sup>The spectral radius of a matrix  $A$  is defined by  $\rho \equiv \max_i(|\lambda_i|)$  where  $\lambda_i$ 's are the eigenvalues of  $A$ .

**Table 6.3:** The values of the Frobenius fidelity adopting the same normalization scheme as the 2-norm metric ( $D = 2$ )

global unitaries:	CNOT	C-phase	C-i	SWAP	$\sigma_1 \otimes \sigma_2$	Toffoli	Fredkin
Fidelity:	0.8536	0.8536	0.9619	0.75	1	0.875	0.875

computation of Frobenius norm, 1-norm or  $\infty$ -norm [91, 104]. Nevertheless, MATLAB offers a built-in routine (`norm`) that can calculate the 2-norm of the matrices. We have exploited this routine for the task of the optimization techniques of global unitaries in the same manner described for the Frobenius norm and here are the results:

For two-qubit global operations like CNOT we do observe a systematic behavior if we allow multiple runs of the program and the resulting data are quite close to each other. In that sense, the data for  $n = 2$  look fairly reliable, as illustrated in Table 6.2. It is interesting to see again that: CNOT and C-phase do give the same values of the fidelity, as expected. Controlled-i gives the highest fidelity among the two-qubits gates considered here and SWAP gives the lowest fidelity. The same happened in the F-norm case.

We should note, however, that in order to compare the values of the fidelity within 2-norm to that of F-norm, we should be careful to adopt the same normalization schemes for the corresponding cost functions, which is not yet the case. The normalization strategy adopted for F-norm inspired by the decomposition of the form

$$\mathcal{C}_F = \|U_g - \tilde{U}\|_F^2 = \|U_g\|_F^2 + \|\tilde{U}\|_F^2 - 2\text{Re}\{\text{Tr}(U_g^\dagger \tilde{U})\}, \quad (6.17)$$

where the normalization was taken care of by

$$\tilde{\mathcal{C}}_F = \frac{\mathcal{C}}{\|U_g\|_F^2 + \|\tilde{U}\|_F^2}, \quad (6.18)$$

whereas in the 2-norm case we made use of the triangular inequality of the norms to bound the fidelity between 0 and 1 (see Eq. (6.15)). If we employ the same strategy as the 2-norm for the normalization of F-norm, the values of the fidelities will be modified as illustrated in Table 6.3. We can see that in all cases the 2-norm fidelities remain smaller than the F-norm, in complete agreement with the fundamental inequality already known from linear algebra [91]

$$\|A\|_2 \leq \|A\|_F. \quad (6.19)$$

On the other hand, it is interesting to see except for SWAP, the values of the fidelities are very close to each other in both metrics.

Unlike the well-behaved numerics for  $n = 2$ , the statistics is not as well-behaved as the Frobenius metric for  $n > 2$  within the 2-norm metric. In the case of the F-norm, we enjoyed a very well-behaved and fast convergence of the fidelities to unique values for any

number of qubits, no local minima occurred. In the 2-norm case, for  $n > 2$  different runs of the program give different values of the fidelity, so the values of the fidelities are not uniquely determined. Table 6.2 illustrates this fact for Toffoli and Fredkin gates. Given the numerical challenges for computation of  $p$ -norm described before, it is absolutely no surprise to see this type of behavior in particular for large matrices which require more optimization iterations and consequently are more prone to running into local minima. Therefore, it seems numerically hard to obtain reliable results for  $n > 2$  within the 2-norm metric.

## 6.5 Conclusions

In conclusion, we have developed theoretical and numerical protocols for an efficient sequential decomposition of global multiqubit operations. We demonstrated how the newly developed method of matrix-product operator (MPO) can be exploited as a flexible numerical framework to study the associated optimization problems. Our numerics confirm the “no-go” theorem and all theoretical claims of Ref. [39] and offers efficient optimization techniques for the sequential realization of any arbitrary global multiqubit operation with an optimal fidelity.

We believe results presented in this chapter will be particularly useful for future implementation of quantum networks, quantum error correction, quantum cryptographic tasks and realted physical setups.





Part III

Appendix



# Appendix A

## Orthonormalization of $B$ -matrices of unfolded Wilson chain

To keep the notation simple, in this appendix we shall imagine the sites of the unfolded Wilson chain to be stretched along a line running from left to right, enumerated by an index  $k$  running from 1 for site  $N\downarrow$  to  $K = 2(N + 1)$  for site  $N\uparrow$ . Correspondingly, matrix-product states will generically be written as  $|\Psi\rangle = \sum_{\{\sigma^K\}} |\sigma^K\rangle (\prod_{k=1}^K B^{[\sigma_k]})$ , with matrix elements  $B_{\nu\eta}^{[\sigma_k]}$ .

It is convenient to ensure that every  $B$ -matrix in a matrix-product state satisfies one of the following two orthonormality conditions:

$$\sum_{\sigma_k} B^{[\sigma_k]\dagger} B^{[\sigma_k]} = \mathbf{1} , \quad (\text{A.1a})$$

$$\sum_{\sigma_k} B^{[\sigma_k]} B^{[\sigma_k]\dagger} = \mathbf{1} . \quad (\text{A.1b})$$

In particular, if *all*  $B$ -matrices satisfy either the first or the second of these conditions, the corresponding matrix-product state is automatically normalized:

$$\langle \Psi | \Psi \rangle = \sum_{\{\sigma^K\}} (B_{1\nu'}^{[\sigma_K]\dagger} \dots B_{\eta'1}^{[\sigma_1]\dagger}) (B_{1\eta}^{[\sigma_1]} \dots B_{\nu 1}^{[\sigma_K]}) = 1 . \quad (\text{A.2})$$

This follows by iteratively applying Eq. (A.1). To start the iteration, note that for matrices at the beginning or end of the chain, where one of the matrix indices is a dummy index with only a single value, Eqs. (A.1a) or (A.1b) imply  $\sum_{\sigma_1} B_{\eta'1}^{[\sigma_1]\dagger} B_{1\eta}^{[\sigma_1]} = \delta_{\eta'\eta}$  or  $\sum_{\sigma_K} B_{\nu 1}^{[\sigma_K]} B_{1\nu'}^{[\sigma_K]\dagger} = \delta_{\nu\nu'}$ , respectively. In the NRG approach, all  $A$ -matrices naturally satisfy Eq. (A.1a) [cf. Eq. (4.6)].

In the VMPS approach, it is convenient to ensure that during variational optimization sweeps, Eq. (A.1a) holds for all matrices to the left of the site, say  $k$ , currently being updated, and Eq. (A.1b) for all matrices to its right. Thus, after optimizing the set of matrices  $B^{[\sigma_k]}$  at site  $k$ , this set should be orthonormalized before moving on to the next

site, such that it satisfies Eq. (A.1a) when sweeping from left to right (or Eq. (A.1b) when sweeping from right to left). This can be achieved using singular value decomposition [cf. Eq. (4.18)]: Arrange the matrix elements of the set of matrices  $B^{[\sigma_k]}$  into a rectangular matrix carrying only two labels, with matrix elements  $\mathcal{B}_{\bar{\nu}\eta} = B_{\nu\eta}^{[\sigma_k]}$  (or  $\mathcal{B}_{\nu\bar{\eta}} = B_{\nu\eta}^{[\sigma_k]}$ ), by introducing a composite index  $\bar{\nu} = (\sigma_k, \nu)$  (or  $\bar{\eta} = (\sigma_k, \eta)$ ). Using singular value decomposition [Eq. (4.18)], write this new matrix as  $\mathcal{B} = \mathcal{U}\mathcal{S}\mathcal{V}^\dagger$ . Then rewrite the matrix-product of two neighboring  $B$ -matrices as  $B^{[\sigma_k]}B^{[\sigma_{k+1}]} = \tilde{B}^{[\sigma_k]}\tilde{B}^{[\sigma_{k+1}]}$  (or  $B^{[\sigma_{k-1}]}B^{[\sigma_k]} = \tilde{B}^{[\sigma_{k-1}]}B^{[\sigma_k]}$ ), where the new matrices  $\tilde{B}$  are defined by

$$\tilde{B}_{\nu\gamma}^{[\sigma_k]} = \mathcal{U}_{\bar{\nu}\gamma}, \quad \tilde{B}_{\gamma\delta}^{[\sigma_{k+1}]} = (\mathcal{S}\mathcal{V}^\dagger B^{[\sigma_{k+1}]})_{\gamma\delta}, \quad (\text{A.3})$$

$$\text{(or } \tilde{B}_{\delta\eta}^{[\sigma_k]} = \mathcal{V}_{\delta\bar{\eta}}^\dagger, \quad \tilde{B}_{\gamma\delta}^{[\sigma_{k-1}]} = (B^{[\sigma_{k-1}]} \mathcal{U}\mathcal{S})_{\gamma\delta} \text{)}. \quad (\text{A.4})$$

The property  $\mathcal{U}^\dagger\mathcal{U} = \mathbb{1}$  (or  $\mathcal{V}^\dagger\mathcal{V} = \mathbb{1}$ ) ensures that the new set of matrices  $\tilde{B}^{[\sigma_k]}$  at site  $k$  is orthonormal according to Eq. (A.1a) (or Eq. (A.1b)), as desired. Now proceed to the next site to the right (or left) and orthonormalize  $\tilde{B}^{[\sigma_{k+1}]}$  (or  $\tilde{B}^{[\sigma_{k-1}]}$ ) in the same manner, etc.

The above procedure can be used to orthonormalize the matrices of a randomly generated matrix-product state before starting VMPS sweeping. Likewise, during VMPS sweeping, each newly optimized matrix can be orthonormalized in the above fashion before moving on to optimize the matrix of the next site.

# Appendix B

## Refolding

This appendix describes how to refold an unfolded matrix-product state of the form

$$|\Psi_{\nu\eta}^n\rangle_{\text{u}} = \sum_{\{\sigma^N\}} |\sigma^n\rangle (B^{[\sigma_{n\downarrow}]} \dots B^{[\sigma_{0\downarrow}]} B^{[\sigma_{0\uparrow}]} \dots B^{[\sigma_{n\uparrow}]})_{\nu\eta}, \quad (\text{B.1})$$

shown schematically by sites  $n\downarrow$  to  $n\uparrow$  of Fig. 4.2(c). Its two indices will be treated as a composite index  $\beta = (\nu, \eta)$  below. The variational matrix-product state  $|\Psi^N\rangle_{\text{u}}$  of Eq. (4.16) discussed in the main text is a special case of Eq. (B.1), with  $n = N$  and  $\nu = \eta = 1$ . The goal is to express Eq. (B.1) as a linear combination,

$$|\Psi_{\nu\eta}^n\rangle_{\text{u}} = \sum_{\alpha} |\Psi_{\alpha}^n\rangle_{\text{r}} C_{\alpha\beta}^n, \quad (\text{B.2})$$

( $\beta = (\nu, \eta)$  is a composite index) of an orthonormal set of “refolded basis states” of the form of Eq. (4.22),

$$|\Psi_{\alpha}^n\rangle_{\text{r}} = \sum_{\{\sigma^n\}} |\sigma^n\rangle (B^{[\sigma_0]} B^{[\sigma_1]} \dots B^{[\sigma_n]})_{1\alpha}, \quad (\text{B.3})$$

shown schematically by sites 0 to  $n$  of Fig. 4.2(a). To this end, we proceed iteratively in  $n$ . We use singular value decomposition to iteratively merge, for every pair of sites  $n\downarrow$  and  $n\uparrow$  of the unfolded chain, the matrices  $B_{\nu\nu'}^{[\sigma_{n\downarrow}]}$  and  $B_{\eta'\eta}^{[\sigma_{n\uparrow}]}$  into a new set of matrices  $B_{\alpha'\alpha}^{[\sigma_n]}$  for site  $n$  of the refolded chain, thereby trading the indices  $\sigma_{n\downarrow}, \sigma_{n\uparrow}$  and  $\nu\eta$  of Fig. 4.2(c) for the indices  $\sigma_n$  and  $\alpha$  of Fig. 4.2(a). This is to be done in such a way that the matrices  $B^{[\sigma_n]}$  are orthonormal in the sense of Eq. (4.6), and that for the first few sites their dimensions increase in a way analogous to those of the  $A^{[\sigma_n]}$  matrices of NRG, starting from  $1 \times d$  at site  $n = 0$ .

For the first iteration step, start with  $n = 0$ , make a singular value decomposition of the matrix-product

$$(B^{[\sigma_{0\downarrow}]} B^{[\sigma_{0\uparrow}]})_{\nu'\eta'} = (\mathcal{U}^0 \mathcal{S}^0 \mathcal{V}^{0\dagger})_{\sigma_0\beta'}, \quad (\text{B.4})$$

with  $\beta' = (\nu', \eta')$ , and use  $\mathcal{U}^0$  to define a new set of  $d$  matrices  $B^{[\sigma_0]}$  for site 0 of the refolded chain, with matrix elements  $B_{1\alpha'}^{[\sigma_0]} = \mathcal{U}_{\sigma_0\alpha'}^0$ . The  $B^{[\sigma_0]}$  have dimensions  $1 \times d$  (the dummy first index has just one value), and are by construction orthonormal in the sense of Eq. (4.6), since  $\mathcal{U}^{0\dagger}\mathcal{U}^0 = \mathbb{1}$ . Upon inserting Eq. (B.4) into Eq. (B.1), the factor  $\mathcal{U}^0$  produces the first matrix factor  $B^{[\sigma_0]}$  in the refolded state (B.3), thus completing the first iteration step. For the second iteration step, contract the factors  $\mathcal{S}^0\mathcal{V}^{0\dagger}$  with the factors  $B^{[\sigma_{1\downarrow}]}$  and  $B^{[\sigma_{1\uparrow}]}$  in Eq. (B.1), factorize the result as  $\mathcal{U}^1\mathcal{S}^1\mathcal{V}^{1\dagger}$  and use  $\mathcal{U}^1$  to construct new matrices  $B^{[\sigma_1]}$  for site 1 of the refolded chain, etc. To be explicit, for general  $n$ , make a singular value decomposition of the matrix-product

$$\sum_{\nu'\eta'} B_{\nu\nu'}^{[\sigma_{n\downarrow}]} (\mathcal{S}^{(n-1)}\mathcal{V}^{(n-1)\dagger})_{\alpha'\beta'} B_{\eta'\eta}^{[\sigma_{n\uparrow}]} = (\mathcal{U}^n\mathcal{S}^n\mathcal{V}^{n\dagger})_{\bar{\alpha}\beta}, \quad (\text{B.5})$$

with composite indices  $\bar{\alpha} = (\sigma_n, \alpha')$ ,  $\sigma_n = (\sigma_{n\downarrow}, \sigma_{n\uparrow})$ ,  $\beta = (\nu, \eta)$  and  $\beta' = (\nu', \eta')$ . Then use  $\mathcal{U}^n$  to define a new set of orthonormal matrices  $B^{[\sigma_n]}$  for site  $n$  of the refolded chain, with matrix elements  $B_{\alpha'\alpha}^{[\sigma_n]} = \mathcal{U}_{\bar{\alpha}\alpha}^n$ . In this way one readily establishes that  $|\Psi_{\nu\eta}^n\rangle_{\text{u}}$  can be written in the form of Eq. (B.2), with  $C_{\alpha\beta}^n = (\mathcal{S}^n\mathcal{V}^{n\dagger})_{\alpha\beta}$ .

The dimensions of the matrices  $B^{[\sigma_n]}$  initially grow by a factor of  $d$  with each iteration step, until their dimensions are restricted by the number of possible values of the composite index  $\beta$ , namely  $D_n'^2$ , with  $D_n'$  given by Eq. (4.17). Thus, the  $B^{[\sigma_n]}$  have dimensions  $D_n^r \times D_{n+1}^r$ , with  $D_n^r = \min(d^n, D_{n-1}'^2)$ , which leads to Eq. (4.21).

# Appendix C

## Calculation of the effective refolded Hamiltonian within the MPS formalism

In this appendix we provide the details of how the effective Hamiltonian of the refolded Wilson chain ( $\mathcal{H}_r^n$  defined in Eq. (4.23)) can be efficiently obtained within the MPS formalism in a recursive manner. We first note that the Jordan-Wigner transformed SIAM Eq. (4.2) for the chain of length  $N$  can be written as [79, 10]

$$\mathcal{H}_N = \sum_{k=1}^N \vec{g}_k \cdot \vec{\sigma}_k + \sum_{k=1}^{N-1} \vec{f}_k \cdot (\vec{\sigma}_k \otimes \vec{\sigma}_{k+1}), \quad (\text{C.1})$$

where  $\vec{f}_k$  and  $\vec{g}_k$  denote the hopping terms and on-site interactions at site  $k$ , respectively, and  $\vec{\sigma}_k \equiv (\sigma_x^k, \sigma_y^k, \sigma_z^k)$  with  $\sigma_x$ ,  $\sigma_y$  and  $\sigma_z$  being the usual Pauli matrices. The couplings structure is depicted schematically in Fig. C.1. Here the original fermionic model has been mapped onto a spin Hamiltonian where use been made of the relation between the Pauli matrices and the fermionic creation/annihilation operators

$$\sigma_x = c + c^\dagger \quad \sigma_y = i(c - c^\dagger) \quad , \quad (\text{C.2})$$

We may now note that the Hamiltonian at site  $k$  of the Wilson chain may be splitted into three parts (as depicted in Fig. C.2)

$$\mathcal{H}_L^k = \mathcal{H}_L^{k-1} + \mathcal{H}_{k-1,k} + \mathcal{H}_k, \quad (\text{C.3})$$

where  $\mathcal{H}_L^{k-1}$  is the Hamiltonian at site  $k-1$ ,  $\mathcal{H}_k$  denotes the local contribution from the current site  $k$ , and  $\mathcal{H}_{k-1,k}$  are those terms of the Hamiltonian that couple site  $k-1$  to site  $k$ .

Having refolded the Wilson chain, we now begin from left of the refolded chain by constructing the effective Hamiltonian for site  $k=1$ . Obviously,  $\mathcal{H}_L^{k-1} = \mathcal{H}_{k-1,k} = 0$  for

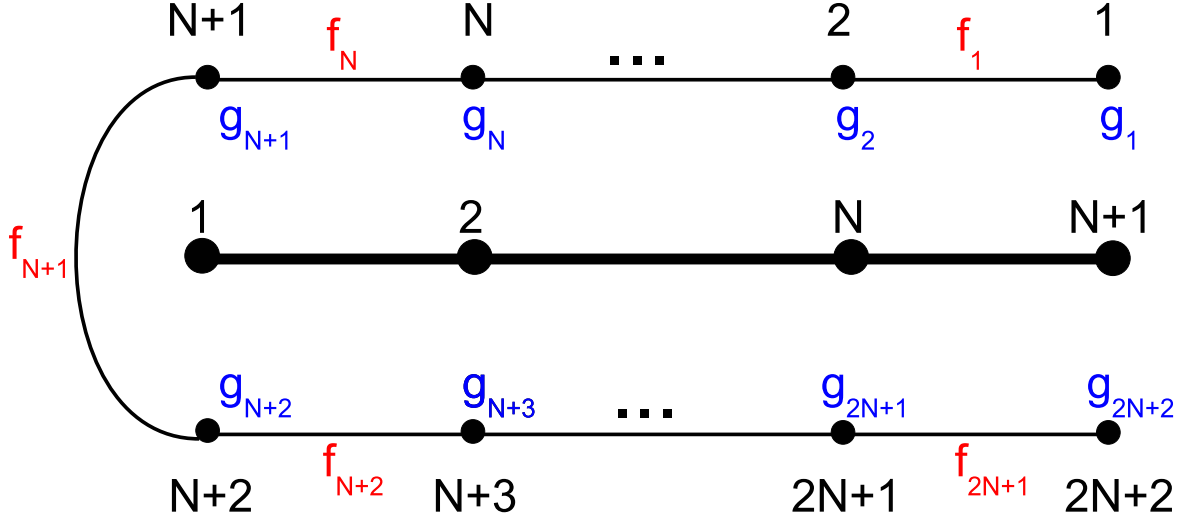


**Figure C.1:** Couplings structure of the unfolded and refolded Wilson chain

$k = 1$ . So the only non-vanishing term will be the local contribution  $\mathcal{H}_1$ , for SIAM given by

$$\mathcal{H}_1 = \sum_{p=1}^3 g(N+1, p) \sigma_{\uparrow p}^{N+1} + g(N+2, p) \sigma_{\downarrow p}^{N+2} + f(N+1, p) \sigma_{\uparrow p}^{N+1} \sigma_{\downarrow p}^{N+2}, \quad (\text{C.4})$$

The aim is now to calculate the matrix elements of  $\mathcal{H}_1$  in the basis of the current site

$$(\mathcal{H}_r^1)_{\alpha\beta} = {}_r \langle \Psi_\alpha^1 | \mathcal{H}_1 | \Psi_\beta^1 \rangle_r, \quad (\text{C.5})$$

To keep the notation simple, we drop the subscript  $r$  for refolded chain throughout this appendix and use the symbols  $l$  and  $r$  for the left and right site of the chain upon going to the next iteration. In the MPS language the basis of the current site  $|r\rangle$  (the one to the right) can be constructed from that of the previous one  $|l\rangle$  (the one to the left) as

$$|r'\rangle = \sum_{l', \sigma'_\uparrow, \sigma'_\downarrow} B_{r'l'}^{[\sigma'_\uparrow, \sigma'_\downarrow]} |l' \sigma'_\uparrow \sigma'_\downarrow\rangle, \quad (\text{C.6})$$

For the sake of simplicity, we split  $x\{1\}$  to two parts  $I_g$  and  $I_f$  containing the contributions from  $g$  and  $f$  couplings, respectively, i.e.  $x\{1\} \equiv I_g + I_f$ .  $I_g$  then reads

$$I_g = \sum_{l, \sigma_\uparrow, \sigma_\downarrow} \sum_{l', \sigma'_\uparrow, \sigma'_\downarrow} \sum_{p=1}^3 B_{rl}^{[\sigma_\uparrow, \sigma_\downarrow] \dagger} B_{r'l'}^{[\sigma'_\uparrow, \sigma'_\downarrow]} \left( g(N+1, p) \langle l|l'\rangle \langle \sigma_\downarrow | \sigma'_\downarrow \rangle \langle \sigma_\uparrow | \sigma_{\uparrow p}^{N+1} | \sigma'_\uparrow \rangle \right. \\ \left. + g(N+2, p) \langle l|l'\rangle \langle \sigma_\uparrow | \sigma'_\uparrow \rangle \langle \sigma_\downarrow | \sigma_{\downarrow p}^{N+2} | \sigma'_\downarrow \rangle \right), \quad (\text{C.7})$$



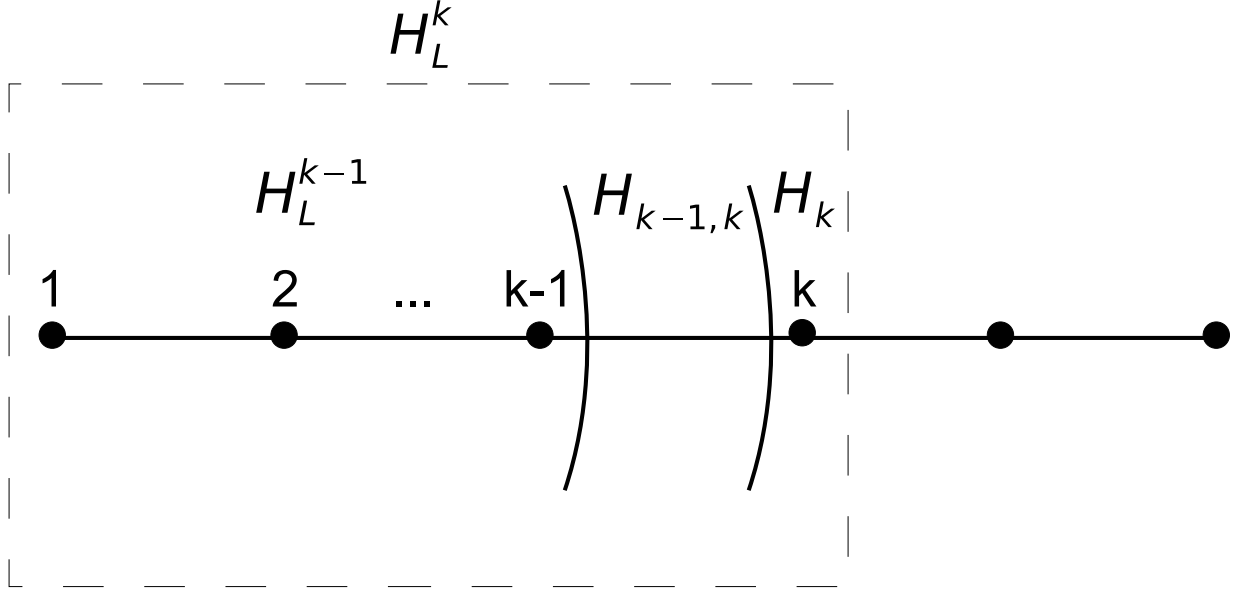


**Figure C.2:** Hamiltonian at site  $k$  splitted into the left, local and the coupling between left and local part.

where use has been made of the fact that each  $\sigma$  operator only acts on its own basis  $|\sigma\rangle$ , e.g.

$$\langle \sigma_{\uparrow} \sigma_{\downarrow} | \sigma_{\uparrow p}^{N+1} | \sigma'_{\uparrow} \sigma'_{\downarrow} \rangle = \langle \sigma_{\uparrow} \sigma_{\downarrow} | \sigma_{\uparrow p}^{N+1} \otimes \mathbb{1}_{\downarrow p}^{N+1} | \sigma'_{\uparrow} \sigma'_{\downarrow} \rangle = \langle \sigma_{\uparrow} | \sigma_{\uparrow p}^{N+1} | \sigma'_{\uparrow} \rangle \langle \sigma_{\downarrow} | \sigma'_{\downarrow} \rangle, \quad (\text{C.8})$$

$I_g$  then reads

$$\begin{aligned} I_g &= \sum_{l, \sigma_{\uparrow}, \sigma_{\downarrow}, \sigma'_{\uparrow}} \sum_{p=1}^3 B_{rl}^{[\sigma_{\uparrow}, \sigma_{\downarrow}] \dagger} B_{r'l}^{[\sigma'_{\uparrow}, \sigma'_{\downarrow}]} g(N+1, p) (sx\{p\})_{\sigma_{\uparrow}, \sigma'_{\uparrow}} \\ &+ \sum_{l, \sigma_{\uparrow}, \sigma_{\downarrow}, \sigma'_{\downarrow}} \sum_{p=1}^3 B_{rl}^{[\sigma_{\uparrow}, \sigma_{\downarrow}] \dagger} B_{r'l}^{[\sigma_{\uparrow}, \sigma'_{\downarrow}]} g(N+2, p) (sx\{p\})_{\sigma_{\downarrow}, \sigma'_{\downarrow}} \end{aligned} \quad (\text{C.9})$$

where use has been made of the facts  $\langle l | l' \rangle = \delta_{ll'}$  and  $\langle \sigma | \sigma' \rangle = \delta_{\sigma\sigma'}$  and we have defined  $\langle \sigma_{\uparrow} | \sigma_{\uparrow p}^{N+1} | \sigma'_{\uparrow} \rangle \equiv (sx\{p\})_{\sigma_{\uparrow}, \sigma'_{\uparrow}}$  and  $\langle \sigma_{\downarrow} | \sigma_{\downarrow p}^{N+2} | \sigma'_{\downarrow} \rangle \equiv (sx\{p\})_{\sigma_{\downarrow}, \sigma'_{\downarrow}}$

The contribution  $I_g$  comes from the coupling between spin-up and down of the impurity  $f(N+1)$ , so  $I_f$  for  $k=1$  takes the form

$$I_f = \langle r | \sum_{p=1}^3 f(N+1, p) \sigma_{\uparrow p}^{N+1} \sigma_{\downarrow p}^{N+2} | r' \rangle, \quad (\text{C.10})$$

In a similar vein,  $I_f$  simplifies to

$$I_f = \sum_{l, \sigma_{\uparrow}, \sigma_{\downarrow}} \sum_{\sigma'_{\uparrow}, \sigma'_{\downarrow}} \sum_{p=1}^3 B_{rl}^{[\sigma_{\uparrow}, \sigma_{\downarrow}] \dagger} B_{r'l}^{[\sigma'_{\uparrow}, \sigma'_{\downarrow}]} f(N+1, p) (sx\{p\})_{\sigma_{\uparrow}, \sigma'_{\uparrow}} (sx\{p\})_{\sigma_{\downarrow}, \sigma'_{\downarrow}}, \quad (\text{C.11})$$

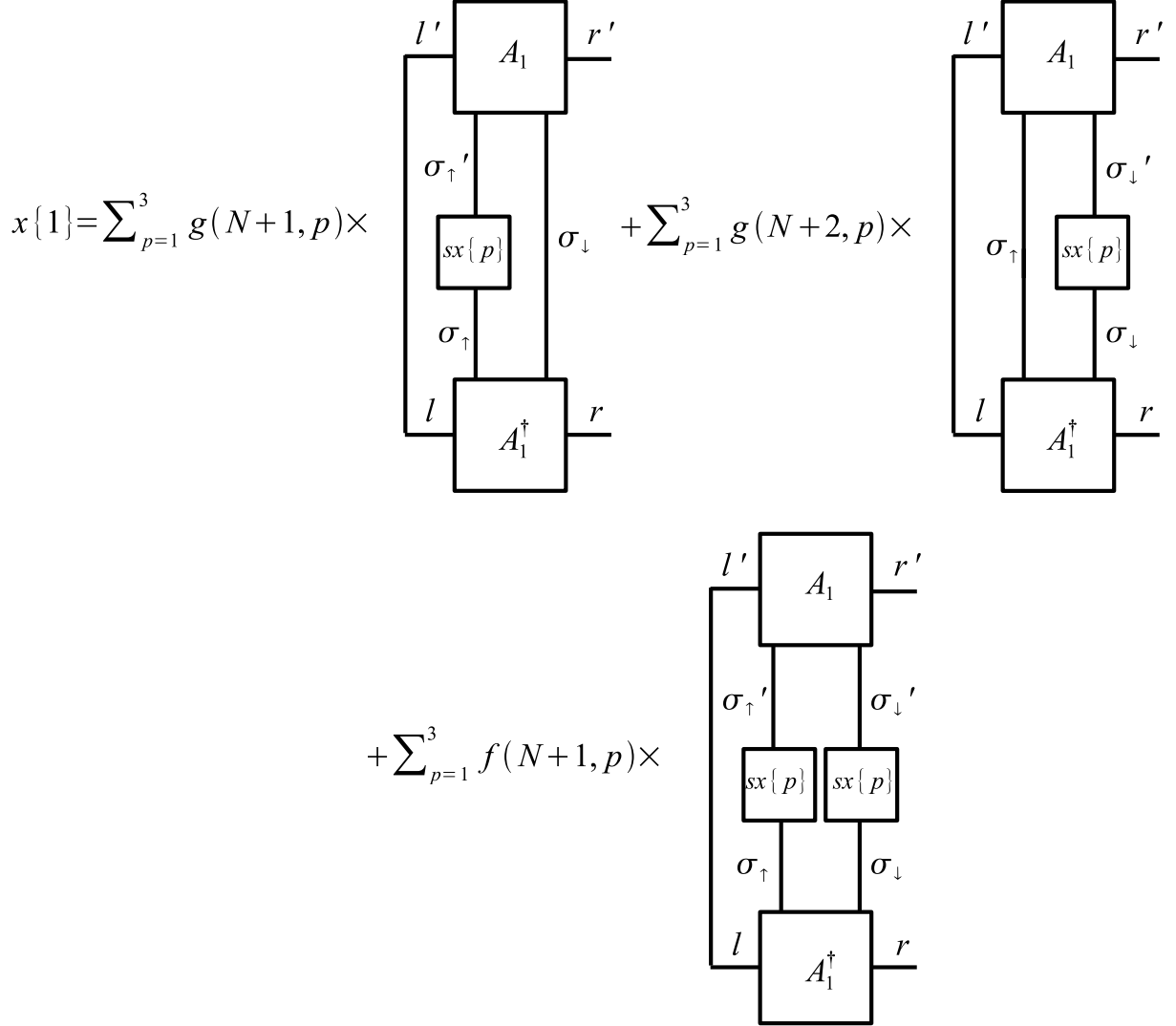


**Figure C.3:** Graphical MPS representation of calculating the effective refolded Hamiltonian for the site  $k = 1$ .

Putting altogether,  $x\{1\}$  can be graphically represented in MPS language as in Fig. C.3.

In order to go to the next site, we still need to calculate the matrix elements of  $\sigma_{\uparrow p}^{N+1}$  and  $\sigma_{\downarrow p}^{N+2}$  in the current basis of site  $k = 1$

$$\left( Sx_{\uparrow}\{1\}\{p\} \right)_{rr'} \equiv \langle r | \sigma_{\uparrow p}^{N+1} | r' \rangle, \quad (\text{C.12})$$

which can be simplified as

$$\left( Sx_{\uparrow}\{1\}\{p\} \right)_{rr'} = \sum_{l, \sigma_{\uparrow}, \sigma_{\downarrow}} \sum_{\sigma_{\uparrow}'} B_{rl}^{[\sigma_{\uparrow}\sigma_{\downarrow}\dagger]} B_{r'l}^{[\sigma_{\uparrow}'\sigma_{\downarrow}]} (sx\{p\})_{\sigma_{\uparrow}\sigma_{\uparrow}'}, \quad (\text{C.13})$$

Similarly, for the spin-down part we will have

$$\left( Sx_{\downarrow}\{1\}\{p\} \right)_{rr'} \equiv \langle r | \sigma_{\downarrow p}^{N+2} | r' \rangle = \sum_{l, \sigma_{\uparrow}, \sigma_{\downarrow}} \sum_{\sigma'_{\downarrow}} B_{rl}^{[\sigma_{\uparrow}\sigma_{\downarrow}] \dagger} B_{r'l}^{[\sigma'_{\uparrow}\sigma'_{\downarrow}]} (sx\{p\})_{\sigma_{\downarrow}\sigma'_{\downarrow}}, \quad (\text{C.14})$$

which provides us with all the data needed to go to the next site.

At site  $k = 2$  of the refolded chain, the recursive form of the Hamiltonian reads

$$\mathcal{H}_L^2 = \mathcal{H}_L^1 + \mathcal{H}_{1,2} + \mathcal{H}_2. \quad (\text{C.15})$$

So the effective Hamiltonian  $x\{2\}$  entails three contributions denoted by

$$(x\{2\})_{rr'} \equiv \langle r | \mathcal{H}_L^2 | r' \rangle = I_1 + I_2 + I_3. \quad (\text{C.16})$$

Note here that the right basis  $r$  is now at site  $k = 2$  and the left basis is the previous site  $k = 1$ . We now calculate each part separately. For the first contribution  $I_1$  we have

$$I_1 = \langle r | \mathcal{H}_L^1 | r' \rangle = \sum_{l, \sigma_{\uparrow}, \sigma_{\downarrow}} \sum_{l'} B_{rl}^{[\sigma_{\uparrow}\sigma_{\downarrow}] \dagger} B_{r'l'}^{[\sigma'_{\uparrow}\sigma'_{\downarrow}]} (x\{1\})_{ll'}. \quad (\text{C.17})$$

where we have made the identification  $\langle l | \mathcal{H}_L^1 | l' \rangle = (x\{1\})_{ll'}$ .

For the second contribution to the effective Hamiltonian at site  $k = 2$  we have

$$I_2 = \langle r | \mathcal{H}_{1,2} | r' \rangle = \langle r | \sum_p f(N, p) \sigma_{\uparrow p}^{N+1} \sigma_{\uparrow p}^N + \sum_p f(N + 2, p) \sigma_{\uparrow p}^{N+2} \sigma_{\downarrow p}^{N+3} | r' \rangle. \quad (\text{C.18})$$

Once again, plugging in the MPS recursive relation for the current basis of Eq. (C.6) yields

$$I_2 = \sum_{l, \sigma_{\uparrow}, \sigma_{\downarrow}} \sum_{l', \sigma'_{\uparrow}, \sigma'_{\downarrow}} \sum_{p=1}^3 B_{rl}^{[\sigma_{\uparrow}\sigma_{\downarrow}] \dagger} B_{r'l'}^{[\sigma'_{\uparrow}\sigma'_{\downarrow}]} \left( f(N, p) \langle l | \sigma_{\uparrow p}^{N+1} | l' \rangle \langle \sigma_{\uparrow}\sigma_{\downarrow} | \sigma_{\uparrow p}^N | \sigma'_{\uparrow}\sigma'_{\downarrow} \rangle \right. \\ \left. + f(N + 2, p) \langle l | \sigma_{\downarrow p}^{N+2} | l' \rangle \langle \sigma_{\uparrow}\sigma_{\downarrow} | \sigma_{\downarrow p}^{N+3} | \sigma'_{\uparrow}\sigma'_{\downarrow} \rangle \right). \quad (\text{C.19})$$

We may now make the identifications from Eqs. (C.12) and (C.13), noting that  $|r\rangle$  basis there is now regarded as  $|l\rangle$  for the current site  $k = 2$

$$\langle l | \sigma_{\uparrow p}^{N+1} | l' \rangle = \left( Sx_{\uparrow}\{1\}\{p\} \right)_w \quad \langle l | \sigma_{\downarrow p}^{N+2} | l' \rangle = \left( Sx_{\downarrow}\{1\}\{p\} \right)_w, \quad (\text{C.20})$$

which are already known from the previous iteration (see Eqs. (C.13) and (C.14)). After inserting this in Eq. (C.19) and taking care of those inner products that simplify to  $\delta_{\sigma\sigma'}$  or  $sx\{p\}$ , we arrive at

$$I_2 = \sum_{l, \sigma_{\uparrow}, \sigma_{\downarrow}} \sum_{l', \sigma'_{\uparrow}, \sigma'_{\downarrow}} \sum_{p=1}^3 B_{rl}^{[\sigma_{\uparrow}\sigma_{\downarrow}] \dagger} B_{r'l'}^{[\sigma'_{\uparrow}\sigma'_{\downarrow}]} f(N, p) (Sx_{\uparrow}\{1\}\{p\})_w (sx\{p\})_{\sigma_{\uparrow}\sigma'_{\uparrow}} \\ + \sum_{l, \sigma_{\uparrow}, \sigma_{\downarrow}} \sum_{l', \sigma'_{\uparrow}, \sigma'_{\downarrow}} \sum_{p=1}^3 B_{rl}^{[\sigma_{\uparrow}\sigma_{\downarrow}] \dagger} B_{r'l'}^{[\sigma'_{\uparrow}\sigma'_{\downarrow}]} f(N + 2, p) (Sx_{\downarrow}\{1\}\{p\})_w (sx\{p\})_{\sigma_{\downarrow}\sigma'_{\downarrow}}. \quad (\text{C.21})$$

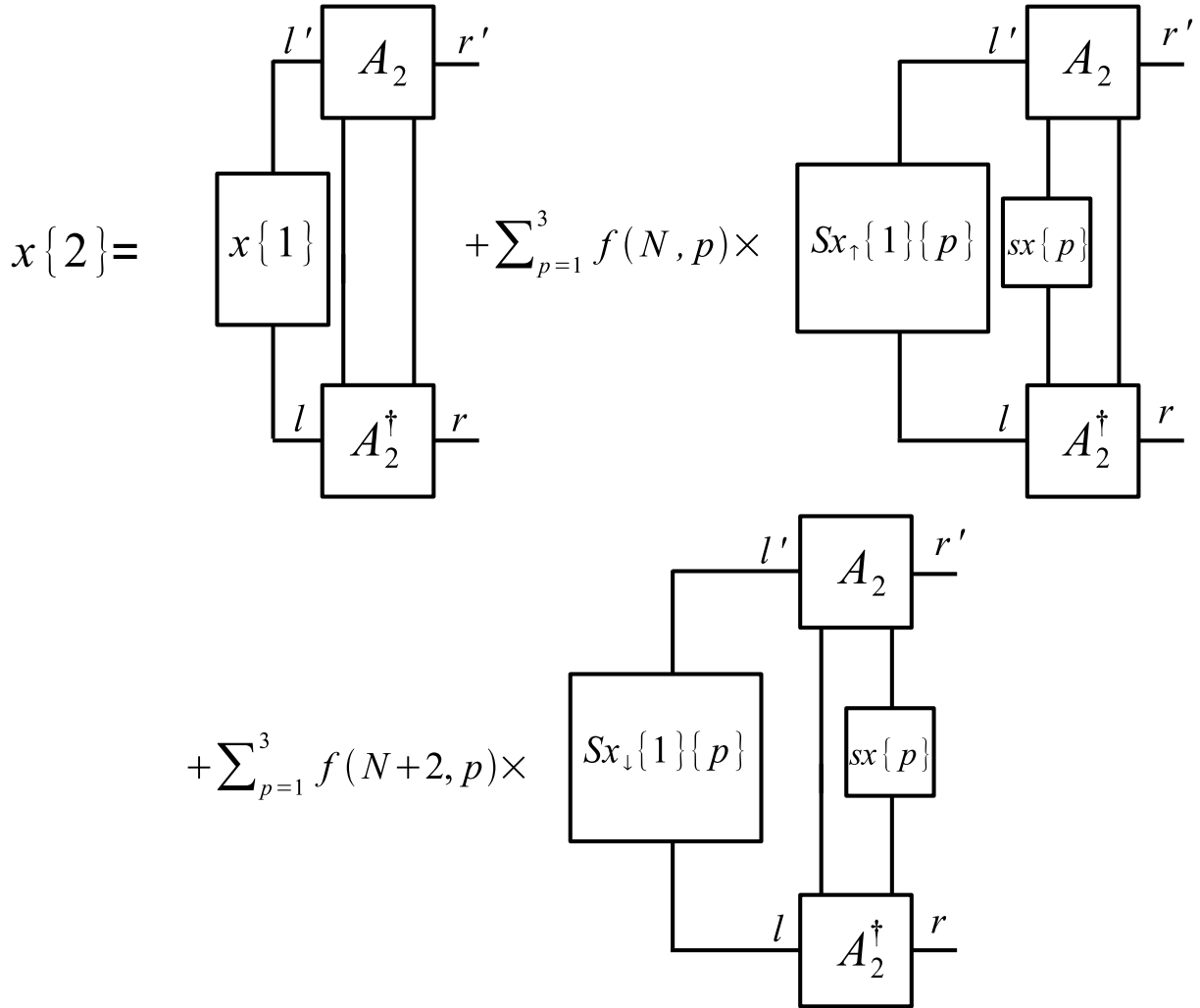


**Figure C.4:** Graphical MPS representation of calculating the effective refolded Hamiltonian for the site  $k = 2$ .

Since for SIAM the on-site interactions  $g$  vanish except for the impurity we simply get  $I_3 = \langle r | \mathcal{H}_2 | r' \rangle = 0$ . Putting altogether, we arrive at the graphical representation depicted in Fig. C.4 for  $x\{2\}$ .

It is easy to verify that the general recipe for obtaining the effective refolded Hamiltonian at site  $k > 1$  is given by Fig. C.5. This offers a recursive relation for obtaining the effective Hamiltonian at any site  $k > 1$  from the information of the previous site.

Having obtained the matrix elements of the effective “refolded Hamiltonian”, we may now diagonalize it to obtain the eigenvalues and eigenstates  $(E_\beta^n)_r$  and  $|E_\beta^n\rangle_r$  used for the calculation of eigenspectra and density of states in Section 4.5.2 as well as energy eigenstates in Section 4.5.3.

$$\begin{aligned}
 x\{k\} = & \left[ \begin{array}{c} l' \\ \text{---} \\ \boxed{A_k} \\ \text{---} \\ r' \\ \text{---} \\ \boxed{x\{k-1\}} \\ \text{---} \\ l \\ \text{---} \\ \boxed{A_k^\dagger} \\ \text{---} \\ r \end{array} \right] + \sum_{p=1}^3 f(N+2-k, p) \times \left[ \begin{array}{c} l' \\ \text{---} \\ \boxed{A_k} \\ \text{---} \\ r' \\ \text{---} \\ \boxed{Sx_\uparrow\{k-1\}\{p\}} \\ \text{---} \\ \boxed{sx\{p\}} \\ \text{---} \\ l \\ \text{---} \\ \boxed{A_k^\dagger} \\ \text{---} \\ r \end{array} \right] \\
 & + \sum_{p=1}^3 f(N+k, p) \times \left[ \begin{array}{c} l' \\ \text{---} \\ \boxed{A_k} \\ \text{---} \\ r' \\ \text{---} \\ \boxed{Sx_\downarrow\{k-1\}\{p\}} \\ \text{---} \\ \boxed{sx\{p\}} \\ \text{---} \\ l \\ \text{---} \\ \boxed{A_k^\dagger} \\ \text{---} \\ r \end{array} \right]
 \end{aligned}$$

where

$$\begin{aligned}
 Sx_\uparrow\{k-1\}\{p\} = & \left[ \begin{array}{c} l' \\ \text{---} \\ \boxed{A_{k-1}} \\ \text{---} \\ r' \\ \text{---} \\ \boxed{sx\{p\}} \\ \text{---} \\ \boxed{A_{k-1}^\dagger} \\ \text{---} \\ l \\ \text{---} \\ r \end{array} \right] \quad \text{and} \quad Sx_\downarrow\{k-1\}\{p\} = \left[ \begin{array}{c} l' \\ \text{---} \\ \boxed{A_{k-1}} \\ \text{---} \\ r' \\ \text{---} \\ \boxed{sx\{p\}} \\ \text{---} \\ \boxed{A_{k-1}^\dagger} \\ \text{---} \\ l \\ \text{---} \\ r \end{array} \right]
 \end{aligned}$$

**Figure C.5:** General recipe for obtaining the effective refolded Hamiltonian in a recursive manner when  $k > 1$ .



# Appendix D

## Variational “cloning” of folded to unfolded states

This appendix gives some details of the cloning procedure of Section 4.6.1. The goal is to solve the variational Eq. (4.33), which determines the  $B$ -matrices of the cloned state  $|G\rangle_c$ . As described in the main text, this can be done by sweeping back and forth along the unfolded Wilson chain, and updating one matrix at a time.

Let  $k\mu$  label the site to be updated and write the cloned state, which is assumed to be of the form (4.16), as

$$|G\rangle_c = \left( X_l^{k\mu} \right)_{1\nu} B_{\nu\nu'}^{[\sigma_{k\mu}]} \left( X_r^{k\mu} \right)_{\nu'1} . \quad (\text{D.1})$$

Here we introduced the shorthands

$$\left( X_l^{k\mu} \right)_{1\nu} = \left( B^{[\sigma_{N\downarrow}]} \dots B^{[\sigma_{k_l\mu_l}]} \right)_{1\nu} , \quad (\text{D.2a})$$

$$\left( X_r^{k\mu} \right)_{\nu'1} = \left( B^{[\sigma_{k_r\mu_r}] } \dots B^{[\sigma_{N\uparrow}]} \right)_{\nu'1} , \quad (\text{D.2b})$$

for the products of matrices standing before or after the one of present interest in the unfolded Wilson chain, and the labels  $k_l\mu_l$  or  $k_r\mu_r$  label the sites just before or after this site. Moreover, assume that all the  $B$ -matrices in  $X_l$  and  $X_r$  have been orthonormalized according to Eq. (A.1a) or (A.1b), respectively. (This can always be ensured by suitably orthonormalizing each  $B$ -matrix after updating it, see below.) These orthonormality relations immediately imply similar ones for the matrix products just introduced:

$$\sum_{\sigma_{N\downarrow}, \dots, \sigma_{k_l\mu_l}} \left( X_l^{k\mu} \right)_{\nu 1}^\dagger \left( X_l^{k\mu} \right)_{1\nu'} = \delta_{\nu\nu'} , \quad (\text{D.3a})$$

$$\sum_{\sigma_{k_r\mu_r}, \dots, \sigma_{N\uparrow}} \left( X_r^{k\mu} \right)_{\nu' 1} \left( X_r^{k\mu} \right)_{1\nu}^\dagger = \delta_{\nu\nu'} . \quad (\text{D.3b})$$

Thus, the norm of  $|G\rangle_c$  can be written as

$${}_c\langle G|G\rangle_c = \frac{1}{\mathcal{N}} \sum_{\nu\nu'} B_{\nu'\nu}^{[\sigma_{k\mu}]^\dagger} B_{\nu\nu'}^{[\sigma_{k\mu}]} , \quad (\text{D.4})$$

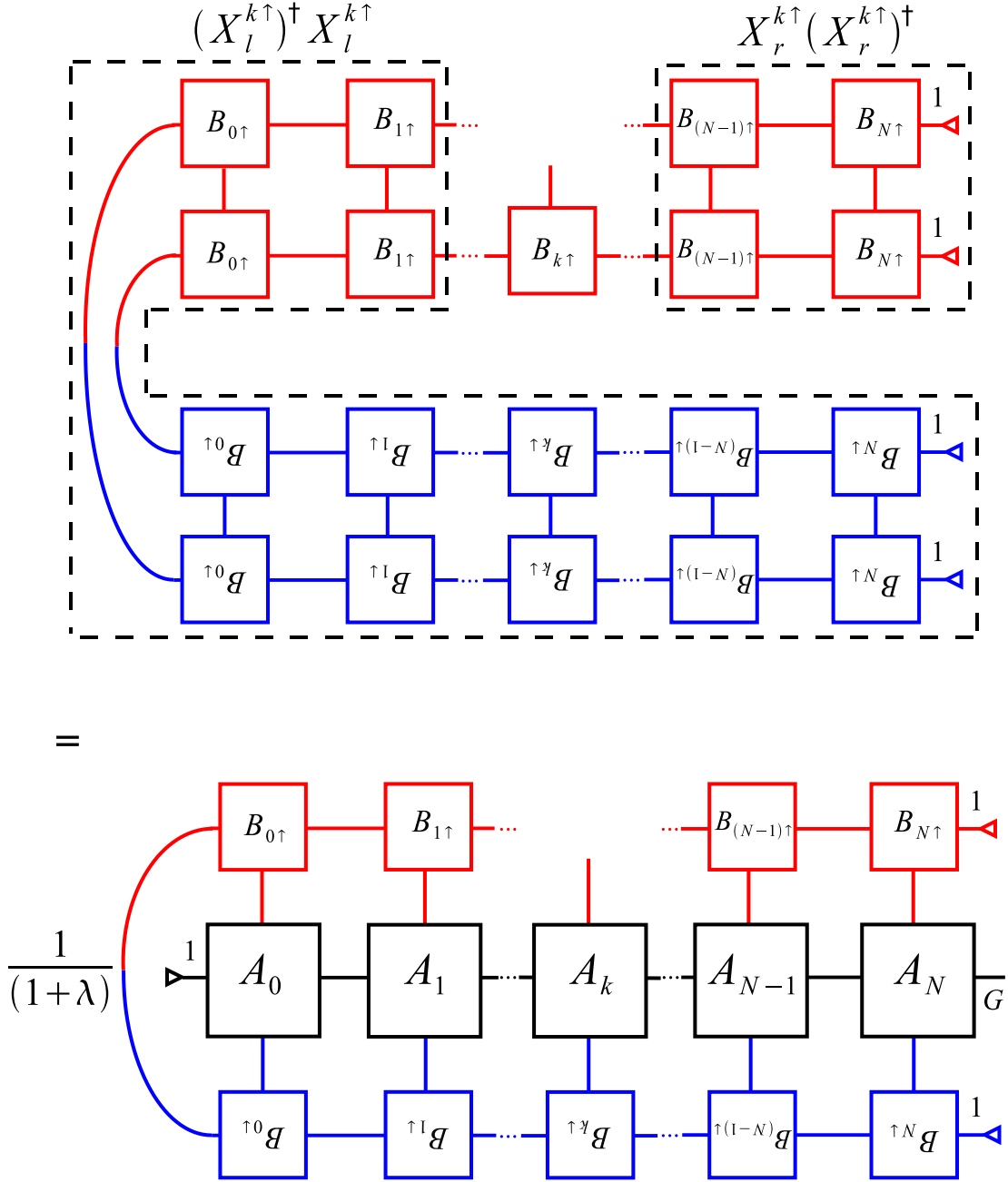


**Figure D.1:** Graphical representation of the variational equation used for cloning, Eqs. (4.33) or (D.5), drawn for the case  $\mu = \uparrow$ , and assuming all matrix elements to be real, using the labelling conventions of Figs. 4.2(a) and 4.2(c). The upper part of the figure represents  $\frac{1}{2} \frac{\partial}{\partial B^{[k\uparrow]}} c \langle G | G \rangle_c$ ; it simplifies to  $B^{[k\uparrow]}$  [left hand side of Eq. (D.5)] upon realizing that the parts in dashed boxes represent the left hand sides of Eqs. (D.3a) and (D.3b), and hence reduce to unity.



where  $\mathcal{N}$  is a normalization constant ensuring that the norm equals unity.

Using Eq. (D.4), the variational Eq. (4.33) readily reduces to

$$B_{\nu\nu'}^{[\sigma_{k\mu}]} = \sum_{\{\sigma'^N\}} \frac{(A^{[\sigma_N]^\dagger} \dots A^{[\sigma_0]^\dagger})_{G1}}{1 + \lambda} \left( X_l^{k\mu} \right)_{1\nu} \left( X_r^{k\mu} \right)_{\nu'1}, \quad (\text{D.5})$$

where  $\{\sigma'^N\}$  denotes the local indices of all sites except the index  $\sigma_{k\mu}$  of site  $k\mu$ , and we have assumed all  $A$ - and  $B$ -matrices to be purely real (exploiting the time-reversal invariance of the present model). This equation (graphically represented in Fig. D.1) completely determines the new matrix  $B^{[\sigma_{k\mu}]}$  in terms of the  $A$ -matrices specifying the NRG input state  $|G\rangle_f$  and the  $B$ -matrices of sites other than the present one, which had been kept fixed during this variational step.

Having calculated  $B^{[\sigma_{k\mu}]}$ , it should be properly orthonormalized, following the procedure of Eq. (A.3) or Eq. (A.4), depending on whether we are sweeping from left to right or vice versa. In other words, use the singular value decomposition  $\mathcal{U}\mathcal{S}\mathcal{V}^\dagger$  of the new-found matrix  $B^{[\sigma_{k\mu}]}$ , to transfer a factor  $\mathcal{S}\mathcal{V}^\dagger$  or  $\mathcal{U}\mathcal{S}$  onto its right or left neighbor, respectively, and rescale this neighbor by an overall constant to ensure that the new state  $|G\rangle_c$  is still normalized to unity. This concludes the update of site  $k\mu$ . Now move on to its neighbor, etc., and thus sweep back and forth through the unfolded Wilson chain, until convergence is reached.



# Appendix E

## Matrix norm and singular value decomposition

The *norm* of a matrix is not uniquely defined and there are several *non-equivalent* definitions of the norm of a matrix and each one suits a particular theory [91]. Let us now introduce two important norms that we shall use throughout this thesis and are indeed the most frequently used matrix norms in numerical analysis. The  $F$ -norm (Frobenius norm) of an  $m \times n$  matrix  $A$  is defined by

$$\|A\|_F = \left[ \sum_{i=1}^m \sum_{j=1}^n |a_{ij}|^2 \right]^{1/2}. \quad (\text{E.1})$$

Note that this is an entry-wise norm which treats an  $m \times n$  matrix as an  $1 \times m \cdot n$  matrix (or indeed a vector).

Another important definition of the norm of a matrix called  $p$ -norm is given by

$$\|A\|_p = \sup_{x \neq 0} \frac{\|Ax\|_p}{\|x\|_p}, \quad (\text{E.2})$$

where the corresponding vector  $p$ -norm (for  $p \geq 1$ ) is defined by

$$\|x\|_p = (|x_1|^p + \dots + |x_n|^p)^{1/p}. \quad (\text{E.3})$$

The theory of the norms can be exploited to prove one of the most important decompositions in matrix analysis [91] which can be stated as follows [92, 91]:

*Singular value decomposition (SVD)*: Let  $A$  be an  $m \times n$  arbitrary matrix ( $A_{m \times n}$ ) and let  $p = \min\{m, n\}$ . Then there exists a matrix  $\Sigma_{m \times n} = [\sigma_{ij}]$  with  $\sigma_{ij} = 0$  for all  $i \neq j$  and  $\sigma_{11} \geq \sigma_{22} \geq \dots \geq \sigma_{pp} \geq 0$ , and there are two unitary matrices  $U_{m \times m} = [u_1, \dots, u_m]$  and  $V_{n \times n} = [v_1, \dots, v_n]$  such that

$$A = U \Sigma V^\dagger, \quad (\text{E.4})$$

The  $\sigma_{ii}$  (or simply  $\sigma_i$ ) are called the *singular values* of  $A$  and have the following important properties [92]:

1. The singular values of  $A$  are exactly the nonnegative square roots of the  $p$  largest eigenvalues of either  $A^\dagger A$  or  $AA^\dagger$ .
2. The singular values of  $A$  and  $A^\dagger$  are the same.
3. Notice that the singular values of a matrix are unitarily invariant, i.e., the singular values of  $U_1 A U_2$  are the same as those of  $A$  for all unitary matrices of appropriate sizes  $U_1$  and  $U_2$ .

It is also worthwhile to mention that  $F$ -norm and 2-norm ( $p$ -norm for  $p = 2$ ) are *unitarily invariant*, namely

$$\|U A V\|_F = \|A\|_F, \quad (\text{E.5})$$

and

$$\|U A V\|_2 = \|A\|_2, \quad (\text{E.6})$$

where  $U$  and  $V$  are unitary matrices of appropriate sizes [91]. This property will be particularly useful for the lower-rank approximation of a matrix in the next section. Also, this invariance characteristic has a useful immediate consequence: A unitarily invariant norm of a matrix  $A$  is a function only of singular values of  $A$ , since

$$\|A\|_{F,2} = \|U \Sigma V^\dagger\|_{F,2} = \|\Sigma(A)\|_{F,2}, \quad (\text{E.7})$$

where use has been made of the singular value decomposition and unitarily invariance of the  $F$ -norm and 2-norm [92]. Moreover, it can be shown that the explicit functionality of the  $F$ -norm and 2-norm in terms of the singular values is given by [91]:

$$\|A\|_F^2 = \sum_{i=1}^p \sigma_i^2, \quad (\text{E.8})$$

and

$$\|A\|_2 = \sigma_1. \quad (\text{E.9})$$

## Part IV

### Miscellaneous



# Bibliography

- [1] W. von der Linden. *A quantum Monte Carlo approach to many-body physics*. Phys. Rep. **220**, 53–162 (1992).
- [2] K. G. Wilson. *The renormalization group: Critical phenomena and the Kondo problem*. Rev. Mod. Phys. **47**, 773–840 (1975).
- [3] H. R. Krishna-murthy, J. W. Wilkins and K. G. Wilson. *Renormalization-group approach to the Anderson model of dilute magnetic alloys. I. Static properties for the symmetric case*. Phys. Rev. B **21**, 1003–1043 (1980).
- [4] R. Bulla, T. A. Costi and T. Pruschke. *Numerical renormalization group method for quantum impurity systems*. Rev. Mod. Phys. **80**, 395 (2008).
- [5] S. R. White. *Density matrix formulation for quantum renormalization groups*. Phys. Rev. Lett. **69**, 2863–2866 (1992).
- [6] S. R. White. *Density-matrix algorithms for quantum renormalization groups*. Phys. Rev. B **48**, 10345–10356 (1993).
- [7] S. R. White. *Strongly correlated electron systems and the density matrix renormalization group*. Phys. Rep. **301**, 187–204 (1998).
- [8] U. Schollwöck. *The density-matrix renormalization group*. Rev. Mod. Phys. **77**, 259 (2005).
- [9] D. Gobert. *Applications of the density-matrix Renormalization group to mesoscopic Phenomena*. Ph.D. thesis, Ludwig-Maximilians-Universität München (2004).
- [10] W. Mündler. *Matrix Product Calculation of Correlation Density Matrices for 1-Dimensional Quantum Chains*. Master’s thesis, Ludwig-Maximilians-Universität München (2008).
- [11] K. Hallberg. *Density Matrix Renormalization: A Review of the Method and its Applications*. arXiv:0303557 (2003).

- [12] G. G. Batrouni and D. Poilblanc, editors. *Recent Developments in the DMRG applied to Quantum Chemistry*, volume 816 of *American Institute of Physics Conference Series* (2006).
- [13] Y. Nakamura, Y. A. Pashkin and J. S. Tsai. *Coherent control of macroscopic quantum states in a single-Cooper-pair box*. *Nature* **398**, 786–788 (1999).
- [14] I. Chiorescu, Y. Nakamura, C. J. P. M. Harmans and J. E. Mooij. *Coherent Quantum Dynamics of a Superconducting Flux Qubit*. *Science* **299**, 1869–1871 (2003).
- [15] D. V. Khveshchenko. *Quantum impurity models of noisy qubits*. *Phys. Rev. B* **69**, 153311 (2004).
- [16] S. Nishimoto and E. Jeckelmann. *Density-matrix renormalization group approach to quantum impurity problems*. *Journal of Physics: Condensed Matter* **16**, 613–625 (2004).
- [17] S. R. White and A. E. Feiguin. *Real-Time Evolution Using the Density Matrix Renormalization Group*. *Phys. Rev. Lett.* **93**, 076401 (2004).
- [18] U. Schollwöck and S. R. White. *Methods for Time Dependence in DMRG*. arXiv:cond-mat/0606018v1 (2006).
- [19] C. Guo, A. Weichselbaum, S. Kehrein, T. Xiang and J. von Delft. *Using DMRG to Study Quantum Impurity Models with Time-Dependent Hamiltonians*. arXiv:0810.2900 (2008).
- [20] S. Östlund and S. Rommer. *Thermodynamic Limit of Density Matrix Renormalization*. *Phys. Rev. Lett.* **75**, 3537–3540 (1995).
- [21] S. Rommer and S. Östlund. *Class of ansatz wave functions for one-dimensional spin systems and their relation to the density matrix renormalization group*. *Phys. Rev. B* **55**, 2164–2181 (1997).
- [22] J. Dukelsky, M. A. Martin-Delgado, T. Nishino and G. Sierra. *Density matrix formulation for quantum renormalization groups*. *Europhys. Lett.* **43**, 457–462 (1998).
- [23] D. Perez-Garcia, F. Verstraete, M. M. Wolf and J. I. Cirac. *Matrix Product State Representations*. *Quantum Inf. Comput.* **7**, 401 (2007).
- [24] P. W. Anderson. *Localized Magnetic States in Metals*. *Phys. Rev.* **124**, 41–53 (1961).
- [25] M. E. Perotti. *Matrix Product Formalism*. Master’s thesis, Technische Universität München and Max-Planck-Institut für Quantenoptik (2005).
- [26] C. Schön. *Quantum Information Processing and Cavity QED*. Ph.D. thesis, Technische Universität München and Max-Planck-Institut für Quantenoptik (2005).



- [27] L. Lamata. *Developments in entanglement theory and applications to relevant physical systems*. Ph.D. thesis, Universidad Autónoma de Madrid (2007).
- [28] D. M. Greenberger, M. Horne and A. Zeilinger. *Bell's Theorem, Quantum Theory, and Conceptions of the Universe*. Kluwer, Dordrecht (1989).
- [29] W. Dür, G. Vidal and J. I. Cirac. *Three qubits can be entangled in two inequivalent ways*. Phys. Rev. A **62**, 062314 (2000).
- [30] R. Raussendorf and H. J. Briegel. *A One-Way Quantum Computer*. Phys. Rev. Lett. **86**, 5188–5191 (2001).
- [31] C. Schön, E. Solano, F. Verstraete, J. I. Cirac and M. M. Wolf. *Sequential Generation of Entangled Multiqubit States*. Phys. Rev. Lett. **95**, 110503 (2005).
- [32] C. Schön, K. Hammerer, M. M. Wolf, J. I. Cirac and E. Solano. *Sequential generation of matrix-product states in cavity QED*. Phys. Rev. A **75**, 032311 (2007).
- [33] H. Saberi, A. Weichselbaum, L. Lamata, D. Pérez-García, J. von Delft and E. Solano. *Constrained Optimization of Sequentially Generated Entangled Multiqubit States*. arXiv:0810.0977 (2008).
- [34] D. P. Bertsekas. *Constrained Optimization and Lagrange Multiplier Methods*. Athena Scientific, Belmont (1996).
- [35] G. M. Crosswhite, A. C. Doherty and G. Vidal. *Applying matrix product operators to model systems with long-range interactions*. Phys. Rev. B **78**, 035116 (2008).
- [36] I. P. McCulloch. *From density-matrix renormalization group to matrix product states*. Journal of Statistical Mechanics: Theory and Experiment **2007**, P10014 (2007).
- [37] I. P. McCulloch. *Infinite size density matrix renormalization group, revisited*. arXiv:0804.2509 (2008).
- [38] V. Murg, J. I. Cirac, B. Pirvu and F. Verstraete. *Matrix product operator representations*. arXiv:0804.3976 (2008).
- [39] L. Lamata, J. Leon, D. Perez-Garcia, D. Salgado and E. Solano. *Sequential Implementation of Global Quantum Operations*. Phys. Rev. Lett. **101**, 180506 (2008).
- [40] J. Kondo. *Resistance Minimum in Dilute Magnetic Alloys*. Prog. Theor. Phys. **32**, 37–49 (1964).
- [41] A. Altland and B. Simons. *Condensed matter field theory*. Cambridge Univ. Press, Cambridge (2006).

- [42] J. Hubbard. *Electron Correlations in Narrow Energy Bands*. Proceedings of the Royal Society of London. Series A, Mathematical and Physical Sciences (1934-1990) **276**, 238–257 (1963).
- [43] J. W. Bray and S. T. Chui. *Computer renormalization-group calculations of  $2kF$  and  $4kF$  correlation functions of the one-dimensional Hubbard model*. Phys. Rev. B **19**, 4876–4882 (1979).
- [44] T. Xiang and G. Gehring. *Real space renormalisation group study of Heisenberg spin chain*. Journal of Magnetism and Magnetic Materials **104-107**, 861–862 (1992).
- [45] S. R. White and R. M. Noack. *Real-space quantum renormalization groups*. Phys. Rev. Lett. **68**, 3487–3490 (1992).
- [46] V. Hakim and J. P. Nadal. *Exact results for 2D directed animals on a strip of finite width*. Journal of Physics A: Mathematical and General **16**, L213–L218 (1983).
- [47] V. Karimipour. *Some general features of matrix product states in stochastic systems*. Journal of Physics A: Mathematical and General **33**, 709–719 (2000).
- [48] A. Klumper, A. Schadschneider and J. Zittartz. *Equivalence and solution of anisotropic spin-1 models and generalized  $t$ - $J$  fermion models in one dimension*. Journal of Physics A: Mathematical and General **24**, L955–L959 (1991).
- [49] H. Hinrichsen, S. Sandow and I. Peschel. *On matrix product ground states for reaction - diffusion models*. Journal of Physics A: Mathematical and General **29**, 2643–2649 (1996).
- [50] A. Honecker and I. Peschel. *Matrix-product states for a one-dimensional lattice gas with parallel dynamics*. J. Stat. Phys. **88**, 319–345 (1997).
- [51] A. Weichselbaum, F. Verstraete, U. Schollwöck, J. I. Cirac and J. von Delft. *Variational matrix product state approach to quantum impurity models*. cond-mat/0504305v2 (2005).
- [52] F. Verstraete, D. Porras and J. I. Cirac. *Density Matrix Renormalization Group and Periodic Boundary Conditions: A Quantum Information Perspective*. Phys. Rev. Lett. **93**, 227205 (2004).
- [53] G. Vidal. *Efficient Classical Simulation of Slightly Entangled Quantum Computations*. Phys. Rev. Lett. **91**, 147902 (2003).
- [54] G. Vidal, J. I. Latorre, E. Rico and A. Kitaev. *Entanglement in Quantum Critical Phenomena*. Phys. Rev. Lett. **90**, 227902 (2003).
- [55] F. Verstraete and J. I. Cirac. *Valence-bond states for quantum computation*. Phys. Rev. A **70**, 060302 (2004).

- [56] A. Ekert and P. L. Knight. *Entangled quantum systems and the Schmidt decomposition*. American Journal of Physics **63**, 415–423 (1995).
- [57] M. A. Nielsen and I. L. Chuang. *Quantum Computation and Quantum Information*. Cambridge University Press, Cambridge (2000).
- [58] D. M. G. A. Zeilinger, M. A. Horne. *Higher-order quantum entanglement*. NASA Conf. Publ. **3135**, 73–81 (1992).
- [59] C. F. Roos, M. Riebe, H. Haffner, W. Hansel, J. Benhelm, G. P. T. Lancaster, C. Becher, F. Schmidt-Kaler and R. Blatt. *Control and Measurement of Three-Qubit Entangled States*. Science **304**, 1478–1480 (2004).
- [60] H. J. Briegel and R. Raussendorf. *Persistent Entanglement in Arrays of Interacting Particles*. Phys. Rev. Lett. **86**, 910–913 (2001).
- [61] H. Haffner, W. Hansel, C. F. Roos, J. Benhelm, D. C. al kar, M. Chwalla, T. Korber, U. D. Rapol, M. Riebe, P. O. Schmidt, C. Becher, O. Guhne, W. Dur and R. Blatt. *Scalable multiparticle entanglement of trapped ions*. Nature **438**, 643–646 (2005).
- [62] J. Joo, J. Lee, J. Jang and Y.-J. Park. *Quantum Secure Communication with W States*. quant-ph/0204003 (2002).
- [63] H. Buhrman, W. van Dam, P. Høyer and A. Tapp. *Multiparty quantum communication complexity*. Phys. Rev. A **60**, 2737–2741 (1999).
- [64] D. Leibfried, E. Knill, S. Seidelin, J. Britton, R. B. Blakestad, J. Chiaverini, D. B. Hume, W. M. Itano, J. D. Jost, C. Langer, R. Ozeri, R. Reichle and D. J. Wineland. *Creation of a six-atom Schrödinger cat state*. Nature **438**, 639–642 (2005).
- [65] A. Kuhn, M. Hennrich and G. Rempe. *Deterministic Single-Photon Source for Distributed Quantum Networking*. Phys. Rev. Lett. **89**, 067901 (2002).
- [66] J. McKeever, A. Boca, A. D. Boozer, R. Miller, J. R. Buck, A. Kuzmich and H. J. Kimble. *Deterministic Generation of Single Photons from One Atom Trapped in a Cavity*. Science **303**, 1992–1994 (2004).
- [67] M. Keller, B. Lange, K. Hayasaka, W. Lange and H. Walther. *Continuous generation of single photons with controlled waveform in an ion-trap cavity system*. Nature **431**, 1075–1078 (2004).
- [68] M. C. Banuls, D. Perez-Garcia, M. M. Wolf, F. Verstraete and J. I. Cirac. *Sequentially generated states for the study of two-dimensional systems*. Phys. Rev. A **77**, 052306–9 (2008).
- [69] F. B. Anders and A. Schiller. *Real-Time Dynamics in Quantum-Impurity Systems: A Time-Dependent Numerical Renormalization-Group Approach*. Phys. Rev. Lett. **95**, 196801 (2005).

- [70] F. B. Anders and A. Schiller. *Spin precession and real-time dynamics in the Kondo model: Time-dependent numerical renormalization-group study*. Phys. Rev. B **74**, 245113 (2006).
- [71] R. Peters, T. Pruschke and F. B. Anders. *Numerical renormalization group approach to Green's functions for quantum impurity models*. Phys. Rev. B **74**, 245114 (2006).
- [72] A. Weichselbaum and J. von Delft. *Sum-Rule Conserving Spectral Functions from the Numerical Renormalization Group*. Phys. Rev. Lett. **99**, 076402 (2007).
- [73] M. Sindel. *Numerical Renormalization Group studies of Quantum Impurity Models in the Strong Coupling Limit*. Ph.D. thesis, Ludwig-Maximilians-Universität München (2004).
- [74] T. Hecht. *Numerical Renormalization Group studies of Correlation effects in Phase Coherent Transport through Quantum Dots*. Ph.D. thesis, Ludwig-Maximilians-Universität München (2008).
- [75] M. Fannes, B. Nachtergaele and R. Werner. *Finitely correlated states on quantum spin chains*. Commun. Math. Phys. **144**, 443–490 (1992).
- [76] H. Takasaki, T. Hikihara and T. Nishino. *Fixed Point of the Finite System DMRG*. Journal of the Physical Society of Japan **68**, 1537–1540 (1999).
- [77] C. Raas, G. S. Uhrig and F. B. Anders. *High-energy dynamics of the single-impurity Anderson model*. Phys. Rev. B **69**, 041102 (2004).
- [78] P. Jordan and E. Wigner. *Über das Paulische Äquivalenzverbot*. Zeitschrift für Physik A Hadrons and Nuclei **47**, 631–651 (1928).
- [79] A. Holzner. *Matrix product state approach for a multi-lead Anderson model*. Master's thesis, Ludwig-Maximilians-Universität München (2006).
- [80] A. Holzner, A. Weichselbaum and J. von Delft. *Matrix product state approach for a two-lead, multi-level Anderson impurity model*. arXiv:0804.0550 (2008).
- [81] M. Pustilnik and L. Glazman. *Kondo effect in quantum dots*. Journal of Physics: Condensed Matter **16**, R513–R537 (2004).
- [82] A. I. Toth, C. P. Moca, O. Legeza and G. Zarand. *Density matrix numerical renormalization group for non-Abelian symmetries*. cond-mat/0802.4332 (2008).
- [83] H. Saberi, A. Weichselbaum and J. von Delft. *Matrix-product-state comparison of the numerical renormalization group and the variational formulation of the density-matrix renormalization group*. Phys. Rev. B **78**, 035124 (2008).

- [84] J.-W. Pan, D. Bouwmeester, M. Daniell, H. Weinfurter and A. Zeilinger. *Experimental test of quantum nonlocality in three-photon Greenberger-Horne-Zeilinger entanglement*. Nature **403**, 515–519 (2000).
- [85] A. Rauschenbeutel, G. Nogues, S. Osnaghi, P. Bertet, M. Brune, J.-M. Raimond and S. Haroche. *Step-by-Step Engineered Multiparticle Entanglement*. Science **288**, 2024–2028 (2000).
- [86] N. Kiesel, C. Schmid, G. Toth, E. Solano and H. Weinfurter. *Experimental Observation of Four-Photon Entangled Dicke State with High Fidelity*. Physical Review Letters **98**, 063604 (2007).
- [87] N. Kiesel, C. Schmid, U. Weber, G. Toth, O. Guhne, R. Ursin and H. Weinfurter. *Experimental Analysis of a Four-Qubit Photon Cluster State*. Phys. Rev. Lett. **95**, 210502 (2005).
- [88] F. Byron and R. Fuller. *Mathematics of Classical and Quantum Physics*. Addison-Wesley (1969).
- [89] H. Andrews and C. Patterson. *Singular Value Decomposition (SVD) Image Coding*. Communications, IEEE Transactions on [legacy, pre - 1988] **24**, 425–432 (1976).
- [90] J. I. Latorre. *Image compression and entanglement*. arXiv:quant-ph/0510031 (2005).
- [91] G. H. Golub and C. F. V. Loan. *Matrix Computations*. The John Hopkins University Press, Baltimore (1996).
- [92] R. A. Horn and C. R. Johnson. *Topics in Matrix Analysis*. Cambridge University Press, Cambridge (1991).
- [93] K. R. Brown, J. Vala and K. B. Whaley. *Scalable ion trap quantum computation in decoherence-free subspaces with pairwise interactions only*. Phys. Rev. A **67**, 012309 (2003).
- [94] Y. Makhlin. *Nonlocal Properties of Two-Qubit Gates and Mixed States, and the Optimization of Quantum Computations*. Quantum Information Processing **1**, 243–252 (2002).
- [95] J. Zhang, J. Vala, S. Sastry and K. B. Whaley. *Minimum Construction of Two-Qubit Quantum Operations*. Phys. Rev. Lett. **93**, 020502 (2004).
- [96] J. Zhang and K. B. Whaley. *Generation of quantum logic operations from physical Hamiltonians*. Phys. Rev. A **71**, 052317 (2005).
- [97] D. P. DiVincenzo. *Two-bit gates are universal for quantum computation*. Phys. Rev. A **51**, 1015–1022 (1995).

- 
- [98] A. Barenco, C. H. Bennett, R. Cleve, D. P. DiVincenzo, N. Margolus, P. Shor, T. Sleator, J. A. Smolin and H. Weinfurter. *Elementary gates for quantum computation*. Phys. Rev. A **52**, 3457–3467 (1995).
- [99] D. Deutsch. *Quantum Theory, the Church-Turing Principle and the Universal Quantum Computer*. Proc. R. Soc. A **400**, 97 (1985).
- [100] F. Verstraete, J. J. García-Ripoll and J. I. Cirac. *Matrix Product Density Operators: Simulation of Finite-Temperature and Dissipative Systems*. Phys. Rev. Lett. **93**, 207204 (2004).
- [101] Y. Delgado, L. Lamata, J. Leon, D. Salgado and E. Solano. *Sequential Quantum Cloning*. Phys. Rev. Lett. **98**, 150502 (2007).
- [102] N. Gisin and S. Massar. *Optimal Quantum Cloning Machines*. Phys. Rev. Lett. **79**, 2153–2156 (1997).
- [103] V. Bužek and M. Hillery. *Quantum copying: Beyond the no-cloning theorem*. Phys. Rev. A **54**, 1844–1852 (1996).
- [104] N. J. Higham. *Estimating the matrix  $p$ -norm*. Numer. Math **62**, 511–538 (1992).

---

## Deutsche Zusammenfassung

In dieser Doktorarbeit werden am Beispiel dreier größerer Projekte neue Entwicklungen im Bereich der Theorie von Matrixproduktzuständen (MPZ), die zur Untersuchung stark korrelierter Systeme sowie im Gebiet der Quanteninformationsverarbeitung Anwendung finden, vorgestellt:

In einem ersten Projekt vergleichen wir systematisch Wilson's Numerische Renormierungsgruppe (NRG) mit White's Dichtematrixrenormierung (DMRG). Ein auf NRG basierender Zugang zu Quantenstörstellmodellen führt zu Energieeigenzuständen, die die Form von Matrixproduktzuständen annehmen. Die Anwendung von White's DMRG auf Quantengitterprobleme kann gleichermaßen in der Sprache der MPZ formuliert werden. Diese bildet somit eine gemeinsame algebraische Struktur für beide Herangehensweisen. Wir nutzen dies um einen auf NRG beruhenden Zugang zum Anderson-Modell einer einzelnen Störstelle mit einem variationellen Matrixproduktzustand (VMPZ) zu vergleichen, der der DMRG für einen Gitterplatz entspricht. Für zweiteren nutzen wir eine entfaltete Wilson-Kette, die, verglichen mit NRG, eine erhebliche Reduzierung des numerischen Aufwandes erlaubt. Wir zeigen, dass alle NRG-Eigenzustände durch VMPZ reproduziert werden können und vergleichen zwei Trunkierungskriterien, scharf bzw. glatt im Energieraum. Wir zeigen, dass NRG-Ergebnisse systematisch durch eine variationelle Optimierung im Raum der VMPZ verbessert werden können, wobei die von NRG erzeugten Zustände als Anfangswert dienen.

In einem zweiten Projekt zeigen wir, wie MPZ eine flexible Struktur bilden, um Optimierungsprobleme unter Nebenbedingungen zu lösen. Diese Nebenbedingungen treten auf bei der schrittweisen Bildung verschränkter Zustände aus mehreren Qbits unter experimentellen Bedingungen. Wir betrachten ein realistisches Szenario, in dem ein Hilfssystem (ancilla) mit einer begrenzten Anzahl an Energieniveaus schrittweise begrenzte Wechselwirkungen mit Qbits in einer Reihe ausführt. Die vorgeschlagene Methode beruht auf einem geeigneten lokalen Optimierungsverfahren, das eine effiziente Vorschrift für eine realistische und näherungsweise Erzeugung eines beliebigen verschränkten Zustands vieler Qbits beinhaltet. Wir führen paradigmatische Beispiele an, die von Interesse für experimentelle oder theoretische Entwicklungen sein können.

Das dritte Projekt behandelt die sequentielle Erzeugung von Operationen. Es ist bekannt, dass die Erzeugung einer beliebigen globalen unitären Operation mit prinzipiellen Schwierigkeiten verbunden ist. Vor diesem Hintergrund wäre es wünschenswert, ein Protokoll zu entwickeln, das die gewünschte unitäre Operation im Rahmen einer sequenziellen Prozedur darstellt, bei der ein Hilfssystem lokal und jeweils nur einmal mit jedem Qbit einer Reihe wechselwirkt. Der Hauptaspekt hierbei ist die Frage, ob es möglich ist, eine solche sequenziell generierte Operation zu entwickeln. Wir geben Optimierungsprotokolle an, die eine optimale Realisierung einer sequenziellen Version der erwünschten globalen

unitären Operation mit optimaler Fidelity erlaubt.



# Acknowledgements

Finally, I would like to thank all the people who helped me to reach *this page* of the thesis!

I would like to take the opportunity, first of all, to express my best gratitude to my boss and PhD advisor Prof. Jan von Delft for accepting me as a PhD student in his group and suggesting various projects on which this thesis is based on. I thank him for his patience and constant support during my PhD years and am very grateful to him for his helpful and critical comments in writing up scientific articles. His critical comments and insightful feedbacks were essential for the success of all projects. I also thank him for sending me to many conferences, the possibility to visit my collaborators, and especially for giving me the opportunity to collaborate with Prof. Enrique Solano and his company. It was a great pleasure for me to be part of his group and to be working in such an excellent scientific environment.

My best gratitude also goes to my PhD advisor Prof. Enrique Solano for his constant support and encouragements throughout our joint projects and many fruitful discussions. It was all luck and a great privilege to work under his supervision. I am grateful to him for his close and highly disciplined supervision of our joint projects. I also appreciate very nice conversations about science as well as other aspects of life. I am also thankful to him for inviting me for a research visit at Universidad del País Vasco Bilbao.

Many thanks to Dr. Lucas Lamata, my collaborator at Max-Planck-Institute für Quantenoptik Garching, which was always willing to discuss and very supportive in our two joint projects. He always showed interest in my results and their interpretations. I am grateful to him for his valuable feedbacks with his deep knowledge of quantum information theory, and many insightful discussions throughout our collaborations.

Many thanks also to Prof. David Pérez-García at Universidad Complutense de Madrid for stimulating discussions and particularly elegant ideas on mathematical aspects of the problems throughout our collaborations.

I thank Dr. Andreas Weichselbaum for many fruitful discussions in numerical techniques. His advises on numerics were essential for the success of our projects.

I would like to thank Prof. Matthias Christandl for co-refereeing this thesis. I also thank Prof. Gerhard Rempe, Prof. Gerhard Buchalla and Prof. Harald Weinfurter for accepting to be part of my PhD examination committee.

I thank Universidad del País Vasco for hospitality and am grateful to Prof. Enrique Solano, Prof. Eugene Sherman and Guillermo Romero for their help and kind hospitality during my stay in Bilbao.

Thanks go to the Center for Nanoscience (CeNS) for their organizational help and support during the CeNS activities, the poster printing efforts, financial travel support, and scientific events organized by CeNS. And the Arnold Sommerfeld Center for Theoretical Physics (ASC) for providing a great working environment with excellent lecturers and workshops.

I gratefully acknowledge financial support of the DFG through the Sonderforschungsbereich “Solid-State Quantum Information Processing: Physical Concepts and Material Aspects” (SFB 631, De-730/3-2), and the German Excellence Initiative via the “Nanosystems Initiative Munich” (NIM).

Many thanks to Theresa Hecht, Michael Möckel and Ali Naji for helping me with many things to get started (and graduate!) as a PhD student in Munich. I particularly thank Michael and Theresa for talking to me in German at work and helping me this way to improve my German (*Danke für alles!*). Thanks also to Michael for helping me with preparing the Deutsche Zusammenfassung, and to Theresa for helping me with some technicalities in thesis layout.

Thanks also to all former and current group members at chair for theoretical condensed matter physics of Prof. von Delft for providing a great scientific atmosphere in the group:

Prof. Stefan Kehrein (particularly for his excellent course on renormalization methods in condensed matter theory), Florian Marquardt (for his excellent lectures on mesoscopic physics), Mikhail Kiselev (his excellent many-body course), Michael Sindel (fruitful discussions about NRG), Vitaly Golovach (various interesting physics discussions), Andreas Holzner (fruitful discussions on matrix-product states and DMRG), Cheng Guo (for nice science and life conversations), Henrik Gutmann, Udo Hartmann, Markus Storckz, Ioana Serban, Benjamin Abel, Peter Fritsch, Wolfgang Münden, Barbara Englert, Markus Heyl, Max Ludwig, Alexandre Faribault, Jiang Qian, Björn Kubala, Maximilians Treiber, Stéphane Schoonover and Silvia Kaiser.

I particularly thank my officemates Michael Möckel and Georg Heinrich for their great accompany and many nice discussions throughout.

I also appreciate interesting discussions with our excellent visitors here in Munich: Prof. Frank Verstraete, Prof. Piet Brouwer (particularly for the great discussions in Venice CeNS workshop), Brendan Huang, Jörn Kupferschmidt, Dr. Hakan Tureci and Dr. Akbar Jafari.

I would also like to take the opportunity to thank my former professors back in Tehran both at Sharif university of technology and Shahid Beheshti university: I thank my M.Sc. advisor Dr. Farshad Ebrahimi for attracting me to the exciting field of condensed matter theory and mesoscopic physics. Dr. Seifoallh Jalili for his great courses in computational physics and motivating me in numerics. Dr. Hasan Azizi and Dr. Mohammad-Mehdi Tehranchi for the original motivations on solid-state physics. Thanks also to Dr. Neda Sadoughi (for original motivations on quantum mechanics), Dr. Ahmad Amjadi (my B.Sc. advisor), Dr. Mohammad Reza Hedayati and Dr. Siamak Gousheh. Thanks also to my high-school physics teacher, Mehrdad Anousheh, the main reason that I decided to study physics!

I particularly thank Prof. Vahid Karimipour for inviting me to visit his group and present part of my PhD research in his quantum information group at Sharif university of technology in Tehran and gratefully acknowledge fruitful discussions with Sahar Alipour and Dr. Abolfazl Bayat on matrix-product states.

My best gratitude to Dr. Afif Siddiki for all his scientific and moral support during my PhD years in Munich, also to his wife Ayse for her kind hospitality. I wish them all the best in their new career at Mugla university as professor.

Thanks also to friends (also colleagues at LMU and TU!) during the PhD years for the great time in Munich: Saeid Ansari, Hasan Sadat Nabi, Abdullah Yoldas, Saeid Aminian, Iman Chashmahcharagh, Maryam Kazerani Farahani, Katy Tabatabaei, Nima Noushi, Tahmineh Pourrostami and Zahra Asgharpour.

Thanks also to Ali Abedi, Elham Khosravi, Payam Norouzzadeh, Mehrnaz Bozorgnia, Lida Ghasemzadeh, André Schleife and Ralph Hambach for the great time in Jülich spring school. Also to Massoud Borhani, Shabnam Safaei, Saeed Abedinour, Mehdi Pourfath and Fardin Kheirandish for the great time in Windsor summer school.

I thank Robert Helling for organizing lively ASC soccer matches. In particular, I thank all my soccer team-mates, Prof. Dieter Lüst, Korbinian Paul, Vitaly Vanchurin, Andrei Constantin and Frederik Beaujean for our great performance and fantastic games in Elite cup tournament.

Last but not least, my deepest gratitude to my parents, to whom this thesis is dedicated. For their constant support, efforts and believe in me.

My deepest gratitude also to my sister Nasim (I should also then mention Mehdi) and

my brother Ali for their steady encouragements and keeping me motivated to pursue my scientific careers both at home and abroad, so did my parents.

I particularly thank the greatest teachers of my life, my father and my mother, for their valueable *life lessons*.

# Curriculum vitae

Hamed Saberi, M.Sc.

born May 1, 1981 in Arak, Iran

## Education

- 10/2004–11/2008 Ph.D. studies in Theoretical Condensed Matter Physics supervised by Prof. Dr. Jan von Delft and Prof. Dr. Enrique Solano Physics Department, Center for NanoScience and Arnold Sommerfeld Center for Theoretical Physics, Ludwig-Maximilians Universität, München
- 10/2002–08/2004 M.Sc. studies in Theoretical Condensed Matter Physics Master's thesis supervised by Dr. Farshad Ebrahimi Shahid Beheshti University, Tehran  
“Quantum monte carlo simulation of persistent currents in Aharonov-Bohm rings”
- 10/1998–08/2002 B.Sc. studies in Atomic and Molecular Physics Bachelor's thesis supervised by Dr. Ahmad Amjadi Sharif University of Technology, Tehran  
“Molecular-dynamics simulation of nano-scale shock-wave propagation by photo-dissociation of impurities in solid Argon”
- 07/1998 Pre-university Diploma in Mathematics Shahid Motahhari pre-university center, Tehran
- 07/1997 High school Diploma in Mathematics Yekan high school, Tehran